LICENTIATE THESIS

Fluids, Particles, and Their Interactions

Linus Sundberg

DEPARTMENT OF PHYSICS

UNIVERSITY OF GOTHENBURG

THESIS FOR THE DEGREE OF LICENTIATE OF PHILOSOPHY

Fluids, particles, and their interactions

LINUS SUNDBERG

Department of Physics
University of Gothenburg
Göteborg, Sweden 2026

UNIVERSITY OF GOTHENBURG

Fluids, particles, and their interactions
Linus Sundberg

Department of Physics
University of Gothenburg
SE-412 96 Göteborg
Sweden
Telephone: +46 (0)31-786 00 00

Printed by Stema Specialtryck AB
Borås, Sweden 2026

ABSTRACT

Particles suspended in a fluid form an interacting system, where the fluid exerts hydrodynamic forces and torques on the particles, and the particles generate disturbances in the fluid flow. For large particles, there are two types of inertia involved in the dynamics of the particle suspension: (i) particle inertia and (ii) fluid inertia.

Particle inertia, measured by the dimensionless Stokes number, allows particles to detach from the flow. This implies that nearby particles can have very large velocity differences. The underlying multivalued particle-velocity field is formed when the phase-space manifold folds over (caustic). Here, we investigate how the tails of the fluid-velocity gradient distribution affect caustic formation.

Fluid inertia, measured by the non-dimensional particle Reynolds number, affects the hydrodynamic forces and torques on the suspended particles. The fluid inertia corrections to the hydrodynamic force and torque are given as polynomials in the relative velocity and angular velocity of particle and fluid. In this thesis, we derive constraints upon the coefficients of the polynomials based on particle-shape symmetries. These constraints are used to predict the fluid-inertial correction to the torque on a curved fibre settling in a quiescent fluid and determine the orientation of which the wire settles. The predicted tilt angle is found to be in qualitative agreement with experimental measurements on settling fibres in quiescent air.

Keywords: particle inertia, caustic formation, atmospheric fibres, particle shape symmetries, inertial torques

LIST OF PAPERS

This thesis consists of an introductory text to the following papers that are appended to the thesis:

Paper [I]

J. MEIBOHM, **L. SUNDBERG**, B. MEHLIG, K. GUSTAVSSON. Caustic formation in a non-Gaussian model for turbulent aerosols. *Physical Review Fluids* **9**, 024302.

Contribution: Performed all numerical simulations for the rate and path of caustic formation in 1D, and analysed the results. Contributed in writing the final manuscript.

Paper [II]

F. CANDELIER, K. GUSTAVSSON, P. SHARMA, **L. SUNDBERG**, A. PUMIR, G. BAGHERI, B. MEHLIG. Torques on curved atmospheric fibers. *Physical Review Fluids* **7**, 013179.

Contribution: Used particle-shape symmetry to constrain the force and torque. Contributed to the analysis of the bifurcation and the slender-body theory.

Paper [III]

L. SUNDBERG, F. CANDELIER, N. FINTZI, G. VOTH, J.L. PIERSON, K. GUSTAVSSON, B. MEHLIG. Fluid-inertia torques from particle-shape symmetry. *Preprint.*

Contribution: Constrained all torques from point-group symmetries, compared the predicted results with previous results for the fore-aft symmetry breaking. Contributed to writing of the manuscript.

Acknowledgements

First and foremost I would like to thank my supervisor Bernhard Mehlig, for taking me on as a student, guiding me through this PhD and putting up with my strong will. I would also like to thank Kristian Gustavsson, my co-supervisor, for interesting discussions and stability in an otherwise turbulent environment.

I would also like to extend my gratitude to Mattias Marklund, who stepped in as my examiner and always being an inspiration. My gratitude also extends to my study director Caroline for supporting me and making the PhD education a much better experience.

A huge thank you to my collaborators Fabien Candelier and Jan Meibohm for your incredible work and wisdom. Without your introduction to the field and your support, this thesis would not have been possible.

To the people currently and previously of Soliden 3, I thank you from the bottom of my heart for making work worth and fun. There are many more to thank for their company and friendliness, you know who you are, thank you!

To Julia, who I have had the privilege to share this (almost) 9 year journey through university with. Your endless patience, kindness, and humour has kept me (mostly) sane through out this time. I am very thankful to call you my friend.

Finally I want to say thank you to my family, for your endless support and love.

Linus Sundberg
Göteborg, Sweden
Mars 2026

CONTENTS

Abstract iii

Publications v

Acknowledgements vii

Contents ix

1 Introduction 1

2 Dynamics of particles in fluids 3
2.1 Navier-Stokes equations . . . 3
2.2 Disturbance flow . . . 4
2.3 Stokes flow . . . 5
2.4 Particle dynamics . . . 7

3 Caustic formation 9
3.1 Dynamics of particle-velocity gradients . . . 11
3.2 Statistical model of turbulence . . . 12
3.3 Path to caustic formation . . . 14
3.4 History effects and future projects . . . 17

4 Symmetry constraints on inertial torques 19
4.1 The force and torque on a particle in Stokes flow . . . 20
4.2 Inertial forces and torques on a particle . . . 21
4.3 Symmetry considerations . . . 24
4.4 Examples . . . 25
4.5 Perturbation theory - addition of symmetries . . . 29
4.6 Conclusions and outlook . . . 31

5 Settling dynamics of fibres 33
5.1 Stokes limit . . . 34
5.2 Inertial torques on slender bodies . . . 35
5.3 Curved fibres settling in quiescent fluid . . . 36
5.4 Conclusions and further work . . . 37

6 Conclusion 39

References 41

Research papers 47

1 Introduction

The dynamics of particles suspended in fluids is important in many scientific and engineering problems. Turbulent motion of the fluid can enhance mixing [1, 2], the turbulent atmosphere transports microplastic particles [3–6], and turbulence mixes water droplets in clouds [7–9]. The key difficulty in turbulent particle suspensions is the non-linear interaction between the particle and the fluid; the particles move according to forces and torques imparted by the fluid upon the particles, while the presence of the particles changes the boundary conditions of the flow. In order to understand the dynamics of a large particle in a fluid, one must consider both the inertia of the particle and the fluid. Particle inertia is quantified by the dimensionless Stokes number St [10], and allows particles to detach from the flow, causing suspended particles to form inhomogeneous spatial patterns in incompressible turbulence [10–16]. Due to particle inertia, the particle velocity becomes multivalued in regions of configuration space when a caustic is formed. Such caustics are formed when the phase-space manifold for the particle dynamics folds over [8, 10, 15–17], resulting in particles having large relative velocities, leading to enhanced collision rates [18, 19]. Collisions between small water droplets are important in the growth of the water droplet size in clouds [7, 8]. For small Stokes numbers, $\mathrm{St} \ll 1$, caustic formation relies on rarely occurring large fluctuations of the fluid velocity gradients [10], which depend on the tails of the gradient distribution. In this thesis, statistical models for caustic formation are discussed.

In addition to particle inertia, fluid inertia is necessary to describe the dynamics of a large particle. The particle Reynolds number Re_p is a dimensionless measure of fluid-inertia effects on the length scale of the particle. The limit $\mathrm{Re}_p \to 0$ is known as the Stokes limit, where fluid inertia can be neglected. In this limit, the hydrodynamic force and torque depend linearly on the relative velocity and angular velocity between the particle and the fluid [20–24]. Fluid inertia changes the disturbances generated by the particle in the fluid. These disturbances, in turn induce inertial corrections to the hydrodynamic force and torque upon the particle [25, 26]. The magnitude and structure are determined by the particle Reynolds number and the symmetries of the particle.

This thesis consists of six chapters. Chapter 1 provides an overview of the background and describes the goals of the research summarised in this thesis. In Chapter 2, the concepts of fluid dynamics that are needed for Papers [I-III] are presented. Chapter 3 considers the effect of particle inertia on particle dynamics in a fluid flow, in particular the caustic formation mechanism which is the focus of Paper [I]. The statistical model proposed in Paper [I] is described in the chapter. A one-dimensional version is used in the chapter, which allows mathematical analysis.

Finally, the thesis concludes with a discussion of possible implications of the Basset-Boussinesq-Oseen history effects on caustic formation. In Chapter 4, the effect of fluid inertia on the dynamics of particles in a fluid is considered, where particle-shape symmetries constrain the form of Re_p-corrections to hydrodynamic force and torque [III]. In the chapter it is explained how these inertial corrections are constrained, and the key idea is illustrated for three different cases (three different groups of particle-shape symmetries). The method of constraining the inertial correction to the torque, described in Chapter 4, is used to constrain the torques on a curved fibre. The predicted torque is used in Chapter 5 to discuss the settling dynamics of curved fibres, which is the topic of Paper [II]. Chapter 6 summarises the results presented in this thesis and Papers [I-III], concluding with an outlook on the most important research questions which have yet to be answered.

2 Dynamics of particles in fluids

Suspended particles in fluids form a coupled dynamical system. The governing equations for the fluid are the Navier-Stokes equations, Eq. (2.1), where the presence of the particle dictates the boundary condition for the fluid velocity [27]. In turn, the particles experience the forces and torques generated by the surrounding fluid [23]. Thus, it is not possible to fully separate the dynamics of either part from the other, in general. A solution is to consider the effect of the particles to be a small disturbance to the flow. In Section 2.1, the Navier-Stokes equations are briefly introduced and rewritten in a non-dimensional form, using the particle Reynolds number and the Strouhal number. The Strouhal number is a non-dimensional measure of unsteadiness of the flow, that is, the importance of time variability in the flow compared with convection. Section 2.2 derives the dynamics of the disturbance flow. In addition, Section 2.3 briefly discusses the limit of no fluid inertia, known as the Stokes limit. The forces and torques on a particle from fluids are covered in Section 2.4.

2.1 Navier-Stokes equations

The Navier-Stokes equations (NSE) describe the dynamics of the fluid velocity $\boldsymbol{u}(\boldsymbol{x}, t)$ and the pressure field $p(\boldsymbol{x}, t)$ in the fluid. The equations for an incompressible flow are [24, 27–29]

$$\rho\left(\frac{\partial \boldsymbol{u}}{\partial t} + (\boldsymbol{u}\cdot\nabla)\boldsymbol{u}\right) = \mu\Delta\boldsymbol{u} - \nabla p + \boldsymbol{f} \tag{2.1}$$

for an external forcing per unit volume $\boldsymbol{f}$. The left hand side is the time derivative of the flow along a streamline, called the material derivative [24]. The fluid velocity changes partly due to variations in time, but also from the moving reference frame. The left hand side has the form of a mass multiplied by an acceleration, as per Newton's second law, is referred to as inertial terms. The right hand side contains the forcing due to pressure differentials in the flow $-\nabla p$, the forcing $\boldsymbol{f}$ caused by external forces on the fluid, and the viscous term $\mu\Delta\boldsymbol{u}$. The viscous term is an internal friction between fluid layers [27].

A simple solution to the Navier-Stokes equations is a homogeneous quiescent fluid subjected to gravity. In a homogeneous quiescent fluid, $\boldsymbol{u} = 0$, and the density is constant, ρ, throughout the fluid. Taking the gravitational field to be in the negative $\boldsymbol{e}_z$-direction, Eq. (2.1) becomes

$$-\nabla p - \rho g \boldsymbol{e}_z = 0. \tag{2.2}$$

We impose the boundary condition that the pressure $p = 0$ on the surface $z = 0$, gives the solution $p = -\rho g z$ to Eq. (2.2).

The pressure p enters linearly into Eq. (2.1) through $-\nabla p$. By redefining the pressure as $p = p' - \rho g z$, the gravitational effects can be treated separately, and the resulting equation becomes

$$\rho\left(\frac{\partial \boldsymbol{u}}{\partial t} + (\boldsymbol{u}\cdot\nabla)\boldsymbol{u}\right) = \mu\Delta\boldsymbol{u} - \nabla p'. \tag{2.3}$$

The hydrodynamic pressure p' is determined by the motion of the fluid. In the remainder of the thesis, p will always refer to the hydrodynamic pressure, unless otherwise stated.

For convenience, it is common to rewrite the Navier-Stokes equations in non-dimensional form using a characteristic length, velocity, time, and pressure scale, a, U, τ and $\mu U/a$ respectively. Here, in preparation for Chapters 3, 4, and 5, the length scale is the size of a particle. Substituting

$$\boldsymbol{r} \to a\boldsymbol{r}, \quad \boldsymbol{u} \to U\boldsymbol{u}, \quad t \to \tau t, \quad p \to \frac{\mu U}{a} p, \tag{2.4}$$

into Eq. (2.3), one finds the non-dimensional form

$$\mathrm{Re}_p\left(\mathrm{Sl}\frac{\partial \boldsymbol{u}}{\partial t} + (\boldsymbol{u}\cdot\nabla)\boldsymbol{u}\right) = \Delta\boldsymbol{u} - \nabla p. \tag{2.5}$$

Here, the particle Reynolds number is $\mathrm{Re}_p = \frac{aU\rho}{\mu}$, or using the kinematic viscosity, $\mathrm{Re}_p = \frac{aU}{\nu}$, and $\mathrm{Sl} = \frac{a}{U\tau}$ is the Strouhal number [30]. The subscript p indicates that the Reynolds number is based on the characteristic scales involved for a flow around a particle. The particle Reynolds number is a non-dimensional number describing the ratio between the inertial effect due to convection and the viscous effect of the fluid [31]; thus it measures the importance of fluid inertia in the flow around the particle. When the particle Reynolds number is small, inertial effects in the fluid are small. The limit of $\mathrm{Re}_p \to 0$ is known as the Stokes limit where the flow has a creeping motion [24].

2.2 Disturbance flow

If a particle is inserted into an undisturbed fluid flow $\boldsymbol{U}^{(\infty)}(\boldsymbol{x}, t)$ with undisturbed field pressure $p^{(\infty)}(\boldsymbol{x}, t)$ that satisfies Eq. (2.5), the problem changes due to an additional boundary condition on the surface of the particle. The fluid flow that satisfies Eq. (2.5) with the boundary condition on the particle surface is taken to be $\boldsymbol{u}(\boldsymbol{x}, t)$ with pressure $p(\boldsymbol{x}, t)$. The difference between the flow with the particle and the

undisturbed flow defines the disturbance flow $\boldsymbol{w}(\boldsymbol{x},t)=\boldsymbol{u}(\boldsymbol{x},t)-\boldsymbol{U}^{(\infty)}(\boldsymbol{x},t)$, and the disturbance pressure equivalently as $p'(\boldsymbol{x},t)=p(\boldsymbol{x},t)-p^{(\infty)}(\boldsymbol{x},t)$. The disturbance flow then must satisfy

$$\mathrm{Re}_p\left(\mathrm{Sl}\frac{\partial \boldsymbol{w}}{\partial t}+(\boldsymbol{U}^{(\infty)}\cdot\nabla)\boldsymbol{w}+(\boldsymbol{w}\cdot\nabla)\boldsymbol{U}^{(\infty)}+(\boldsymbol{w}\cdot\nabla)\boldsymbol{w}\right)=\Delta\boldsymbol{w}-\nabla p' \tag{2.6}$$

in the laboratory frame.

It is sometimes more convenient to solve the disturbance flow for moving particles in a reference frame moving with the particle. In a reference frame moving with the centre of mass of the particle, any position vector in the laboratory frame can be expressed as a position vector $\boldsymbol{r}$ relative to the centre of mass of the particle $\boldsymbol{x}_p(t)$, through $\boldsymbol{x}=\boldsymbol{x}_p(t)+\boldsymbol{r}$. The change of coordinate system implies that the derivatives become

$$\begin{aligned}\nabla_x&=\nabla_r,\\ \left.\frac{\partial}{\partial t}\right|_x&=\left.\frac{\partial}{\partial t}\right|_r-\frac{a}{U\tau}(\dot{\boldsymbol{x}}_p\cdot\nabla_r)=\left.\frac{\partial}{\partial t}\right|_r-\mathrm{Sl}^{-1}(\dot{\boldsymbol{x}}_p\cdot\nabla_r),\end{aligned} \tag{2.7}$$

where the inverse Strouhal number appears because velocities being measured using the characteristic velocity U, while the time and space derivatives are made non-dimensional from τ and a, respectively. When inserted back into Eq. (2.6), we find

$$\mathrm{Re}_p\left(\mathrm{Sl}\frac{\partial \boldsymbol{w}}{\partial t}-(\dot{\boldsymbol{x}}_p\cdot\nabla)\boldsymbol{w}+(\boldsymbol{U}^{(\infty)}\cdot\nabla)\boldsymbol{w}+(\boldsymbol{w}\cdot\nabla)\boldsymbol{U}^{(\infty)}+(\boldsymbol{w}\cdot\nabla)\boldsymbol{w}\right)=\Delta\boldsymbol{w}-\nabla p', \tag{2.8}$$

where the spatial derivatives are taken with respect to $\boldsymbol{r}$ and the time derivative is taken keeping $\boldsymbol{r}$ constant.

The boundary condition for the flow $\boldsymbol{u}(\boldsymbol{x},t)$ on the surface of a solid particle is the no-slip boundary condition $\boldsymbol{u}(\boldsymbol{x},t)=\dot{\boldsymbol{x}}_p(t)$ [27]. The disturbance flow thus must satisfy

$$\boldsymbol{w}(\boldsymbol{r},t)=\dot{\boldsymbol{x}}_p(t)-\boldsymbol{U}^{(\infty)}(\boldsymbol{r},t) \tag{2.9}$$

on the surface of the particle. Very far from the particle surface, the effect of the particle is assumed to vanish, leading to the boundary condition $\boldsymbol{w}\to 0$ when $|\boldsymbol{r}|\to\infty$.

2.3 Stokes flow

In the Stokes limit, $\mathrm{Re}_p\to 0$, the fluid inertial effect is completely disregarded [23, 24]. It follows that Eq. (2.8) reduces to [23]

$$\Delta\boldsymbol{w}-\nabla p=0,\quad \nabla\cdot\boldsymbol{w}=0. \tag{2.10}$$

The flow described by the solution of the Stokes equation is called a Stokes flow. The solution can be found using the general solution to the Stokes problem constructed by Lamb (the Lamb solution) [23, 24]. The linearity of the Stokes equation (2.10) allows for solutions to be built by superposition and provides a good approximation for the flow around the particle up to distances of $\mathcal{O}(\mathrm{Re}_p^{-1})$ (in units of a) [24].

The incompressibility condition, $\nabla \cdot \boldsymbol{w} = 0$, implies that the disturbance pressure must solve the Laplace equation,

$$\Delta p = 0. \tag{2.11}$$

For the case of spherical geometry, the general solution for the disturbance pressure can be written in terms of spherical harmonics

$$p = \sum_{n=-\infty}^{\infty} p_n = \sum_{n=-\infty}^{\infty} r^n \sum_{l=0}^{n-1} \sum_{m=-l}^{l} a_{nm}^l Y_l^m(\theta, \varphi), \tag{2.12}$$

where coefficients a_{nm}^l allow for any general mode to be included. The Lamb solution for the disturbance flow is [23, 24]

$$\boldsymbol{w} = \sum_{n=-\infty}^{\infty} \left[\nabla \times (\chi_n \boldsymbol{r}) + \nabla \phi_n + \frac{n+3}{2(n+1)(2n+3)} r^2 \nabla p_n - \frac{n}{(n+1)(2n+3)} p_n \boldsymbol{r} \right], \tag{2.13}$$

where χ_n and ϕ_n are spherical harmonic functions, similar to p_n.

One could add a forcing term to the homogeneous Stokes equation that has so far been described. The forcing term then results in

$$\Delta \boldsymbol{w} - \nabla p = -\boldsymbol{f}, \tag{2.14}$$

which, apart from the homogeneous solution found using the Lamb solution, has a particular solution to account for the forcing. By taking the divergence of Eq. (2.14), the equation for the pressure becomes

$$\Delta p = \nabla \cdot \boldsymbol{f}. \tag{2.15}$$

The particular solution of the disturbance flow $\boldsymbol{w}$ in Eq. (2.14) is given by

$$\boldsymbol{w}(\boldsymbol{x}) = \int_{\mathbb{R}^3} \mathrm{d}\boldsymbol{x}' \frac{1}{8\pi|\boldsymbol{x}-\boldsymbol{x}'|} \left(\mathbb{I} + \frac{(\boldsymbol{x}-\boldsymbol{x}') \otimes (\boldsymbol{x}-\boldsymbol{x}')}{|\boldsymbol{x}-\boldsymbol{x}'|^2} \right) \cdot \boldsymbol{f}(\boldsymbol{x}'), \tag{2.16}$$

where $\mathbb{I}$ is the 3×3 identity matrix.

2.4 Particle dynamics

The dynamics of the particles are described by Newton's second law of motion,

$$\rho_p V \dot{\boldsymbol{v}} = \rho_p V \boldsymbol{g} + \boldsymbol{F}_{\text{fluid}}, \tag{2.17}$$

where V is the volume, ρ_p the density, and $\dot{\boldsymbol{v}}$ the acceleration of the particle. Here, $\rho_p V \boldsymbol{g}$ is the force from the external gravitational field and $\boldsymbol{F}_{\text{fluid}}$ is the force imparted on the particle from the fluid. The force $\boldsymbol{F}_{\text{fluid}}$ is calculated by integrating the normal component of the stress tensor $\boldsymbol{\sigma} \cdot \hat{\boldsymbol{n}}$ over the surface of the particle [27]

$$\boldsymbol{F}_{\text{fluid}} = \int_{\partial V} \boldsymbol{\sigma} \cdot \hat{\boldsymbol{n}} \, \mathrm{d}S, \tag{2.18}$$

where ∂V denotes the surface of the particle. The stress tensor $\boldsymbol{\sigma}$ depends on the disturbance flow $\boldsymbol{w}$ and the pressure field p within the fluid as

$$\sigma^{ij} = 2\mu \partial^{(i} w^{j)} - p\delta^{ij} = 2\mu S^{ij} - p\delta^{ij}, \tag{2.19}$$

where $S^{ij} = \frac{1}{2}(\partial^i w^j + \partial^j w^i)$ is the strain rate tensor.

In Section 2.1 it was shown that gravity results in a spatially varying pressure field, $p = -\rho_f g z$, which yields the stress tensor $\sigma^{ij} = \rho_f g z \delta^{ij}$. The force on a spherical particle with radius a, found from Eq. (2.18), is

$$\boldsymbol{F}_{\text{fluid}} = \int_0^{\pi} 2\pi \rho_f g a^3 \cos^2\theta \sin\theta \, \mathrm{d}\theta \, \boldsymbol{e}_z = V \rho_f g \boldsymbol{e}_z = -V \rho_f \boldsymbol{g}. \tag{2.20}$$

This is the buoyancy force, that acts to oppose gravity [23, 24]. Using Gauss's theorem [32], the equation can be shown to be true for any shape.

The buoyancy force originates from the pressure and the external gravity field. The Navier-Stokes equations are linear in pressure, which leads to the contribution from the stationary solution can be separated out from those forces and torques which arise from a fluid in motion. This leads to the equation of motion for the particle

$$\rho_p V \dot{\boldsymbol{v}}_p = (\rho_p - \rho_f) V \boldsymbol{g} + \boldsymbol{F}_{\text{h}}, \tag{2.21}$$

where the hydrodynamic force $\boldsymbol{F}_{\text{h}}$ is calculated using Eq. (2.18) with the stress tensor

$$\sigma'^{ij} = 2\mu \partial^{(i} w^{j)} - p' \delta^{ij}, \tag{2.22}$$

corresponding to the disturbances of the particle. From this point onwards, the primes are omitted, and the pressure referred to is the disturbance pressure.

The Stokes limit, $\mathrm{Re}_p \to 0$, was briefly introduced in Section 2.3. In this limit, the hydrodynamic force on a spherical particle with radius a is proportional to the relative velocity between the fluid $\boldsymbol{U}^{(\infty)}$ and the particle $\boldsymbol{v}$ [23, 24, 27, 33]

$$\boldsymbol{F}_\mathrm{h} = 6\pi\nu\rho_f a(\boldsymbol{U}^{(\infty)} - \boldsymbol{v}). \tag{2.23}$$

For a particle moving with the same velocity as the surrounding fluid, the hydrodynamic force acting on the particle vanishes. The minus sign in front of $\boldsymbol{v}$ makes the force act as a damping term, which results in the particle velocity relaxing to the driving due to gravity and the flow [27].

The inertial effects of a flow which changes rapidly in time (unsteadiness), such that $\mathrm{Re}_p\,\mathrm{Sl} = a^2/(\tau\nu)$ is non-zero, introduces interactions of the disturbance fields generated by previously relative motions of the particle and fluid. The forces the particle experiences become dependent on the history of the relative acceleration between the fluid and the particle [34, Sec. 20.2]. The resulting time-dependent force on a sphere is the Basset-Bossinesq-Oseen (BBO) force [35–37]:

$$\boldsymbol{F}_\mathrm{BBO}(t) = 6a^2\rho_f\sqrt{\pi\nu}\int_0^t \frac{\frac{\mathrm{d}}{\mathrm{d}\tau}\{\boldsymbol{u}[\boldsymbol{x}_p(\tau)] - \boldsymbol{v}(\tau)\}}{\sqrt{t-\tau}}\mathrm{d}\tau. \tag{2.24}$$

The BBO force disregards other effects of fluid inertia proportional to the particle Reynolds number. Candelier et al. [38] derived a history force for large particles that includes effects of fluid-gradients and inertial corrections. Their results show that the history force takes a different form when higher order inertial terms are included. They show that the $1/\sqrt{t-\tau}$ kernel is not complete and that the exact form is not fully known to arbitrary expansion order in $\mathrm{Re}_p\,\mathrm{Sl}$.

The fluid can also exert a torque on the particle. In analogy to Eq. (2.18), the torque that acts on the particle can be calculated by

$$\boldsymbol{T}^{(c)}_\mathrm{fluid} = \int_{\partial V} \boldsymbol{r}^{(c)} \times (\sigma\cdot\hat{\boldsymbol{n}})\,\mathrm{d}S, \tag{2.25}$$

where the position vector $\boldsymbol{r}^{(c)}$ is defined relative to the chosen reference point (c) about which the torque is calculated. The dynamics of the particle is independent of the choice of reference point. Using the parallel-axis theorem, the torque can be translated between points [23]. This allows for the calculation to be performed using the reference point that is most convenient and then mapped to the centre of mass about which rotations occur for a free particle.

3 Caustic formation

The dynamics of small particles in a turbulent fluid is encountered in engineering and science. The clustering mechanism of small particles in turbulence is of crucial importance in understanding the evolution of the droplet-size distribution in clouds [9], and in collisions of dust particles in the protoplanetary disc, where collisions can lead to fragmentations or merger of the particles [12, 39]. In both of these applications, inertia is a key factor. There are two types of inertia involved in the system. The first is that of the fluid, which affects how resistant the fluid is to changes. For very small particles, the particle Reynolds number Re_p is small, and therefore the fluid is barely affected by the presence of the particles. The second type of inertia is the particle inertia. The Stokes number St is a measure of particle inertia, determining how responsive the particle is to changes in the relative motion between the particle and fluid [10].

Particle inertia allows suspended particles in a turbulent flow to detach from the flow lines. The particles can then cluster in regions of space and form fractal spatial patterns [13–15]. In flows with high vorticity, the flow changes rapidly and particles with $\mathrm{St} \neq 0$ can detach from the flow and be centrifuged out [2, 11, 12, 14]. As a result, particles tend to accumulate in regions of low vorticity [2, 11]. This phenomenon is called preferential concentration and it increases the probability that a particle experiences higher strain. Preferential concentration due to being centrifuged out of high vorticity regions is less prevalent when the Stokes number is of order one [12]. The instantaneous fluid-velocity gradients become less important when particle inertia increases and the history of the fluid-velocity gradient becomes more important [10].

Saffman and Turner [7] derived a model for the growth of water droplets within clouds because of collisions which are driven by turbulence and gravity. The collision rate between two droplets of similar size depends on the relative velocity. In their model, they estimate the distribution of relative velocities assuming that the droplets follow the flow, which implies that $\mathrm{St} = 0$. Particles with $\mathrm{St} \neq 0$ detach from the flow and the particle velocities in certain regions in space can be multivalued [8]. The multivalued particle velocities are formed at singular points in configuration space where the phase-space manifold folds over [8, 10, 15–17]. The point at which the phase-space manifold folds over is called a caustic, and this leads to a region of many-to-one velocities in the vicinity thereof [16, 18, 19]. The multivalued velocity of the particles gives rise to large relative velocities for nearby particles which allows the particles to collide [18, 19, 40]. To investigate the effect of particle inertia on caustic formation, Wilkinson and Mehlig [17] employed a mathematical model for the distribution of fluid-velocity gradients to model particles in a turbulent flow.

For an inertial particle in turbulence, the fluid-velocity gradients it experiences along its path are hard to predict. The non-linearity of the Navier-Stokes equations, which govern the evolution of the fluid velocity, makes the flow along the particle trajectory analytically intractable. One possible approach is to use direct numerical simulation (DNS) to compute the fluid-velocity gradients and trajectories of the particles. DNS is computationally costly and gives limited insight into the mechanisms of caustic formation.

Another approach to theoretically study the caustic formation mechanism is to model the fluid-velocity gradients experienced by the particle with statistical models. This makes it possible to analytically derive results for the rate of caustic formation in different limits [10, 15]. The distribution of fluid-velocity gradients in turbulence is not known analytically, and hence must be modelled approximately. Depending on the model, different aspects of the distribution of fluid-velocity gradients in turbulence can be studied separately, such as the influence of heavy tails on caustic formation.

The probability distribution of the fluid-velocity gradients that an inertial particle experiences has been modelled in different ways and in different limits using statistical models. In the white-noise limit, the particle experiences an uncorrelated fluid-velocity gradient at each instant of time [14, 17]. The caustic formation rate is then treated as a diffusion problem, where the caustic rate formation was found to have an exponential scaling of St^{-1}. The white-noise limit has been asymptotically extended to the regime of short but non-zero time correlation [41]. The caustic formation rate was found to exponentially scale as St^{-2} in the small St limit and approach the scaling of the white-noise limit for large St. In the persistent limit, heavy particles experience gradients that vary slowly in time compared to the particle dynamics [18, 19, 42]. For the persistent limit, the process of caustic formation is initiated when the fluid-velocity gradients grow beyond a large threshold value [19]. It was seen for Gaussian models that caustics occur predominately in regions where the flow has high strain [18, 19]. In Paper [I] it was shown that for a non-Gaussian model the caustic forms in regions of high strain and low vorticity. The thesis considers only the persistent limit in the remaining chapter.

Section 3.1 describes the dynamics of particle-velocity gradients and introduces the non-dimensional Stokes number measuring particle inertia. Section 3.2 describes the statistical model used in Paper [I] for the distribution of fluid-velocity gradients experienced by the particles. In Section 3.3, a one-dimensional model of caustic formation is discussed, where the optimal path is compared to the distribution of simulated trajectories resulting in a caustic. Section 3.4 covers the attempts to include fluid-inertial and history effects and their impact on caustic formation. This

section also comments on possible future research directions.

3.1 Dynamics of particle-velocity gradients

Particles suspended in a moving fluid experience forces from the flow. In Section 2.4, the equation of motion of a spherical particle in a viscous fluid was described. When the particle is very small, such that the particle Reynolds number and the shear Reynolds number are negligible, effects of fluid inertia can be disregarded [15]. Mathematically, $\mathrm{Re}_p = \frac{a|\boldsymbol{u}-\boldsymbol{v}|}{\nu} \ll 1$ and $\mathrm{Re}_s = \frac{a^2 s}{\nu} \ll 1$, where a is the radius of the particle, $\boldsymbol{u}$ is the fluid velocity, $\boldsymbol{v}$ is the particle velocity, s is the shear rate (the magnitude of the imposed fluid-velocity gradients), and ν is the kinematic viscosity [15]. The force on the particle from the fluid is given by the Stokes drag, Eq. (2.23), and the equation of motion is given by

$$m_p \frac{\mathrm{d}\boldsymbol{v}}{\mathrm{d}t} = 6\pi\nu\rho_f a\,[\boldsymbol{u}(\boldsymbol{x}(t),t)-\boldsymbol{v}] + m_p\boldsymbol{g}, \tag{3.1}$$

for a particle with mass $m_p = \frac{4\pi a^3}{3}\rho_p$ located at $\boldsymbol{x}(t)$ at time t. By introducing the damping time scale $\tau_p = (2\rho_p a^2)/(9\nu\rho_f)$ [10], Eq. (3.1) becomes

$$\dot{\boldsymbol{v}} = \frac{1}{\tau_p}(\boldsymbol{u}-\boldsymbol{v}) + \boldsymbol{g}. \tag{3.2}$$

This equation describes the damped dynamics of the particle velocity, driven by the fluid velocity, with a damping time of τ_p. In the absence of gravity, the acceleration of the particle is only driven by the fluid velocity $\boldsymbol{u}$ the particle experiences as it moves through the turbulence. When the flow $\boldsymbol{u}(\boldsymbol{x}(t),t)$ changes slowly in space and time compared with the damping time, the particle velocity decays exponentially towards that of the fluid. The damping time scale is therefore also the response time of the particle to changes in the flow and consequently sometimes called "the response time".

Caustics are characterised by singular points in the phase space of the particle dynamics, resulting in a multivalued particle velocity field between points in space [8, 10, 15–17]. The many-to-one velocities in regions in space implies that particles can have a finite relative velocity between two infinitely close points [8]. The particle-velocity gradient $\mathbb{Z} = \tau_p \frac{\partial \boldsymbol{v}}{\partial \boldsymbol{x}}$, diverges at points when the phase space folds over. In three dimensions, this means that $|\mathrm{Tr}\,\mathbb{Z}| \to \infty$, since one of the eigenvalues blows up [17, 43].

The particle-velocity gradient evolves in time while the particle moves in the flow [8, 17]. Writing the particle-velocity gradient with index notation, with the definition

$Z_i{}^j = \tau_p \partial_i v^j$, and equivalently the fluid-velocity gradient $A_i{}^j = \tau_p \partial_i u^j$, the time evolution is given by

$$\begin{aligned}\frac{\mathrm{d}}{\mathrm{d}t} Z_i{}^j &= \tau_p \frac{\mathrm{d}}{\mathrm{d}t} \partial_i v^j = \tau_p \left(\partial_t \partial_i v^j + v^k \partial_k \partial_i v^j\right) \\ &= \tau_p \left(\partial_i \partial_t v^j + \partial_i (v^k \partial_k v^j) - (\partial_i v^k)\partial_k v^j\right) = \tau_p \partial_i \frac{\mathrm{d}v^j}{\mathrm{d}t} - \frac{1}{\tau_p} Z_i{}^k Z_k{}^j. \quad (3.3)\end{aligned}$$

Replacing the particle acceleration $\frac{\mathrm{d}\boldsymbol{v}}{\mathrm{d}t}$ in Eq. (3.3) with the equation of motion, found in Eq. (3.2), one finds the well-known result [8, 10, 18, 44]:

$$\dot{Z}_i{}^j = \tau_p \partial_i \left(\frac{1}{\tau_p}[u^j - v^j] + g^j\right) - \frac{1}{\tau_p} Z_i{}^k Z_k{}^j = \frac{1}{\tau_p}[A_i{}^j - Z_i{}^j - Z_i{}^k Z_k{}^j]. \quad (3.4)$$

In the persistent limit, the time scale on which the fluid gradient changes is the Kolmogorov time τ_K [15]. Writing Eq. (3.4) in dimensionless form by substituting $t \to t\tau_K$, using the Kolmogorov time as the time scale, yields

$$\mathrm{St}\, \dot{Z}_i{}^j = A_i{}^j - Z_i{}^j - Z_i{}^k Z_k{}^j. \quad (3.5)$$

In Eq. (3.5), $\mathrm{St} = \tau_p/\tau_k$ is the Stokes number. It compares how fast the particle relaxes to the flow with how fast the flow changes. When $\mathrm{St} = 0$, the particles relax instantly and follow the flow perfectly. For $\mathrm{St} \neq 0$, the flow the particles see along their trajectories can change faster than the relaxation time and the particles detach from the flow line. The distribution of fluid-velocity gradients the particle experiences along its trajectory is different from that of the fluid, since the particle can detach and preferentially sample regions with higher strain when the Stokes number is non-zero [10]. This makes it difficult to predict the time-dynamics of the fluid-velocity gradients $\mathbb{A}$. To accurately predict the gradients the particle experiences along its trajectory requires direct numerical simulation of the Navier-Stokes equations and the equation of motion for the particle. An alternative approach is to model the fluid-velocity gradients as a stochastic process.

3.2 Statistical model of turbulence

Statistical models are constructed using assumptions about the spatial and temporal correlations, together with flow-specific parameters which can be tuned to mimic characteristics of turbulence. Saffman and Turner [7] modelled the probability distribution of fluid-velocity gradients as a time-independent random Gaussian distribution with mean square value given in terms of the energy dissipation rate and kinematic viscosity of air estimated in different types of clouds. A time-dependent statistical model for turbulence in an incompressible fluid can be constructed from

a vector potential $\boldsymbol{\Psi}$, built up by random Fourier modes by $\boldsymbol{u} = \nabla \times \boldsymbol{\Psi}(\boldsymbol{x}, t)$ [10]. A Gaussian spatial correlation function is achieved by representing the vector potential as a Fourier series with Gaussian decaying spatial dependence and time-dependent random coefficients [15]. The spatial correlation function of the resulting model is determined by a single length scale l_0:

$$\langle \Psi_i(\boldsymbol{x}, t)\Psi_j(\boldsymbol{x}', t')\rangle = \mathscr{N}(u_0 l_0)^2 \delta_{ij} \exp\left\{-\frac{|\boldsymbol{x}-\boldsymbol{x}'|^2}{2l_0^2}\right\} f(t-t'). \tag{3.6}$$

The spatial correlation length l_0 and the root-mean-square velocity u_0 of the fluctuation velocities are model-specific parameters that determine the Kolmogorov time $\tau_K \sim l_0/u_0$ and can be chosen to match the turbulence in question [10]. The time correlation function $f(t-t')$ is determined by the stochastic process of the Fourier coefficients. The time dependence of the coefficients can be modelled by assuming they are described by an Ornstein-Uhlenbeck process [45], with a correlation time τ_0. The ratio between the two time scales defines the Kubo number $\mathrm{Ku} = u_0\tau_0/l_0$, determining the persistence of the flow. A large Kubo number implies that the flow changes slowly in time compared to how rapidly the fluid fluctuation is displaced by a correlation length. The limit $\mathrm{Ku} \to \infty$ is the persistent limit, as the gradients are persistent in time. The limit of $\mathrm{Ku} \to 0$ with KuSt being constant is the white-noise limit where the fluid-velocities change rapidly in time. For an extensive review of statistical models and these limits see Ref. [15] and the references therein.

The aim of Paper [I] is to investigate the effect of heavy tails on the caustic formation rate, inspired by the existence of non-Gaussian tails of the fluid-velocity gradients found in turbulence. Consequently, we propose a non-Gaussian model. The model is constructed from

$$\boldsymbol{u}(\boldsymbol{x}, t) = \frac{1}{\sqrt{M}} \sum_{\alpha=1}^{M} \boldsymbol{u}_\alpha(\boldsymbol{x}) c_\alpha(t), \tag{3.7}$$

with M time-independent random velocity fields $\boldsymbol{u}_\alpha(\boldsymbol{x})$, constructed from independent Gaussian random vector potentials. The time dependence was generated by multiplying each random velocity field $\boldsymbol{u}_\alpha(\boldsymbol{x})$ by an independent Ornstein-Uhlenbeck process $c_\alpha(t)$ [45, 46]. Each product has a non-Gaussian probability distribution, and gives a probability distribution of $\mathbb{A}(\boldsymbol{x}, t)$ that is non-Gaussian. For large $M \gg 1$, the central limit theorem applies for the sum, and the probability distribution for $\mathbb{A}(\boldsymbol{x}, t)$ converges to a Gaussian probability distribution [47].

3.3 Path to caustic formation

Caustics are rare events for small St, and where and how they occur depends sensitively on the fluid-velocity gradients in the vicinity of the particle's path. In Eq. (3.5), it was seen that the fluid-velocity gradient along the particle path drives the dynamics of the particle-velocity gradient. The question then becomes: what shape do the fluctuations of the fluid-velocity gradients have that result in caustic formation? In the process of caustic formation, $\mathrm{Tr}\,\mathbb{Z} \to -\infty$, one of the eigenvalues grows in magnitude until it diverges. To illustrate the process, we use a one-dimensional model. The one-dimensional system in dimensionless units is described by

$$\mathrm{St}\dot{z} = -z - z^2 + A, \tag{3.8a}$$

$$\dot{A}(t) = -A(t) + \Gamma(t), \tag{3.8b}$$

$$\langle \Gamma(t)\Gamma(t')\rangle = \mathrm{St}^2\delta(t-t'), \tag{3.8c}$$

where $\Gamma(t)$ is Gaussian white noise with zero mean, and the correlation time is taken to be the Kolmogorov time. The right hand side of Eq. (3.8a) can be rewritten as $-(z+1/2)^2 + A(t) + 1/4$, which shows that $A(t) < -1/4$ leads to a z that accelerates towards negative infinity. The particle-velocity gradient takes time to grow and therefore the fluid-velocity gradient has to be below $A(t) < -1/4$ for a sufficiently long time such that $z \ll -1$. This occurs when the fluid-velocity gradient has a fluctuation with a sufficient magnitude.

A large fluctuation is a rare event and that depends on the tails of the distribution. The fluctuation of the fluid-velocity gradient in the persistent limit that results in a caustic is an example of such an event [41]. The optimal fluctuation is found using large deviation theory for the probability of the system to take particular values. The probability distribution $P(z,a,t)$ of the system to be in (z,A) at a time t is given by the corresponding Fokker-Planck equation of Eq. (3.8a)[41, 46]

$$\frac{\partial}{\partial t}P(z,A,t) = \frac{\partial}{\partial z}\left[\frac{1}{\mathrm{St}}(z+z^2-A)P(z,A,t)\right] + \frac{\partial}{\partial A}\left[AP(z,A,t)\right] + \frac{1}{2}\mathrm{St}^2\frac{\partial^2}{\partial A^2}P(z,A,t). \tag{3.9}$$

To find the probability distribution, the so-called "shooting method" (SM) is employed [41]. The stationary probability distribution ($\frac{\partial P}{\partial t} = 0$) is assumed to have the shape

$$P(z,A) = \exp\left\{-\frac{1}{\mathrm{St}^2}S(z,A)\right\}. \tag{3.10}$$

The function $S(z,A)$ is called the action of the system, by analogy with the WKBJ approximation used in quantum mechanics [15, 47]. Rewriting the stationary version

of Eq. (3.9) in terms of the action $S(z,A)$ results in

$$0=\frac{1}{\mathrm{St}}(A-z-z^2)\frac{\partial S}{\partial z}-A\frac{\partial S}{\partial A}+\left(\frac{\partial S}{\partial A}\right)^2+\mathscr{O}(\mathrm{St}), \tag{3.11}$$

where we keep only terms up to $\mathscr{O}(\mathrm{St}^0)$. The equation has the same mathematical structure as that of Hamiltonian dynamics: $\mathscr{H}(z,A,p_z,p_A)=0$ in classical mechanics [48]. Therefore, we identify the two canonical momenta $p_z=\frac{\partial S}{\partial z}$ and $p_A=\frac{\partial S}{\partial A}$, which results in a Hamiltonian of the form

$$\mathscr{H}=\frac{1}{\mathrm{St}}(A-z-z^2)p_z-Ap_A+p_A^2. \tag{3.12}$$

The Hamiltonian dynamics gives the evolution of the coordinates and momenta as

$$\begin{aligned}
\frac{\mathrm{d}z}{\mathrm{d}t}&=\frac{\partial\mathscr{H}}{\partial p_z}=\frac{1}{\mathrm{St}}(A-z-z^2), \quad \frac{\mathrm{d}A}{\mathrm{d}t}=\frac{\partial\mathscr{H}}{\partial p_A}=-A+2p_A,\\
\frac{\mathrm{d}p_z}{\mathrm{d}t}&=-\frac{\partial\mathscr{H}}{\partial z}=\frac{1}{\mathrm{St}}(1+2z)p_z, \quad \frac{\mathrm{d}p_A}{\mathrm{d}t}=-\frac{\partial\mathscr{H}}{\partial A}=p_A-p_z,
\end{aligned} \tag{3.13}$$

which then governs the optimal fluctuation together with the constraint $\mathscr{H}=0$. The dynamics has three fixed points: the first is $(z,A,p_z,p_A)=0$, around which the dynamics is primarily located. In four-dimensional phase space, it has two unstable directions. The second fixed point is $(z,A,p_z,p_A)=(-1,0,0,0)$. To form a caustic, the path of the optimal fluctuation in phase space goes in a direction of the plane spanned by the two unstable directions and passes close to the second fixed point [41]. The optimal path is found by solving Eq. (3.13) with the starting position being slightly perturbed in an unstable direction, and requiring that the trajectory has the final state $p_z=p_A=0$ and $z\to-\infty$ at the finite caustic formation time t_c. The time t_c is the time when the phase space folds over and beyond that time the particle velocity field becomes multivalued.

The optimal path found from the shooting method, described above, with a Gaussian probability distribution for A is compared to numerical results of a one-dimensional version of the Gaussian model ($M=\infty$) and the non-Gaussian model ($M=1$), described in Section 3.2, in Figure 3.1. The numerical simulation is carried out by solving the one dimensional system,

$$\begin{aligned}
\mathrm{St}\,\dot{z}&=-z-z^2+A,\\
A(t)&=\frac{1}{\sqrt{M}}\sum_{\alpha=1}^{M}A^\alpha c_\alpha(t),\\
\dot{c}_\alpha(t)&=-c_\alpha(t)+\Gamma_\alpha(t), \quad \alpha=1,\dots,M\\
\langle\Gamma_\alpha(t)\Gamma_\beta(t')\rangle&=\delta_{\alpha\beta}\delta(t-t'),
\end{aligned} \tag{3.14}$$

where A^α is given by a Gaussian random number with variance St^2 and $\Gamma_\alpha(t)$ being white noise with zero mean. The system is integrated until the numerical condition $z < -50$ is fulfilled and a caustic is regarded to have formed. The trajectory of $A(t)$ is then stored and the distribution of A at different times (normalised at each time step) is displayed in Figure 3.1 for $\mathrm{St} = 0.06$. The case ($M = \infty$) in the figure shows

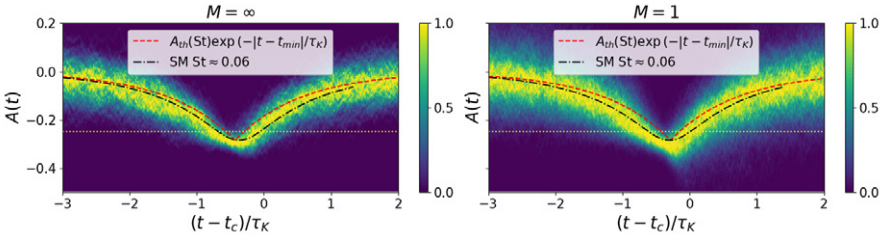

Figure 3.1: The figure shows the distribution the paths of fluid-velocity gradient that resulted in a caustic forming in a one-dimensional model for $\mathrm{St} = 0.06$ together with the dotted line indicating $A = -1/4$. The optimal path from the Shooting method (SM) assuming a Gaussian probability distribution and the correlation function with a Stokes dependent amplitude $A_{\mathrm{th}}(\mathrm{St})$ was plotted for comparison. The left panel shows the result of numerical results of the model using a Gaussian model given in Eq. (3.8). The right panel shows the distribution of trajectories conditioned on caustic formation for the non-Gaussian model in Eq. (3.14) with $M = 1$. The colour shows the probability distribution of the paths, normalised to unity at each instant of time t.

the numerical result of the Gaussian model for the distribution of fluid-velocity gradients, which shows that the distribution of trajectories that lead to caustic formation is close to the optimal path found from the shooting method. The trajectories tend to, in contrast, have a larger maximal value of $-A$. The shape is also compared with the time-correlation function $A_{\mathrm{th}}(\mathrm{St})e^{-|t|}$, with a Stokes-dependent prefactor $A_{\mathrm{th}}(\mathrm{St})$ centred at the time t_{min} at which the maximum value of $-A$ occurs. Both the probability distribution and the optimal path found from the shooting method are approximately the same shape as the correlation function, although smoother. The optimal fluctuation is thus influenced by the correlation function, which was also found for the Gaussian model in Refs. [18, 19].

The non-Gaussian model with $M = 1$ in Fig. 3.1 is compared with the same optimal path found from the shooting method with a Gaussian distribution. The model is also compared with the correlation function scaled with the Stokes-dependent maximum value $A_{\mathrm{th}}(\mathrm{St})$. The figure shows that the distribution of trajectories has approximately the same shape as the optimal path from the shooting method. The scaled correlation function is also seen to approximate the trajectories. Comparing the Gaussian model $M = \infty$ with the non-Gaussian model $M = 1$, it may be seen

that the paths follow the correlation function in both cases, something which was proven in Paper [I], and mainly differ in the variance of the distribution at each instant of time. The non-Gaussian model tends to overshoot the optimal path more than the Gaussian, which could be explained by the heavy tails of the non-Gaussian model's allowing A to take larger values more frequently.

In both cases, the path to caustic formation is in good agreement with the scaled time-correlation function, $A(t) = A_{\text{th}}(\text{St})e^{-|t|}$, with $A_{\text{th}}(\text{St}) + 1/4 \propto \text{St}^{2/3}$. The interpretation of A_{th} as an effective threshold, which the fluctuation must surpass for a caustic to form, can be compared with the approximate condition Bätge, Fouxon, and Wilczek [49] found for a combination of depth and the time the fluctuation was below $-1/4$. In the statistical model the time interval the fluctuation is smaller than $-1/4$, is determined by the shape of the correlation function and the minimal value it takes. Here the correlation function is exponential and the time at which fixed points were absent is fully determined by the minimal value, i.e. the threshold. Therefore, the condition of Bätge, Fouxon, and Wilczek [49] is equivalent to requiring an effective threshold that the fluid-velocity gradients must surpass for the statistical model.

3.4 History effects and future projects

In the model used for studying caustics, the size of the particle is assumed to be very small, and the movement of the particle does not impact the fluid. The movement of particles generates disturbance flows that result in the history forces described in Section 2.4. Maxey and Riley [35] derived a force for particles due to fluid acceleration, added mass and the BBO history force [36, 37]. Recently, Rajarshi and Govindarajan [50] attempted to include the effects of fluid acceleration and added mass to understand how the fluid-velocity gradients, sampled by particles in their trajectories, change the condition on forming caustics. They found that particles that have lower $\mathscr{R}$ need to be subjected to higher strain for longer time to form a caustic, which causes the formation to be rarer in 2D turbulence. However, the case in 3D has not been investigated and neither have the effects of the history force.

The effect of the history force has been hypothesised to hinder caustic formation, as the history force makes the inertial particles act as tracers ($\text{St} = 0$) [51]. It remains an open question to what extent the BBO history force affects the caustic-formation rate. When including the effect of inertial forces on a spherical particle, Eq. (3.2) is

replaced by [35]

$$\frac{\mathrm{d}\boldsymbol{v}}{\mathrm{d}t} = \alpha\boldsymbol{g} + (1-\alpha)\left(2\frac{D\boldsymbol{u}}{Dt} + \frac{\mathrm{d}\boldsymbol{u}}{\mathrm{d}t}\right) + \frac{\alpha}{\tau_p}(\boldsymbol{u}-\boldsymbol{v}) + \sqrt{\frac{36}{\pi}\frac{1}{2\mathscr{R}\tau_p}}\int_0^t \frac{\frac{\mathrm{d}}{\mathrm{d}s}[\boldsymbol{u}(s)-v(s)]}{\sqrt{t-s}}\mathrm{d}s, \tag{3.15}$$

where $\alpha = 2\mathscr{R}/(2\mathscr{R}+1)$ and $\mathscr{R} = \rho_p/\rho_f$. For heavy particles, the density ratio becomes very large, $\mathscr{R} \gg 1$ and α can be expanded as a power-series $\alpha \approx 1 - \frac{1}{2\mathscr{R}} + \mathscr{O}\left((\frac{1}{2\mathscr{R}})^2\right)$. Using the expansion of α and rewriting the equation in terms of non-dimensional time, i.e. $t \to \tau_K t$, the non-dimensional equation becomes

$$\begin{aligned}\frac{\mathrm{d}\boldsymbol{v}}{\mathrm{d}t} = \mathrm{Fr}^{-1}\,\boldsymbol{g} + \frac{1}{\mathrm{St}}(\boldsymbol{u}-\boldsymbol{v}) + \frac{1}{\sqrt{2\mathscr{R}}}\sqrt{\frac{36}{\pi}\frac{1}{\mathrm{St}}}\int_0^t \frac{\frac{\mathrm{d}}{\mathrm{d}s}[\boldsymbol{u}(s)-v(s)]}{\sqrt{t-s}}\mathrm{d}s \\ + \frac{1}{2\mathscr{R}}\left(2\frac{D\boldsymbol{u}}{Dt} + \frac{\mathrm{d}\boldsymbol{u}}{\mathrm{d}t} - \mathrm{Fr}^{-1}\,\boldsymbol{g} - \frac{1}{\mathrm{St}}(\boldsymbol{u}-\boldsymbol{v})\right) + \mathscr{O}\left(\left(\frac{1}{2\mathscr{R}}\right)^2\right),\end{aligned} \tag{3.16}$$

where $\mathrm{Fr} = g\tau_k/u_K$ is the Froude number and u_K is the Kolmogorov velocity [10]. From Equation (3.16) it is seen that in the limit $\mathscr{R} \to \infty$, holding St is constant, the particles are governed by the Stokes drag. The next highest order correction to the force of the particle depends on $\mathrm{St}/\mathscr{R}$. For $\mathrm{St}/\mathscr{R} \gg 1$, the history force dominates over the corrections due to added mass. In contrast, added mass is predicted to be of higher importance when $\mathrm{St}/\mathscr{R} \ll 1$.

For water droplets in air, where $R = \rho_p/\rho_f \approx 1000$ and $\alpha \approx 1$, Olivieri et al. [52] showed that the history force was the major contributor to the forces acting on the particles besides the Stokes drag. The history force provides an interesting aspect to investigate in terms of its effect on the caustic formation. Olivieri et al. [52] also showed that for heavy particles, the history effects were most notable at higher Stokes numbers, with little to no difference for small St.

The expression for the added mass has been discussed in Refs. [35, 38], and the exact expression to a general order in inertial corrections remains unclear. Candelier et al. [38] derived a kernel for the history force which depends on the surrounding flow to second order in inertial corrections. The question regarding if the BBO history force prevent caustic formation remains open. The history force of Candelier et al. included higher order inertial corrections which might affect the caustic formation, which also remains unclear at this point.

4 Symmetry constraints on inertial torques

Particles experience forces and torques given by the disturbance flow and pressure on their surfaces according to Eq. (2.18) and (2.25). It is expected that the symmetries a particle possesses affect the hydrodynamical force and torque, as the particle surface provides the inner boundary condition for the disturbance flow. This leads to the question: how do particle-shape symmetries constrain the hydrodynamical force and torque? In the Stokes limit, Happel and Brenner [23] used transformation properties, together with the requirement that the energy dissipation is a scalar, to derive a constraint for the resistance tensors. The symmetry restrictions of the force and torque were further developed to include a shear coupling in the Stokes limit [22, 53, 54].

When particles are sufficiently large or move too quickly, such that fluid inertial effects need to be considered, the Stokes approximation breaks down; it neglects the effect of fluid inertia on the disturbance flow. The importance of fluid inertia is measured by the dimensionless particle Reynolds number, Re_p, and it leads to corrections to the stress tensor. The inertial corrections to the stress tensors give rise to inertial forces and torques that the particle experiences. Brenner and Cox [25] investigated the leading-order corrections in Re_p to the force and found that the corrections are given by a polynomial in the velocity. Cox [26] extended the theory to consider the torque and included the angular velocity. Brenner and Cox [25] considered particle-shape symmetries that result in the quadratic terms of the inertial correction vanishing. The analysis was limited to effects of reflection and rotational symmetries of either $\pi/2$ or π radians. Cox [26] performed a similar analysis, where the torque or its components vanished under the same set of particle-shape symmetries.

Recently, there has been interest in how non-spherical particles settle [55–61], which was the focus of Paper [II]. Inertial torque has been observed to play a role in determining the orientation in which particles settle [26, 55, 58]. The torque on, and consequently the angular dependence of, settling particles strongly influences how they are transported [56, 62, 63]. Constraining the torque from particle-shape symmetry then provides models for understanding experimental results or ansatzes used in *ab initio* simulations [64].

In Paper [III], the method to constrain the inertial corrections to the torque from particle-shape symmetries is further extended to include unsteady effects. The paper focuses on reducing the degrees of freedom in the inertial correction to the torque, going beyond cases where the torque vanishes. The present chapter is devoted to explaining how the particle-shape symmetries constrain the force and

torque in the previously studied Stokes limit, and it also introduces the constraints for the inertial torque.

Section 4.1 introduces the Stokes forces and torques for general particle shape. The inertial corrections to the force and torque are discussed in Section 4.2 for low particle Reynolds number. In Section 4.3, the particle-shape symmetry constraint is derived for the inertial correction together with the known Stokes case. The resulting constraints are then applied to a spheroid, cube, and curved fibre in Section 4.4. The last example will be revisited in Chapter 5. Section 4.5 outlines how multiple symmetry-breaking effects interact. Finally, Section 4.6 summarises this chapter and presents an outlook.

4.1 The force and torque on a particle in Stokes flow

In Section 2.3 the Stokes flow for a spherical particle is discussed. For a particle that is not a sphere, the force and torque it experiences can depend on the orientation of the particle. Assuming the largest dimension of the particle is a, all distances in the problem can be defined in terms of a by letting $\boldsymbol{r} \to a\boldsymbol{r}$. Using a characteristic velocity scale v_0 to write the velocity in non-dimensional form as $\boldsymbol{w} \to v_0\boldsymbol{w}$ and the angular velocity $\boldsymbol{\omega} \to \frac{v_0}{a}\boldsymbol{\omega}$ results in the non-dimensional force and torque as follows

$$\boldsymbol{F} \to (\nu\rho_f v_0 a)\,\boldsymbol{F}, \tag{4.1a}$$

$$\boldsymbol{T} \to (\nu\rho_f v_0 a^2)\,\boldsymbol{T}. \tag{4.1b}$$

We assume the particle Reynolds number $\mathrm{Re}_p = a v_0/\nu$ based on the velocity scale is small, and the magnitude of the relative velocity between the flow and the particle on the surface, the slip velocity, is bounded from above by v_0.

The Stokes limit is thus found when the particle Reynolds number, based on the characteristic velocity, approaches zero, $\mathrm{Re}_p \to 0$, resulting in Eq. (2.10). The linearity of the Stokes equation allows for problems to be subdivided [20–23]. For a particle that both travels with velocity $\boldsymbol{v}$ and rotates with angular velocity $\boldsymbol{\omega}$ in a fluid with a velocity $\boldsymbol{u}^{(\infty)}$ and vorticity $\boldsymbol{\Omega}^{(\infty)}$, the disturbance flow $\boldsymbol{w}$ satisfies $\boldsymbol{w} = (\boldsymbol{v} - \boldsymbol{u}^{(\infty)}) + (\boldsymbol{\omega} - \boldsymbol{\Omega}^{(\infty)}) \times \boldsymbol{r}$ on the particle surface. Here, $\boldsymbol{r}$ is the position vector of a point on the particle surface from the centre of mass. The problem can then be split into

$$\boldsymbol{w} = \boldsymbol{w}^{(t)} + \boldsymbol{w}^{(r)}, \tag{4.2}$$

where both the translational contribution $\boldsymbol{w}^{(t)}$ and the rotational contribution $\boldsymbol{w}^{(r)}$ independently satisfy the Stokes equation [21]. The boundary conditions are then $\boldsymbol{w}^{(t)} = \boldsymbol{v} - \boldsymbol{u}^{(\infty)}$ and $\boldsymbol{w}^{(r)} = (\boldsymbol{\omega} - \boldsymbol{\Omega}^{(\infty)}) \times \boldsymbol{r}$, and it follows that $\boldsymbol{w}$ satisfies $\boldsymbol{w} = \boldsymbol{v} -$

$\boldsymbol{u}^{(\infty)}+(\boldsymbol{\omega}-\boldsymbol{\Omega}^{(\infty)})\times\boldsymbol{r}$ on the surface. The force $\boldsymbol{F}$ and torque $\boldsymbol{T}$ on a particle can then be written as [24]

$$\begin{bmatrix}\boldsymbol{F}\\ \boldsymbol{T}\end{bmatrix}=\begin{bmatrix}\mathbb{A} & \mathbb{B}^T\\ \mathbb{B} & \mathbb{C}\end{bmatrix}\begin{bmatrix}\boldsymbol{u}^{(\infty)}-\boldsymbol{v}\\ \boldsymbol{\Omega}^{(\infty)}-\boldsymbol{\omega}\end{bmatrix}, \tag{4.3}$$

where the tensors $\mathbb{A}$, $\mathbb{B}$ and $\mathbb{C}$ depend on the geometry of the particle. The resistance tensor $\mathbb{A}$ is a symmetric tensor and is responsible for the drag and lift force acting on the particle [23, 24]. Analogously, the tensor $\mathbb{C}$ is the resistance to rotational motion of the particle. The tensor $\mathbb{B}$ is called the translation-rotation coupling and is seen in Eq. (4.3) to relate the translational velocity to a torque, which causes the particle to rotate. Similarly, the transpose $\mathbb{B}^T$ relates a rotation $\boldsymbol{\omega}$ to a force that propels the particle. A classic example of an object which converts rotational motion to translation is a boat propeller; however, it should be noted that a boat propeller is both too large and works at too high speeds for the Stokes approximation to hold.

For particles in a shear flow, the boundary condition includes the shear $\mathbb{S}^{(\infty)}$, similarly to the vorticity of the flow

$$\boldsymbol{w}=\boldsymbol{v}-\boldsymbol{u}^{(\infty)}+(\boldsymbol{\omega}-\boldsymbol{\Omega}^{(\infty)})\times\boldsymbol{r}-\mathbb{S}^{(\infty)}\cdot\boldsymbol{r}, \tag{4.4}$$

on the surface of the particle. Analogously, the flow can be split into parts that can be solved separately and then added together [22]. The force and torque are then related by [24, 57]

$$\begin{bmatrix}\boldsymbol{F}\\ \boldsymbol{T}\end{bmatrix}=\begin{bmatrix}\mathbb{A} & \mathbb{B}^T & \mathbb{G}\\ \mathbb{B} & \mathbb{C} & \mathbb{H}\end{bmatrix}\begin{bmatrix}\boldsymbol{u}^{(\infty)}-\boldsymbol{v}\\ \boldsymbol{\Omega}^{(\infty)}-\boldsymbol{\omega}\\ \mathbb{S}^{(\infty)}\end{bmatrix}. \tag{4.5}$$

Here $\mathbb{G}$ is a third-order tensor and $\mathbb{H}$ a third-order pseudotensor under orthogonal transformations. This means that they are doubly contracted to the undisturbed strain $\mathbb{S}^{(\infty)}$, e.g. $\mathbb{G}:\mathbb{S}^{(\infty)}=\sum_i[\sum_{jk}G_{ijk}S^{(\infty)}_{jk}]\boldsymbol{e}_i$, as the strain tensor is a rank two tensor.

4.2 Inertial forces and torques on a particle

When particles are in a flow, where the particle Reynolds number is non-zero, fluid inertial effects have to be considered. In general, this can be accounted for by solving the Navier-Stokes equations (2.5), where the left-hand side is now non-zero. If the inertial effects are small, the equation can be treated using a matched asymptotic expansion in the Reynolds number. For a non-zero particle Reynolds number, there are regions in space where different terms in Eq. (2.5) dominate. The solution is constructed by solving the equations in different regions and matching them [65, 66]. There are two regions that are being matched, one close to the surface of the

particle and one far away.

Using the conventions from Section 4.1, the particle Reynolds number limits the slip velocity, on which inertial effects depend. Therefore, the simplification to consider a particle moving in a quiescent fluid is justified. A quiescent fluid fulfils $\boldsymbol{U}^{(\infty)} = 0$, $\frac{\partial}{\partial t}\boldsymbol{U}^{(\infty)} = 0$ and $\boldsymbol{\Omega}^{(\infty)} = 0 = \mathbb{S}^{(\infty)}$. The disturbance flow $\boldsymbol{w}$ for a particle settling stably with velocity $\boldsymbol{v}$ satisfies

$$\mathrm{Re}_p\,[(\boldsymbol{w}\cdot\nabla)\boldsymbol{w} - (\boldsymbol{v}\cdot\nabla)\boldsymbol{w}] = \Delta\boldsymbol{w} - \nabla p, \tag{4.6}$$

where p is the disturbance pressure. In the case of steady state settling, the term $\frac{\partial}{\partial t}\boldsymbol{w}$ vanishes. For the region close to the particle, the solution is assumed to be of the form $\boldsymbol{w} = \boldsymbol{w}^{(0)} + \mathrm{Re}_p\,\boldsymbol{w}^{(1)} + \ldots$ together with $p = p^{(0)} + \mathrm{Re}_p\,p^{(1)} + \ldots$; when inserted into Eq. (4.6) this generates a series of equations, one at each order of expansion. These can be solved separately seen as

$$\begin{aligned} \mathrm{Re}_p^{\,0}: &\quad \Delta\boldsymbol{w}^{(0)} - \nabla p^{(0)} = 0, \\ \mathrm{Re}_p^{\,1}: &\quad \Delta\boldsymbol{w}^{(1)} - \nabla p^{(1)} = (\boldsymbol{w}^{(0)}\cdot\nabla)\boldsymbol{w}^{(0)} - (\boldsymbol{v}\cdot\nabla)\boldsymbol{w}^{(0)}, \\ &\quad\vdots \end{aligned} \tag{4.7}$$

At lowest order in Re_p, we have a Stokes equation for $\boldsymbol{w}^{(0)}$ and $p^{(0)}$. The next order problem, proportional to $\mathrm{Re}_p^{\,1}$, is an inhomogeneous Stokes problem for $\boldsymbol{w}^{(1)}$ and $p^{(1)}$, where $\boldsymbol{w}^{(0)}$ enters on the right-hand side as an effective forcing. The boundary condition in the inner region is given by

$$\begin{aligned} \boldsymbol{w}^{(0)} &= \boldsymbol{v}, \\ \boldsymbol{w}^{(1)} &= 0, \\ &\vdots \end{aligned} \tag{4.8}$$

on the surface of the particle, which in turn depends on the shape of the particle and the particle-shape symmetries. This scheme can be continued for higher order corrections of inertial effects.

Far from the particle, its effects may be treated as a point force [30, 38, 67, 68]. The outer equation takes the form

$$-\mathrm{Re}_p(\boldsymbol{v}\cdot\nabla)\boldsymbol{w}_{\mathrm{out}} = \Delta\boldsymbol{w}_{\mathrm{out}} - \nabla p_{\mathrm{out}} + \boldsymbol{f}\,\delta(\boldsymbol{r}) \tag{4.9}$$

where the non-linear convective term has been disregarded as it decays too fast in space [38, 68]. Equation (4.9) is a linear differential equation and can be solved by

Fourier transformation. The solution is then required to satisfy the outer boundary condition, $\boldsymbol{w} \to 0$ when $|\boldsymbol{r}| \to \infty$. The inner solution, the one close to the surface of the particle, and the outer solution are then matched so that the undetermined coefficients in each solution are found from the other [65].

Symmetric particles that lack a rotation-translational coupling in the Stokes limit are prime examples of how fluid inertia provides a translation-rotation coupling. Examples of such particles which has been studied include: homogeneous rods [69–71], plates [54, 72] and spheroids [58, 73]; when they settle in a stationary fluid, the particles settle with a preferred orientation based on their geometrical shape. The settling orientation of a particle with a non-zero Stokes translation-rotation coupling is determined by a balance between the translation-rotation coupling and the inertial correction to the torque. Roy et al. [56] showed that for their type P1 particles, that is, partially hollow rods, a stable settling direction resulted from the translation-rotation coupling in the Stokes limit competing with the inertial correction to the torque. Candelier and Mehlig [55] concluded that the same was true for an asymmetric dumbbell and Maches et al. [61] did the same for two rigidly connected spheres. This was further shown to be the case in Paper [II], where the torque due to the translation-rotation coupling and the inertial torque competed and resulted in a stable oblique orientation.

When fluid inertia is not disregarded, the forces and torques are, in general, no longer linear functions of the fluid velocity. The general expressions for the forces and torques are still functions of the fluid velocity, but the question of how particle-shape symmetries constrain them is more complicated. Brenner and Cox [25] showed that the force and torque are third-order polynomials in the settling velocity, later extended to include the angular velocity [26]. In Paper [III] the calculation was extended to include unsteadiness. The correction to the inertial force proportional to Re_p on a steady settling particle can be split into a singular and a regular solution to yield the linear $\boldsymbol{F}^{(1)} = \boldsymbol{F}_{\mathrm{Sing}} + \boldsymbol{F}_{\mathrm{Reg}}$, where

$$\begin{aligned} \boldsymbol{F}_{\mathrm{Sing}} &= -\frac{3\nu}{32\pi}\mathbb{A}\cdot[\mathbb{A}\cdot\boldsymbol{v} - \frac{1}{3}(\hat{\boldsymbol{v}}\otimes\hat{\boldsymbol{v}})\cdot\mathbb{A}\cdot\boldsymbol{v}], \\ \boldsymbol{F}_{\mathrm{Reg}} &= \mathbb{M}:(\boldsymbol{v}\otimes\boldsymbol{v}), \end{aligned} \tag{4.10}$$

with $\hat{\boldsymbol{v}} = \boldsymbol{v}/v$ being the direction of the velocity. Similarly, one finds the inertial torque to be $\boldsymbol{T}^{(1)} = \boldsymbol{T}_{\mathrm{Sing}} + \boldsymbol{T}_{\mathrm{Reg}}$ with

$$\begin{aligned} \boldsymbol{T}_{\mathrm{Sing}} &= -\frac{3\nu}{32\pi}\mathbb{B}\cdot[\mathbb{A}\cdot\boldsymbol{v} - \frac{1}{3}(\hat{\boldsymbol{v}}\otimes\hat{\boldsymbol{v}})\cdot\mathbb{A}\cdot\boldsymbol{v}], \\ \boldsymbol{T}_{\mathrm{Reg}} &= \mathbb{N}:(\boldsymbol{v}\otimes\boldsymbol{v}), \end{aligned} \tag{4.11}$$

where $\mathbb{M}$ and $\mathbb{N}$ are third-order tensors and pseudotensors under orthogonal transformations, respectively. The names "singular" and "regular" refers to their origin

in the matching, see Paper [III] for details. It should be noted that the resistance tensors from the Stokes limit appear in the singular contribution, as a result of the Stokes flow entering as a forcing term in the first order problem in Eq. (4.7).

4.3 Symmetry considerations

It is expected that a solution of a symmetrical problem should have similar symmetries as the problem. In the Stokes limit, the particle-shape symmetries are encapsulated in the resistance tensors $\mathbb{A}, \mathbb{B}$ and $\mathbb{C}$. Therefore, the particle symmetries should constrain the elements of these tensors so as to give the force and torque the correct symmetries. Happel and Brenner [23] considered how the resistance tensors were constrained under orthogonal transformations, using the energy-dissipation scalar to derive a condition for the transformation properties of $\mathbb{A}, \mathbb{B}$ and $\mathbb{C}$. Similar results can be found by requiring that $\boldsymbol{F}' = \mathbb{O} \cdot \boldsymbol{F}$ and $\boldsymbol{T}' = \mathrm{Det}(\mathbb{O})\, \mathbb{O} \cdot \boldsymbol{T}$, by changing $\boldsymbol{v}' = \mathbb{O} \cdot \boldsymbol{v}$ and $\boldsymbol{\omega}' = \mathrm{Det}(\mathbb{O})\, \mathbb{O} \cdot \boldsymbol{\omega}$, for some orthogonal transformation that leads to the same configuration. For example, the force should be unchanged for a spheroid when rotated about its symmetry axis. It should be noted that $\boldsymbol{\omega}$ has an extra factor of the determinant since it is an axial vector. This leads to the following relation for the tensors

$$\begin{aligned} \mathbb{A} &= \mathbb{O}^{-1} \cdot \mathbb{A} \cdot \mathbb{O}, \\ \mathbb{B} &= \mathrm{Det}(\mathbb{O})\, \mathbb{O}^{-1} \cdot \mathbb{B} \cdot \mathbb{O}, \\ \mathbb{C} &= \mathbb{O}^{-1} \cdot \mathbb{C} \cdot \mathbb{O}. \end{aligned} \tag{4.12}$$

Bretherton [53] carried out a similar analysis for the case with shear included for reflections. Fries, Einarsson, and Mehlig [54] used the same method to constrain the torque on a hexagonal plate-like particle.

A similar argument, as was given for the Stokes force and torque, can be imposed on $\boldsymbol{F}_{\mathrm{Reg}}$ and $\boldsymbol{T}_{\mathrm{Reg}}$. The singular contributions are given by the Stokes resistance tensors, and thus are constrained by Eq. (4.12). The regular contributions to the force and torque are polynomial in the settling velocity and are thus written as $\boldsymbol{F}_{\mathrm{Reg}}(\boldsymbol{v})$ and $\boldsymbol{T}_{\mathrm{Reg}}(\boldsymbol{v})$. Under a symmetry transformation $\boldsymbol{v}' = \mathbb{O} \cdot \boldsymbol{v}$, the force and torque are related by

$$\boldsymbol{F}'_{\mathrm{Reg}}(\boldsymbol{v}') = \mathbb{O} \cdot \boldsymbol{F}_{\mathrm{Reg}}(\boldsymbol{v}), \tag{4.13a}$$

$$\boldsymbol{T}'_{\mathrm{Reg}}(\boldsymbol{v}') = \mathrm{Det}(\mathbb{O})\mathbb{O} \cdot \boldsymbol{T}_{\mathrm{Reg}}(\boldsymbol{v}). \tag{4.13b}$$

The force and torque can be computed for the settling velocity $\boldsymbol{v}'$ as

$$F'^{i}_{\mathrm{Reg}}(\boldsymbol{v}') = M_{ijk} O_{jl}\, O_{km}\, v^{l} v^{m}, \tag{4.14a}$$

$$T'^{i}_{\mathrm{Reg}}(\boldsymbol{v}') = M_{ijk} O_{jl}\, O_{km}\, v^{l} v^{m}, \tag{4.14b}$$

leading to the constraints

$$\begin{aligned} M_{ijk} &= O_{mi}\, M_{mnl}\, O_{nj}\, O_{lk}\,, \\ N_{ijk} &= \mathrm{Det}(\mathbb{O})\, O_{mi}\, N_{mnl}\, O_{nj}\, O_{lk}\,. \end{aligned} \tag{4.15}$$

In general, similar arguments can be made for the force and torque comprising of general functions of the settling velocity $\boldsymbol{F}(\boldsymbol{v}) = \mathbb{M}(\boldsymbol{v}) \cdot \boldsymbol{v}$ and $\boldsymbol{T}(\boldsymbol{v}) = \mathbb{N}(\boldsymbol{v}) \cdot \boldsymbol{v}$.

4.4 Examples

In this section, we consider three examples: a spheroid, cube and curved fibre. The settling of a curved fibre is the topic of Paper [II] and Chapter 5. The spheroid and cube were also considered in Paper [III]. The particles considered here are shown in Figure 4.1.

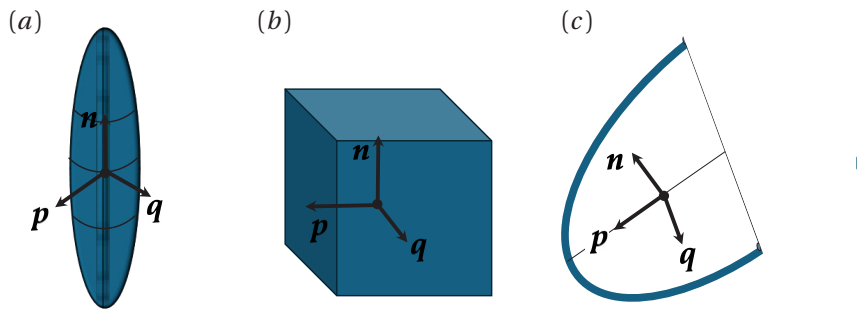

Figure 4.1: The displays the particles that is considered throughout this section, with their respective particle fixed coordinate system $\boldsymbol{p}, \boldsymbol{q}, \boldsymbol{n}$. The spheroid is being depicted in (a). The second particle shape considered is the cube shown in (b). Finally the bent fibre is depicted in (c).

The first example we will consider is the spheroid, depicted in Fig. 4.1 (a), which has a continuous rotational symmetry, about the symmetry axis $\hat{\boldsymbol{n}}$, as well as reflection

symmetries in all three directions. The reflection about the $\hat{\boldsymbol{n}}$ direction is given by

$$\mathbb{O} = \begin{pmatrix} 1 & 0 & 0 \\ 0 & 1 & 0 \\ 0 & 0 & -1 \end{pmatrix}. \tag{4.16}$$

Using the symmetry constraint for the Stokes contribution (4.12), this leads to

$$\mathbb{A} = \begin{pmatrix} A_{pp} & 0 & 0 \\ 0 & A_{qq} & A_{qn} \\ 0 & A_{nq} & A_{nn} \end{pmatrix}, \quad \mathbb{B} = \begin{pmatrix} 0 & 0 & B_{pn} \\ 0 & 0 & B_{qn} \\ B_{np} & B_{nq} & 0 \end{pmatrix}, \quad \mathbb{C} = \begin{pmatrix} C_{pp} & 0 & 0 \\ 0 & C_{qq} & C_{qn} \\ 0 & C_{nq} & C_{nn} \end{pmatrix}. \tag{4.17}$$

The reflection symmetry forces 13 coefficients to vanish, but does not impose any relationship between the coefficients. Furthermore, the particle has a continuous rotation symmetry around the $\hat{\boldsymbol{n}}$ axis, which is given by

$$\mathbb{O} = \begin{pmatrix} \cos\theta & -\sin\theta & 0 \\ \sin\theta & \cos\theta & 0 \\ 0 & 0 & 1 \end{pmatrix}, \tag{4.18}$$

for an arbitrary angle θ. Because the particle is rotationally symmetrical, the relationship must hold for all angles θ. The rotational symmetry constrains $\mathbb{A}$, $\mathbb{B}$ and $\mathbb{C}$ to take the form

$$\mathbb{A} = \begin{pmatrix} A & A^* & 0 \\ -A^* & A & 0 \\ 0 & 0 & A_{nn} \end{pmatrix}, \quad \mathbb{B} = \begin{pmatrix} B & B^* & 0 \\ -B^* & B & 0 \\ 0 & 0 & B_{nn} \end{pmatrix}, \quad \mathbb{C} = \begin{pmatrix} C & C^* & 0 \\ -C^* & C & 0 \\ 0 & 0 & C_{nn} \end{pmatrix}, \tag{4.19}$$

where A, A^*, B, B^*, C and C^* have been introduced, with coefficients shared within the tensors. For any orthogonal rotation $\mathrm{Det}(\mathbb{O}) = 1$, which leads to $\mathbb{A}, \mathbb{B}$, and $\mathbb{C}$ have the same form.

A spheroid has both particle-shape symmetries, which implies that the tensors $\mathbb{A}, \mathbb{B}$ and $\mathbb{C}$ satisfy both of these constraints. The final resistance matrices are found to be:

$$\mathbb{A} = \begin{pmatrix} A_\perp & 0 & 0 \\ 0 & A_\perp & 0 \\ 0 & 0 & A_\parallel \end{pmatrix}, \quad \mathbb{B} = \begin{pmatrix} 0 & 0 & 0 \\ 0 & 0 & 0 \\ 0 & 0 & 0 \end{pmatrix}, \quad \mathbb{C} = \begin{pmatrix} C_\perp & 0 & 0 \\ 0 & C_\perp & 0 \\ 0 & 0 & C_\parallel \end{pmatrix}. \tag{4.20}$$

The particle has two more reflection symmetries, but these do not further constrain the tensors. The matrices found through this method agree with the results found by Brenner [74] by computing the Stokes solution around a spheroid.

Computing the regular contribution to the inertial correction using Eq. (4.15) for the reflections and the rotation around $\hat{\boldsymbol{n}}$, one finds that $\mathbb{M}=0$ and $\mathbb{N}$ reduces to

$$N_{p;;}=\begin{pmatrix}0&0&0\\0&0&N_1\\0&N_2&0\end{pmatrix},\quad N_{q;;}=\begin{pmatrix}0&0&-N_1\\0&0&0\\-N_2&0&0\end{pmatrix},\quad N_{p;;}=\begin{pmatrix}0&N_3&0\\-N_3&0&0\\0&0&0\end{pmatrix}. \tag{4.21}$$

Eq. (4.21) shows that there are three degrees of freedom for the inertial contribution to the torque, N_1, N_2, and N_3. Collecting these results, the force is given by

$$F_\alpha = A_\perp\left(1-\frac{\mathrm{Re}_p\,\nu}{16\pi}A_\perp+\frac{\mathrm{Re}_p\,\nu}{32\pi}(A_\parallel-A_\perp)\hat{v}_n^2\right)v_\alpha,\quad \alpha=p,q, \tag{4.22a}$$

$$F_n = A_\parallel\left(1-\frac{\mathrm{Re}_p\,\nu}{32\pi}(3A_\parallel-A_\perp)+\frac{\mathrm{Re}_p\,\nu}{32\pi}(A_\parallel-A_\perp)\hat{v}_n^2\right)v_n. \tag{4.22b}$$

The translation-rotation coupling from the Stokes limit is found to be $\mathbb{B}=0$, which implies that $\boldsymbol{T}_{\mathrm{Reg}}$ is the only torque up to the first order correction in Re_p. The torque resulting from Eq. (4.21) can be written as

$$\boldsymbol{T}=\mathrm{Re}_p\,v^2(N_1+N_2)(\hat{v}\cdot\hat{\boldsymbol{n}})(\hat{\boldsymbol{n}}\times\hat{v}), \tag{4.23}$$

which shows that settling spheroids align because of fluid inertia. The coefficient N_1+N_2 depends on the aspect ratio [58, 73].

The second example is the cube, shown in Fig. 4.1 (b). The cube has three reflection symmetries along the three mutually perpendicular axes, and also three rotational degrees of freedom about the same mutually perpendicular axes. The three reflections are represented by

$$\mathbb{O}_1=\begin{pmatrix}-1&0&0\\0&1&0\\0&0&1\end{pmatrix},\quad \mathbb{O}_2=\begin{pmatrix}1&0&0\\0&-1&0\\0&0&1\end{pmatrix},\quad \mathbb{O}_3=\begin{pmatrix}1&0&0\\0&1&0\\0&0&-1\end{pmatrix}. \tag{4.24}$$

The effect of $\mathbb{O}_3$ has already been determined for the spheroid, and similarly the effects of $\mathbb{O}_1$ and $\mathbb{O}_2$ could be determined. We find the requirement that

$$\mathbb{A}=\begin{pmatrix}A_{pp}&0&0\\0&A_{qq}&0\\0&0&A_{nn}\end{pmatrix},\quad \mathbb{B}=\begin{pmatrix}0&0&0\\0&0&0\\0&0&0\end{pmatrix},\quad \mathbb{C}=\begin{pmatrix}C_{pp}&0&0\\0&C_{qq}&0\\0&0&C_{nn}\end{pmatrix}. \tag{4.25}$$

Any particle which has three mutually perpendicular reflection symmetries has the resistance tensors above, for example ellipsoidal particles. The cube also possesses

discrete rotational symmetry by $\pi/2$ radian increments. A $\pi/2$ rotation about the $\hat{\boldsymbol{n}}$ axis is imposed by the transformation

$$\mathbb{O}_4 = \begin{pmatrix} 0 & -1 & 0 \\ 1 & 0 & 0 \\ 0 & 0 & 1 \end{pmatrix}. \tag{4.26}$$

This results in the same condition as was found from Eq. (4.19), illustrating that the angular dependence does not enter into the constraint, just the generators. Because the cube possesses similar rotation symmetries about the $\hat{\boldsymbol{p}}$ and $\hat{\boldsymbol{q}}$ axes, the resistance matrices become

$$\mathbb{A} = \begin{pmatrix} A & 0 & 0 \\ 0 & A & 0 \\ 0 & 0 & A \end{pmatrix}, \quad \mathbb{B} = \begin{pmatrix} 0 & 0 & 0 \\ 0 & 0 & 0 \\ 0 & 0 & 0 \end{pmatrix}, \quad \mathbb{C} = \begin{pmatrix} C & 0 & 0 \\ 0 & C & 0 \\ 0 & 0 & C \end{pmatrix}. \tag{4.27}$$

This shows that $\mathbb{A} = A\mathbb{I}$ and $\mathbb{C} = C\mathbb{I}$, i.e. that the resistance tensors are isotropic.

The regular contributions to the inertial correction to the force and torque are again found using Eq. (4.15) with $\mathbb{O}_k$, for $k = 1, ..., 6$. The transformations $\mathbb{O}_5$ and $\mathbb{O}_6$ are the equivalent of $\mathbb{O}_4$ for the rotation around the $\hat{\boldsymbol{p}}$ and $\hat{\boldsymbol{q}}$ directions, respectively. Like the spheroid, $\mathbb{M} = 0$ and the inertial correction to the force is fully determined by the Stokes tensors. The pseudotensor $\mathbb{N}$ is proportional to the fully anti-symmetric tensor ϵ. This implies that the regular contribution to the inertial correction of the torque $\boldsymbol{T}_{\text{Reg}} = \mathbb{N} : (\boldsymbol{v} \otimes \boldsymbol{v}) = 0$. The force on the cube is given by

$$\boldsymbol{F} = \left(A + \frac{\text{Re}_p \nu}{16\pi} A^2 \right) \boldsymbol{v}, \tag{4.28}$$

while there is no torque on the non-rotating cube. This suggests that the cube is isotropic to linear order in Re_p, and will behave similarly to a settling sphere.

The final example, shown in Fig. 4.1 (c), is a curved fibre. The curved fibre only possess two reflection symmetries encoded by

$$\mathbb{O}_1 = \begin{pmatrix} 1 & 0 & 0 \\ 0 & -1 & 0 \\ 0 & 0 & 1 \end{pmatrix}, \quad \text{and} \quad \mathbb{O}_2 = \begin{pmatrix} 1 & 0 & 0 \\ 0 & 1 & 0 \\ 0 & 0 & -1 \end{pmatrix}, \tag{4.29}$$

which correspond to a reflection of the $\hat{\boldsymbol{q}}$ axis and the $\hat{\boldsymbol{n}}$ axis, respectively. Using the symmetry condition for the tensors $\mathbb{A}$, $\mathbb{B}$ and $\mathbb{C}$ given in Eq. (4.12) with $\mathbb{O}_1$ and $\mathbb{O}_2$

results in

$$\mathbb{A}=\begin{pmatrix} A_{pp} & 0 & 0 \\ 0 & A_{qq} & 0 \\ 0 & 0 & A_{nn} \end{pmatrix}, \quad \mathbb{B}=\begin{pmatrix} 0 & 0 & 0 \\ 0 & 0 & B_{qn} \\ 0 & B_{nq} & 0 \end{pmatrix} \quad \text{and} \quad \mathbb{C}=\begin{pmatrix} C_{pp} & 0 & 0 \\ 0 & C_{qq} & 0 \\ 0 & 0 & C_{nn} \end{pmatrix}. \tag{4.30}$$

The regular contribution to the force and torque is then determined by Eq. (4.15) using $\mathbb{O}_1$ and $\mathbb{O}_2$ and results in

$$\mathbb{M}_{p::}=\begin{pmatrix} 0 & 0 & M_{ppn} \\ 0 & 0 & 0 \\ M_{pnp} & 0 & 0 \end{pmatrix}, \mathbb{M}_{q::}=\begin{pmatrix} 0 & 0 & 0 \\ 0 & 0 & M_{qqn} \\ 0 & M_{qnq} & 0 \end{pmatrix}, \mathbb{M}_{n::}=\begin{pmatrix} M_{npp} & 0 & 0 \\ 0 & M_{nqq} & 0 \\ 0 & 0 & M_{nnn} \end{pmatrix},$$
$$\mathbb{N}_{p::}=\begin{pmatrix} 0 & 0 & 0 \\ 0 & 0 & N_{pqn} \\ 0 & N_{pnq} & 0 \end{pmatrix}, \quad \mathbb{N}_{q::}=\begin{pmatrix} 0 & 0 & N_{qpn} \\ 0 & 0 & 0 \\ N_{qnp} & 0 & 0 \end{pmatrix}, \quad \mathbb{N}_{n::}=\begin{pmatrix} 0 & N_{npq} & 0 \\ N_{nqp} & 0 & 0 \\ 0 & 0 & 0 \end{pmatrix}. \tag{4.31}$$

The regular contribution to the torque has six independent parameters, which results in the torque of the form

$$T^p_{\text{Reg}} = v^2(N_{pqn}+N_{pnq})\hat{v}_q\hat{v}_n, \tag{4.32a}$$
$$T^q_{\text{Reg}} = v^2(N_{qpn}+N_{qnp})\hat{v}_p\hat{v}_n, \tag{4.32b}$$
$$T^n_{\text{Reg}} = v^2(N_{npq}+N_{nqp})\hat{v}_p\hat{v}_q, \tag{4.32c}$$

that has three coefficients, which are sums of the six parameters. The singular contribution is given by

$$T^p_{\text{Sing}} = 0, \tag{4.33a}$$
$$T^q_{\text{Sing}} = -\tfrac{v}{32\pi}B_{qn}(3A_{nn}-A_{pp}\hat{v}_p^2-A_{qq}\hat{v}_q^2-A_{nn}\hat{v}_n^2)v_n, \tag{4.33b}$$
$$T^n_{\text{Sing}} = -\tfrac{v}{32\pi}B_{nq}(3A_{qq}-A_{pp}\hat{v}_p^2-A_{qq}\hat{v}_q^2-A_{nn}\hat{v}_n^2)v_q. \tag{4.33c}$$

4.5 Perturbation theory - addition of symmetries

Previous sections in this chapter have dealt with what particle-shape symmetries constrain. A similar question is: what happens when a particle-shape symmetry is slightly broken? The particle can have multiple effects that break the symmetry of the unperturbed shape. Small imperfections can be described by perturbing, around the original shape. As an example, consider a body whose surface is parametrised by

$$\boldsymbol{r} = R(x,y,z)\boldsymbol{e}_r = [R_0(x,y,z)+\varepsilon_1 f^{(1)}(x,y,z)+\varepsilon_2 f^{(2)}(x,y,z)]\boldsymbol{e}_r, \tag{4.34}$$

where there are two effects that perturb the surface. The sizes of the perturbations are characterised by ε_1 and ε_2. The perturbation scheme used for a single parameter can be extended to include multiple parameters. In Section 4.2, the problem was divided into a series of problems at different orders of Re_p, which is also the method employed here. The solution is therefore taken to be of the form $\boldsymbol{w} = \boldsymbol{w}^{(0)} + \mathrm{Re}_p\, \boldsymbol{w}^{(1)} + \ldots$. The surface boundary condition can be imposed by expanding the disturbance flow around the unperturbed surface through

$$\begin{aligned}\boldsymbol{w}^{(i)}\Big|_{r=R} &= \boldsymbol{w}^{(i)}\Big|_{R_0} + \varepsilon_1 (f^{(1)}\boldsymbol{e}_r)\cdot\nabla\boldsymbol{w}^{(i)}\Big|_{R_0} + \varepsilon_2 (f^{(2)}\boldsymbol{e}_r)\cdot\nabla\boldsymbol{w}^{(i)}\Big|_{R_0} \\ &+ \left[\varepsilon_1^2\frac{1}{2}(f^{(1)})^2 + \varepsilon_1\varepsilon_2 (f^{(1)})(f^{(2)}) + \varepsilon_2^2\frac{1}{2}(f^{(2)})^2\right](\boldsymbol{e}_r\otimes\boldsymbol{e}_r):(\nabla\otimes\nabla)\boldsymbol{w}^{(i)}\Big|_{R_0} + \ldots, \quad (4.35)\end{aligned}$$

where Eq. (4.35) illustrates that the expected expansion should include mixed terms, e.g. $\propto \varepsilon_1\varepsilon_2$. The ansatz for the disturbance flow and disturbance pressure is

$$\boldsymbol{w}^{(i)} = \boldsymbol{w}^{(i,0,0)} + \varepsilon_1\boldsymbol{w}^{(i,1,0)} + \varepsilon_2\boldsymbol{w}^{(i,0,1)} + \varepsilon_1^2\boldsymbol{w}^{(i,2,0)} + \varepsilon_1\varepsilon_2\boldsymbol{w}^{(i,1,1)} + \varepsilon_2^2\boldsymbol{w}^{(i,0,2)} + \ldots, \quad (4.36a)$$

$$p^{(i)} = p^{(i,0,0)} + \varepsilon_1 p^{(i,1,0)} + \varepsilon_2 p^{(i,0,1)} + \varepsilon_1^2 p^{(i,2,0)} + \varepsilon_1\varepsilon_2 p^{(i,1,1)} + \varepsilon_2^2 p^{(i,0,2)} + \ldots, \quad (4.36b)$$

which then results in the disturbance flow evaluated at the perturbed surface as a series expansion evaluated at the unperturbed surface:

$$\begin{aligned}\boldsymbol{w}^{(i)}\Big|_{r=R} &= \boldsymbol{w}^{(i,0,0)}\Big|_{R_0} + \varepsilon_1\left[\boldsymbol{w}^{(i,1,0)}\Big|_{R_0} + (f^{(1)}\boldsymbol{e}_r)\cdot\nabla\boldsymbol{w}^{(i,0,0)}\Big|_{R_0}\right] \\ &+ \varepsilon_2\left[\boldsymbol{w}^{(i,0,1)}\Big|_{R_0} + (f^{(2)}\boldsymbol{e}_r)\cdot\nabla\boldsymbol{w}^{(i,0,0)}\Big|_{R_0}\right] + \mathscr{O}(\varepsilon^2). \quad (4.37)\end{aligned}$$

From the expansion of the field around the unperturbed surface it is seen that the two perturbations to linear order in perturbations do not interact. Thus, because the mixing of the two symmetry-breaking effects occurs first at order $\varepsilon_1\varepsilon_2$ for the disturbance flow, the straining tensor separates into

$$\sigma_{lm}^{(i,j,k)} = -p^{(i,j,k)}\delta_{lm} + 2\partial_{(l}\, w_{m)}^{(i,j,k)}, \quad (4.38)$$

because of the linear dependence of the perturbed fields. Thus, for both the force and torque, the split propagates through

$$F^{(i,j,k)\,l} = \int_{r=R_0} \sigma^{(i,j,k)\,lm}\hat{n}_m \,\mathrm{d}S, \quad (4.39a)$$

$$T_l^{(i,j,k)} = \int_{r=R_0} \epsilon_{lmn} r^m \sigma^{(i,j,k)\,np}\hat{n}_p \,\mathrm{d}S, \quad (4.39b)$$

which implies that the symmetry breaking enters the force and torque as a series in the perturbations,

$$\boldsymbol{F}^{(i)} = \boldsymbol{F}^{(i,0,0)} + \varepsilon_1 \boldsymbol{F}^{(i,1,0)} + \varepsilon_2 \boldsymbol{F}^{(i,0,1)} + \mathcal{O}(\varepsilon^2), \tag{4.40a}$$

$$\boldsymbol{T}^{(i)} = \boldsymbol{T}^{(i,0,0)} + \varepsilon_1 \boldsymbol{T}^{(i,1,0)} + \varepsilon_2 \boldsymbol{T}^{(i,0,1)} + \mathcal{O}(\varepsilon^2). \tag{4.40b}$$

To first order the force and torque are sums of the two separate perturbations. From this, it is expected that the effects of symmetry breaking is additive. The additivity simplifies the symmetry analysis of objects which have more complex shapes and behaviours. An example is a spheroidal squirmer with an aspect ratio close to unity, which has both a time-dependent boundary condition as well as a small non-spheroidicity.

The perturbation theory in this section can be extended to include more symmetry breaking effects $\boldsymbol{r} = [R_0 + \sum_i \varepsilon_i f^{(i)}]\boldsymbol{e}_r$ without further problems. Likewise Eq. (4.37) may be generalised and one recovers that the lowest order in the effects of the perturbations are additive.

A natural question to ask is: what happens when there is one perturbation parameter that is much larger than the others? The labelling of ε_i is arbitrary and one can thus take ε_1 to be the largest without loss of generality, hence $1 \gg \varepsilon_1 \gg \varepsilon_2 \simeq \varepsilon_3 \ldots$. Because the parameters are smaller than unity, there exists an α such that $\varepsilon_1^\alpha \sim \varepsilon_2$. The power α is the power to which perturbation ε_1 has to be expanded before the effect of the second perturbation ε_2 starts to become visible. The effects at this order are still decoupled and the orders of ε_1 only depend on the $f^{(1)}$. The first mixing effects enter at order $\varepsilon_1\varepsilon_2 \sim \varepsilon_1^{\alpha+1}$ and the additive property can be violated.

4.6 Conclusions and outlook

The particle-shape symmetries a particle has impose constraints on the force and torque the particle experiences due to the fluid. The Stokes limit forces invariance of the resistance tensors under symmetry transformations. For small but non-zero particle Reynolds number, the inertial corrections to the force and torque are found to be polynomial in the velocities. The first-order correction was found to be a third order polynomial, with only the terms proportional to the square of the settling velocities resulting in new tensors to be constrained. The constraint is given in Eq.(4.15). It follows that particles, which do not have a translation-rotation coupling in the Stokes limit, can have a translation-rotation coupling when $\mathrm{Re}_p \neq 0$, aligning them to settle in stable directions. Breaking of particle-shape symmetries to the lowest order is seen as additive corrections, while at higher orders they can start to interact.

In experiments the particle experiences a transient in the time dynamics, which has not been rigorously studied. This provides an excellent test for the non-steady theory presented in Paper [III], which has yet to be analysed. Paper [III] considered unsteady effects (due to time-dependent variations in the surrounding flow) and as well as included particle rotation. Larger particles can be subjected to a shear flow across the particle. The theory in Paper [III] has not included such effects and remains an open project to compute the force and torque on the particle for that case. Other possible further works include extending the list of point group symmetries considered.

5 Settling dynamics of fibres

Microplastics have been linked with a negative environmental impact [75, 76], and one of the ways microplastic particles are spread is through atmospheric transport [3, 4, 76]. Models for transport of atmospheric particles [3, 5] have mainly focused on highly symmetrical particles [63, 72]. However, microplastic fibres are often asymmetric [5, 77, 78]. The shape of the particles used in atmospheric transport models has been shown to affect the transport of atmospheric particles and increase the distance that atmospheric fibres can travel [6].

Fibres are long slender bodies that can bend to form complex shapes [78, 79]. The defining feature of a slender fibre is that it has two different length scales, its length a and its width b, and the aspect ratio $\lambda = a/b \gg 1$. The fibre thus creates fluid disturbances on two length scales. When the two scales are well separated, λ being large, a matched asymptotic expansion can be used, which leads to a slender-body theory [69–71, 80]. Using this theory, the force and torque on a fibre can be calculated as a series in powers of $\log^{-1}\lambda$, provided that the radius of curvature of the fibre is much larger than the width b.

In Chapter 4 and Paper [III], it was shown that particle-shape symmetry constrains the torque in the Stokes limit and the inertial corrections. The inertial correction to the torque is given as a third-order polynomial in the relative velocity with the coefficients constrained by the symmetries. Bent fibres have fewer symmetries than a straight fibre and, as a consequence, need more parameters to describe their torque, compared with a straight fibre, when settling. In Paper [II], the parameters of the torque upon a planar curved fibre, bent into a quarter- and semicircular arc settling in a quiescent fluid, were calculated using a bead model together with the slender-body theory. In the bead model, the fibre is replaced by a collection of rigidly connected beads, where the effects of nearby beads are inferred in the boundary condition for each bead. The curved fibre is predicted to have a stable settling orientation where the normal of the plane in which the curved fibre lies forms an angle with the direction of gravity. The predicted angle is compared with experimental results for millimetre-sized fibres dropped in air, where the angle is found to qualitatively have the same dependence on the inertial parameter.

Section 5.1 covers the settling dynamics in the Stokes limit, without any fluid inertial effects. The forces and torques on straight and curved fibres are discussed. Section 5.2 introduces inertial effects for straight and curved fibres. The chapter then proceeds with Section 5.3, where the results of experiments and the theory of Paper [II] are discussed. The chapter concludes with a summary and outlook in Section 5.4.

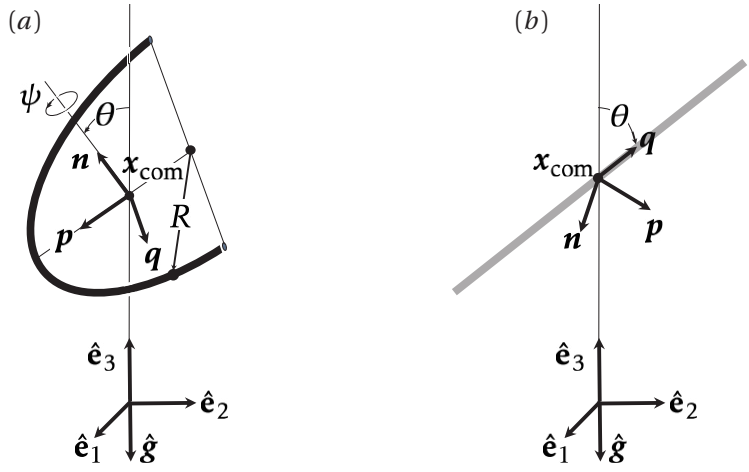

Figure 5.1: This illustration defines the coordinate system used for a curved fibre (a) and a straight fibre (b).

5.1 Stokes limit

Very short fibres with a length scale much smaller than that of the viscous length ν/v_t, where v_t is the terminal settling speed, are approximated by the Stokes limit. In Section 4.4, the curved fibre in Figure 5.1 (a) was shown to have Stokes-resistance tensors

$$\mathbb{A} = \begin{pmatrix} A_{pp} & 0 & 0 \\ 0 & A_{qq} & 0 \\ 0 & 0 & A_{nn} \end{pmatrix} \quad \text{and} \quad \mathbb{B} = \begin{pmatrix} 0 & 0 & 0 \\ 0 & 0 & B_{qn} \\ 0 & B_{nq} & 0 \end{pmatrix}, \tag{5.1}$$

due to its reflection symmetry in $\hat{\boldsymbol{q}}$ and $\hat{\boldsymbol{n}}$ and π-rotation symmetry around $\hat{\boldsymbol{p}}$. The straight fibre in Figure 5.1 (b) imposes the additional conditions of having a reflection symmetry in $\hat{\boldsymbol{p}}$ and, depending on the cross-section, an additional (discrete) rotation-symmetry around $\hat{\boldsymbol{q}}$. Assuming a circular cross-section, one finds $A_{pp} = A_{nn} = A_\perp$, $A_{qq} = A_\parallel$ and $B_{qn} = B_{nq} = 0$. In Eq. (5.1), the curved fibre has a non-zero translation-rotation coupling, which generates a torque

$$T^{(0)p} = 0, \quad T^{(0)q} = B_{qn}\, v_n, \quad T^{(0)n} = B_{nq}\, v_q, \tag{5.2}$$

on the fibre for all settling directions, except when $\boldsymbol{v}$ is co-linear with $\hat{\boldsymbol{p}}$, corresponding to $\theta = \pi/2, \psi = 0$ in Figure 5.1 (a). The curved fibre thus settles with a preferred orientation. The straight fibre does not have a translation-rotation coupling and hence keeps its original orientation while settling.

5.2 Inertial torques on slender bodies

Inertial torques are known to cause particles to settle in preferred directions [59, 72, 73, 81, 82]. To first order in $\mathrm{Re}_p = a\,v_t/\nu$, the first and third powers of $\hat{\boldsymbol{v}}$ in the torque are determined by the singular contribution, Eq. (4.11), and by extension by the Stokes resistance tensors. The quadratic terms found in Eq. (4.11) were constrained in Section 4.4 for a spheroid, with the same symmetry as the straight fibres in Fig. 5.1 (b), except with $\hat{\boldsymbol{q}}$ as the symmetry axis, resulting in

$$\mathbb{N}_{p,:,:} = \begin{pmatrix} 0 & 0 & 0 \\ 0 & 0 & N_1 \\ 0 & N_2 & 0 \end{pmatrix}, \mathbb{N}_{q,:,:} = \begin{pmatrix} 0 & 0 & N_3 \\ 0 & 0 & 0 \\ -N_3 & 0 & 0 \end{pmatrix}, \mathbb{N}_{n,:,:} = \begin{pmatrix} 0 & -N_2 & 0 \\ -N_1 & 0 & 0 \\ 0 & 0 & 0 \end{pmatrix}. \quad (5.3)$$

The quadratic contribution to the inertial correction of the torque then becomes $\boldsymbol{T}^{(1)}_{\mathrm{reg}} = (N_1 + N_2)(\hat{q}\cdot\boldsymbol{v})(\hat{q}\times\boldsymbol{v})$, which is of the same form of previous studies [58, 59, 62, 71, 83]. The translation-rotation coupling in the Stokes limit was shown to be $\mathbb{B} = 0$, and it therefore follows that

$$\boldsymbol{T} = \mathrm{Re}_p(N_1 + N_2)v^2(\hat{\boldsymbol{q}}\cdot\hat{\boldsymbol{v}})(\hat{\boldsymbol{q}}\times\hat{\boldsymbol{v}}), \quad (5.4)$$

where the coefficient $(N_1 + N_2)$ depends on the exact geometry of the fibre. From Eq. (5.4) it is clear that the preferential settling orientation of straight fibres is determined by fluid inertia. The torque vanishes whenever $\hat{\boldsymbol{q}}$ points in the settling direction, $\hat{\boldsymbol{q}}\times\boldsymbol{v} = 0$, or is orthogonal to the settling direction, $\hat{\boldsymbol{q}}\cdot\boldsymbol{v} = 0$. Depending on the sign of the coefficient $N_1 + N_2$, one of these will be a stable settling direction [73]. It has been observed that elongated particles settle with $\hat{\boldsymbol{q}}$ orthogonal to the settling direction [59, 62, 84].

The inertial correction to the torque upon a curved fibre shown in Fig. 5.1 (a) was derived in Section 4.4, for which one finds

$$T^{(1)p} = (N_{pqn} + N_{pnq})v_q v_n, \quad (5.5a)$$

$$T^{(1)q} = \nu\left\{(N_{qpn} + N_{qnp})\hat{v}_p - \tfrac{1}{32\pi}B_{qn}[3A_{nn} - (A_{pp}\hat{v}_p^2 + A_{qq}\hat{v}_q^2 + A_{nn}\hat{v}_n^2)]\right\}v_n, \quad (5.5b)$$

$$T^{(1)n} = \nu\left\{(N_{npq} + N_{nqp})\hat{v}_p - \tfrac{1}{32\pi}B_{nq}[3A_{qq} - (A_{pp}\hat{v}_p^2 + A_{qq}\hat{v}_q^2 + A_{nn}\hat{v}_n^2)]\right\}v_q. \quad (5.5c)$$

Breaking the symmetry through bending the fibre in the $\hat{\boldsymbol{p}}$ direction, the torque component along the $\hat{\boldsymbol{q}}$ axis becomes non-zero. The presence of a Stokes translation-rotation coupling and the fluid inertial contributions to the torque means that there are two effects that determine the settling direction. The steady settling orientation therefore depends on the numerical values of the coefficients.

5.3 Curved fibres settling in quiescent fluid

The settling of a curved fibre is described by Newton's second law

$$\rho_p V \dot{\boldsymbol{v}} = (\rho_p - \rho_f)\boldsymbol{g} + \boldsymbol{F}, \tag{5.6a}$$

$$\frac{\mathrm{d}}{\mathrm{d}t}(\mathbb{J}\boldsymbol{\omega}) = \boldsymbol{T}, \tag{5.6b}$$

in the lab frame. In the particle fixed coordinate system $\hat{\boldsymbol{p}}, \hat{\boldsymbol{q}}, \hat{\boldsymbol{n}}$ centred on the centre of mass, the moment of inertia $\mathbb{J}$ is constant and Eq. (5.6b) can be rewritten as [64]

$$\mathbb{J}\frac{\mathrm{d}}{\mathrm{d}t}\boldsymbol{\omega} = \boldsymbol{T} + \boldsymbol{\omega} \times (\mathbb{J} \cdot \boldsymbol{\omega}). \tag{5.7}$$

The coordinate system evolves with

$$\frac{\mathrm{d}}{\mathrm{d}t}\hat{\boldsymbol{p}} = \boldsymbol{\omega} \times \hat{\boldsymbol{p}}, \quad \frac{\mathrm{d}}{\mathrm{d}t}\hat{\boldsymbol{q}} = \boldsymbol{\omega} \times \hat{\boldsymbol{q}}, \quad \frac{\mathrm{d}}{\mathrm{d}t}\hat{\boldsymbol{n}} = \boldsymbol{\omega} \times \hat{\boldsymbol{n}}. \tag{5.8}$$

Steady rotation-free settling requires $\dot{\boldsymbol{v}} = 0$ and $\boldsymbol{\omega} = 0$. Given the Stokes torque from Eq. (4.3) and (5.1) and the inertial correction to the torque Eq. (5.5), it follows that the torque component T^p vanishes if $v_q = 0$. The T^n component of the torque also vanish as the first order inertial correction in Eq. (5.5) is proportional to v_q and the Stokes limit is $T^{(0)n} = B_{nq} v_q$. Furthermore, the torque component in the direction of $\hat{\boldsymbol{q}}$, Eq. (5.5b), vanishes if $\hat{v}_n = 0$, which means that the fibre settles with $\hat{\boldsymbol{p}}$ parallel to gravity, the settling orientation in the Stokes limit. However, the torque can also vanish if $\hat{\boldsymbol{v}}$ is orientated such that $\hat{v}_q = 0$ and

$$B_{qn}(1 - \tfrac{3\,\mathrm{Re}_p}{32\pi} A_{nn}) + 2\,\mathrm{Re}_p\, N_{q(pn)} \hat{v}_p - \tfrac{\mathrm{Re}_p}{32\pi} B_{qn}(A_{pp}\hat{v}_p^2 + A_{nn}\hat{v}_n^2) = 0, \tag{5.9}$$

where Re_p is the particle Reynolds number based on the settling velocity and $N_{q(np)} = \frac{1}{2}(N_{qpn} + N_{qnp})$ is the symmetrised tensor. Defining the tilt angle, θ, as the angle to be the angle between $\hat{\boldsymbol{n}}$ and the settling direction of the fibre, the components become $\hat{v}_n = \cos\theta$ and $\hat{v}_p = \sin\theta$. Under the assumption that

$$\frac{B_{qn}^2 (A_{pp} - A_{nn})(1 - \frac{\mathrm{Re}_p}{8\pi} A_{nn})}{32\pi\,\mathrm{Re}_p\, N_{q(pn)}^2} \ll 1, \tag{5.10}$$

the tilt angle is approximately given by

$$\sin\theta \approx \frac{B_{qn}(1 - \frac{\mathrm{Re}_p}{8\pi} A_{nn})}{2\,\mathrm{Re}_p\, N_{q(pn)}}. \tag{5.11}$$

The similarity between T^q and T^p means that an analogous result can be found if one instead assumes $\hat{v}_n = 0$, but that case is not considered here as it is unstable [II].

To determine which of the four solutions ($\theta = \pm\pi/2$, $\sin^{-1}(\frac{B_{qn}(1-\frac{\mathrm{Re}_p}{8\pi}A_{nn})}{2\,\mathrm{Re}_p\,N_{q(pn)}})$) and $\theta = \pi - \sin^{-1}(\frac{B_{qn}(1-\frac{\mathrm{Re}_p}{8\pi}A_{nn})}{2\,\mathrm{Re}_p\,N_{q(pn)}})$ is the steady solution, the coefficients must be computed. In Paper [II], this was done for a quarter- and semicircular fibre to order $1/\log^2\lambda$, using a combination of a model where the fibre is represented as a series of beads and the slender-body theory [71]. The stable direction was found to be given by

$$\hat{v}_p = \sin\theta^*, \quad \hat{v}_q = 0, \quad \hat{v}_n = \cos\theta^*, \tag{5.12}$$

where $\sin\theta^* = B_{qn}/(2\,\mathrm{Re}_p\,N_{q(pn)})$, using the notation of this thesis. It should be noted that B_{qn} is of order $1/\log^2\lambda$ compared with B_{nq} which is of order $1/\log\lambda$, this explains why Eq. (3c) in Paper [II] is the only component of the torque that has linear and cubic terms in the settling velocity when quoted to order $1/\log^2\lambda$. It also validates the condition in Eq. (5.10) since $N_{q(pn)}$ is of order $1/\log^2\lambda$, and A_{pp} as well as A_{nn} are of order $1/\log\lambda$, making the fraction of order $1/\log\lambda \ll 1$. When $\mathrm{Re}_p/\log\lambda \ll 1$, Eq. (5.11) reduces to θ^*. When the particle Reynolds number Re_p is very small, the right hand side of Eq. (5.11) becomes greater than unity, and the solution ceases to exist in a pitch-fork bifurcation point, below which $\theta^* = \pi/2$ is stable.

The experimental results presented in Paper [II] show that the particle settles at an angle to the direction of gravity. For low fluid inertia, the experimental results agree well with the theoretical prediction. For higher fluid inertia, the theoretical prediction overestimates the influence of the fluid inertial effect on the settling angle, resulting in a discrepancy between theory and experimental results. The tilted orientation compared with the Stokes prediction ($\theta = \pi/2$) and the inertial torque principle of "particles settle broadside down" ($\theta = 0$) [62] shows that the two effects compete, which results in a direction between the two effects. The drag on the fibre depends on the direction in which the fibre settles, which shows the importance of inertial effects on the fibre when applied in models for atmospherical fibres.

5.4 Conclusions and further work

By studying the settling dynamics of fibres, we have seen that the inertial torque plays a significant role in determining the stable direction, and consequently what drag the fibre experiences. In contrast to the straight fibre, the torque experienced by the curved fibre is not solely governed by the inertial torque, and the curved fibre does not settle according to the principle of "broad side down". The complex dynamics of a bent fibre shows that treating particles as spherical or spheroidal may not suffice in models for atmospheric transport of fibres.

Theoretical models for the dynamics of fibres often utilise the slender-body theory used to compute the force and torque on the fibre. The theory requires $\log\lambda \gg 1$, and is computed to order $\log^{-2}\lambda$, which is not necessarily accurate enough for all applications. A theory for slender bodies to higher order in $\log^{-1}\lambda$ could be of practical interest in studies of smaller fibres, where the aspect ratio is of order $\lambda \sim 10$. The slender-body theory neglects interactions between fibre segments. Consequently, fibres with a small radius of curvature thus fail to be accurately described by the slender-body theory. Therefore, a new theory is required to find the forces and torques on particles with high curvature.

In this chapter and Paper [II], the fibres were rigid and maintained their shape while settling. A question that might be of interest is how the rigidity of the fibre affects the settling behaviour. Is there a steady settling configuration and what is its shape? Further, it would be interesting to determine if there is a stiffness below which there no longer exists a stable fixed point for the dynamics.

6 Conclusion

Particles suspended in a fluid are of crucial importance in many scientific and engineering problems. The particles and fluid form an interacting dynamical system. For larger particles, the dynamics depend on the inertia of the fluid and the particle. Fluid inertia is measured by the dimensionless particle Reynolds number Re_p, which is proportional to the size of the particle. In the Stokes limit, $\mathrm{Re}_p \to 0$, where fluid inertia is neglected, particle inertia may still play an important role in the dynamics. Particle inertia, measured by the non-dimensional Stokes number St, allows particles to detach from the flow and avoids regions of high vorticity [2, 11]. Another consequence of particle inertia is that particles can arrive in regions in configuration space with different velocities, which means that the particle-velocity field is multivalued in those locations [8, 17]. The formation of such region occurs when the phase space of the particle dynamics folds over, which happens when the particle-velocity gradients diverge (caustics). In the persistent limit, caustics form when the particles experience fluid-velocity gradients with high strain [19]. For small St, the large fluctuations of fluid-velocity gradients that lead to caustics are rare events, and they depend on the tails of the gradient distribution. In Paper [I], a statistical model for the fluid-velocity gradients that is non-Gaussian with heavy tails was proposed. It was shown that the heavy tails enhance the caustic-formation rate compared to previously studied Gaussian models. The result indicates that the heavy tails in the distribution of fluid-velocity gradients in turbulence are important for understanding caustic formation and its consequences. The optimal fluctuation of the fluid-velocity gradients that results in caustic formation was shown to follow the same mechanism in the Gaussian and non-Gaussian model, given by the time correlation function. The main difference is the greater variance in the distribution of fluctuations which results in formation. A question which still remains is how the BBO history force affects the rate of caustic formation for heavy particles in turbulence. Do history effects enhance or suppress caustic formation?

Larger particles experience the effects of fluid inertia more strongly. As a result, the hydrodynamic force and torque exerted by the fluid on the particle gains an inertial correction to the Stokes limit, that is proportional to the particle Reynolds number. The correction is a third-order polynomial in the relative velocity of the particle and fluid, with coefficients that depend on the geometry of the particle. Symmetries in the shape of the particle constrain the coefficients. In Paper [III], constraints for the inertial correction to the force and torque were derived including time-dependent contributions. We identified which contributions are due to instantaneous effects, and which depend on the transient dynamics. Settling particles in turbulence are subjected to time-dependent flows which may reorientate the particles. Reorientation changes the drag on the particle. A question is then how does time-dependent

motion affect the long-range transport of atmospheric particles. Current models represent the particles as volume-equivalent spheres, but it has been shown that fibres are transported differently to that of a sphere [84]. In the future we will analyse the how the reduction of particle-shape symmetries affect the atmospheric transport of particles.

Atmospheric fibres are examples of particles which are large enough to experience corrections to the hydrodynamic force and torque because of fluid-inertia effects. For low particle Reynolds numbers, the torque on a straight fibres is known. Microplastic fibres are not necessarily straight, and curved fibres have fewer particle-shape symmetries than straight fibres. As mentioned previously, particles with more symmetries have torques which are more constrained. Paper [II] considered a curved planar fibre to study the settling of less symmetrical particles. The torque on the fibre is computed theoretically using a combination of the slender-body theory and a bead model (replacing the fibre with a chain of hydrodynamically interacting beads). The computed torque shows that the inertial correction to the torque causes the curved fibre to settle with a tilt angle compared to the Stokes limit. This angle was compared with results from an experiment where semi- and quarter-circular fibres were dropped in a chamber of quiescent air and their motion were recorded. The theoretically predicted tilt angle for the semicircular fibre is in qualitative agreement with the experimentally found settling angles. However, the theoretically predicted angle appears to overpredict the inertial correction. The question is how to resolve the quantitative differences between the tilt angles observed in the experiments and those predicted by our theory. It was shown in Chapter 5 that the theory used in Paper [II] misses terms because of the considered expansion order in $\log^{-1}\lambda$ (where λ is the aspect ratio) in the slender-body theory. Can the quantitative difference in the settling angle be explained by the shortcomings of the slender-body theory? The theory assumes that the disturbances generated in the near-field of a fibre segment do not interact with disturbances generated by a nearby segment. This is known to be a good assumption for fibres with infinite aspect ratio, but is likely an inaccurate approximation for fibres with aspect ratios realisable in experiments. Another possibility, is that the Stokes approximation used in the theoretical model is inaccurate, as it was calculated from a bead model.

References

[1] E. Villermaux. “Mixing Versus Stirring”. In: *Annual Review of Fluid Mechanics* 51.Volume 51, 2019 (2019), pp. 245–273. ISSN: 1545-4479. DOI: https://doi.org/10.1146/annurev-fluid-010518-040306.

[2] M. R. Maxey. “Droplets in turbulence: a: new perspective”. In: *Journal of Fluid Mechanics* 816 (2017), pp. 1–4. DOI: 10.1017/jfm.2017.96.

[3] S. Allen et al. “Evidence of free tropospheric and long-range transport of microplastic at Pic du Midi Observatory”. In: *Nature Communications* 12.1 (Dec. 2021), p. 7242. DOI: 10.1038/s41467-021-27454-7.

[4] Y. Zhang et al. “Atmospheric microplastics: A review on current status and perspectives”. In: *Earth-Science Reviews* 203 (2020), p. 103118. ISSN: 0012-8252. DOI: https://doi.org/10.1016/j.earscirev.2020.103118.

[5] J. Brahney et al. “Constraining the atmospheric limb of the plastic cycle”. In: *Proceedings of the National Academy of Sciences* 118.16 (2021), e2020719118. DOI: 10.1073/pnas.2020719118.

[6] D. Tatsii et al. “Shape Matters: Long-Range Transport of Microplastic Fibers in the Atmosphere”. In: *Environmental Science & Technology* 58.1 (Jan. 2024), pp. 671–682. DOI: 10.1021/acs.est.3c08209.

[7] P. G. Saffman and J. S. Turner. “On the collision of drops in turbulent clouds”. In: *Journal of Fluid Mechanics* 1.1 (1956), pp. 16–30. DOI: 10.1017/S0022112056000020.

[8] G. Falkovich, A. Fouxon, and M. G. Stepanov. “Acceleration of rain initiation by cloud turbulence”. In: *Nature* 419.6903 (2002), pp. 151–154. DOI: 10.1038/nature00983.

[9] B. J. Devenish et al. “Droplet growth in warm turbulent clouds”. In: *Quarterly Journal of the Royal Meteorological Society* 138.667 (2012), pp. 1401–1429. DOI: https://doi.org/10.1002/qj.1897.

[10] J. Bec, K. Gustavsson, and B. Mehlig. “Statistical Models for the Dynamics of Heavy Particles in Turbulence”. In: *Annual Review of Fluid Mechanics* 56.Volume 56, 2024 (2024), pp. 189–213. ISSN: 1545-4479. DOI: https://doi.org/10.1146/annurev-fluid-032822-014140.

[11] M. R. Maxey. “The gravitational settling of aerosol particles in homogeneous turbulence and random flow fields”. In: *Journal of Fluid Mechanics* 174 (1987), pp. 441–465. DOI: 10.1017/S0022112087000193.

[12] W. C. Reade and L. R. Collins. “Effect of preferential concentration on turbulent collision rates”. In: *Physics of Fluids* 12.10 (Oct. 2000), pp. 2530–2540. ISSN: 1070-6631. DOI: 10.1063/1.1288515.

[13] J. Bec. “Fractal clustering of inertial particles in random flows”. In: *Physics of Fluids* 15.11 (Nov. 2003), pp. L81–L84. ISSN: 1070-6631. DOI: 10.1063/1.1612500.

[14] M. Wilkinson et al. “Unmixing in random flows”. In: *Physics of Fluids* 19.11 (Nov. 2007), p. 113303. ISSN: 1070-6631. DOI: 10.1063/1.2766740.
[15] K. Gustavsson and B. Mehlig. “Statistical models for spatial patterns of heavy particles in turbulence”. In: *Advances in Physics* 65.1 (2016), pp. 1–57. DOI: 10.1080/00018732.2016.1164490.
[16] J. Meibohm et al. “Fractal catastrophes”. In: *New Journal of Physics* 22.1 (Jan. 2020), p. 013033. DOI: 10.1088/1367-2630/ab60f7.
[17] M. Wilkinson and B. Mehlig. “Caustics in turbulent aerosols”. In: *Europhysics Letters* 71.2 (June 2005), p. 186. DOI: 10.1209/epl/i2004-10532-7.
[18] J. Meibohm et al. “Paths to caustic formation in turbulent aerosols”. In: *Phys. Rev. Fluids* 6 (6 June 2021), p. L062302. DOI: 10.1103/PhysRevFluids.6.L062302.
[19] J. Meibohm, K. Gustavsson, and B. Mehlig. “Caustics in turbulent aerosols form along the Vieillefosse line at weak particle inertia”. In: *Phys. Rev. Fluids* 8 (2 Feb. 2023), p. 024305. DOI: 10.1103/PhysRevFluids.8.024305.
[20] H. Brenner. “The Stokes resistance of an arbitrary particle”. In: *Chemical Engineering Science* 18.1 (1963), pp. 1–25. ISSN: 0009-2509. DOI: https://doi.org/10.1016/0009-2509(63)80001-9.
[21] H. Brenner. “The Stokes resistance of an arbitrary particle—II: An extension”. In: *Chemical Engineering Science* 19.9 (1964), pp. 599–629. ISSN: 0009-2509. DOI: https://doi.org/10.1016/0009-2509(64)85051-X.
[22] H. Brenner. “The Stokes resistance of an arbitrary particle—III: Shear fields”. In: *Chemical Engineering Science* 19.9 (1964), pp. 631–651. ISSN: 0009-2509. DOI: https://doi.org/10.1016/0009-2509(64)85052-1.
[23] J. Happel and H. Brenner. *Low Reynolds number hydrodynamics*. Springer Netherlands, 2012. ISBN: 978-94-009-8352-6.
[24] S. Kim and J. Karrila Seppo. *Microhydrodynamics*. Butterworth-Heinemann, 1991. ISBN: 9780-7506-9173-4. DOI: https://doi.org/10.1016/C2013-0-04644-0.
[25] H. Brenner and R. G. Cox. “The resistance to a particle of arbitrary shape in translational motion at small Reynolds numbers”. In: *Journal of Fluid Mechanics* 17 (1963), pp. 561–595.
[26] R. G. Cox. “The steady motion of a particle of arbitrary shape at small Reynolds numbers”. In: *Journal of Fluid Mechanics* 23.4 (1965), pp. 625–643. DOI: 10.1017/S0022112065001593.
[27] G. Falkovich and K. R. Sreenivasan. “Lessons from hydrodynamic turbulence”. In: *Physics Today* 59.4 (Apr. 2006), pp. 43–49. ISSN: 0031-9228. DOI: 10.1063/1.2207037.
[28] U. Frisch. *Turbulence: The Legacy of A. N. Kolmogorov*. Cambridge University Press, 1995.
[29] G. K. Batchelor. *The Theory of Homogeneous Turbulence*. Cambridge University Press, 1953.

[30] T. Redaelli et al. “Hydrodynamic force on a small squirmer moving with a time-dependent velocity at small Reynolds numbers”. In: *Journal of Fluid Mechanics* 973 (2023), A11. DOI: 10.1017/jfm.2023.650.

[31] E. J. Hinch. “Hydrodynamics at Low Reynolds Numbers: A Brief and Elementary Introduction”. In: *Disorder and Mixing: Convection, Diffusion and Reaction in Random Materials and Processes*. Dordrecht: Springer Netherlands, 1988, pp. 43–56. ISBN: 978-94-009-2825-1. DOI: 10.1007/978-94-009-2825-1_4.

[32] G. B. Arfken, H. J. Weber, and F. E. Harris. *Mathematical Methods for Physicists: A Comprehensive Guide*. Academic Press, 2011.

[33] G. G. Stokes. “On the Effect of the Internal Friction of Fluids on the Motion of Pendulums”. In: *Mathematical and Physical Papers*. Cambridge University Press, 2009, pp. 1–10.

[34] R. W. Johnson. *Handbook of Fluid Dynamics*. 2nd ed. CRC Press, 2016. ISBN: 9780429106989. DOI: 10.1201/b19031.

[35] M. R. Maxey and J. J. Riley. “Equation of motion for a small rigid sphere in a nonuniform flow”. In: *The Physics of Fluids* 26.4 (Apr. 1983), pp. 883–889. ISSN: 0031-9171. DOI: 10.1063/1.864230.

[36] A. B. Basset. *A treatise on hydrodynamics, with numerous examples*. eng. Vol. 2. England: Bell and co., 1888.

[37] J. Boussinesq. *Théorie analytique de la chaleur*. Vol. 2. Gauthier-Villars, 1903.

[38] F. Candelier et al. “Second-order inertial forces and torques on a sphere in a viscous steady linear flow”. In: *Journal of Fluid Mechanics* 954 (Jan. 2023). ISSN: 1469-7645. DOI: 10.1017/jfm.2022.1015.

[39] M. Wilkinson, B. Mehlig, and V. Uski. “Stokes Trapping and Planet Formation”. In: *The Astrophysical Journal Supplement Series* 176.2 (June 2008), p. 484. DOI: 10.1086/533533.

[40] J. Bec et al. “Intermittency in the velocity distribution of heavy particles in turbulence”. In: *Journal of Fluid Mechanics* 646 (2010), pp. 527–536. DOI: 10.1017/S0022112010000029.

[41] K. Gustavsson and B. Mehlig. “Distribution of velocity gradients and rate of caustic formation in turbulent aerosols at finite Kubo numbers”. In: *Phys. Rev. E* 87 (2 Feb. 2013), p. 023016. DOI: 10.1103/PhysRevE.87.023016.

[42] S. A. Derevyanko et al. “Lagrangian and Eulerian descriptions of inertial particles in random flows”. In: *Journal of Turbulence* 8 (2007), N16. DOI: 10.1080/14685240701332475.

[43] K. Gustavsson et al. “Inertial-particle dynamics in turbulent flows: caustics, concentration fluctuations and random uncorrelated motion”. In: *New Journal of Physics* 14.11 (Nov. 2012), p. 115017. DOI: 10.1088/1367-2630/14/11/115017.

[44] J. Meibohm et al. “Caustic formation in a non-Gaussian model for turbulent aerosols”. In: *Phys. Rev. Fluids* 9 (2 Feb. 2024), p. 024302. DOI: 10.1103/PhysRevFluids.9.024302.

[45] G. E. Uhlenbeck and L. S. Ornstein. “On the Theory of the Brownian Motion”. In: *Phys. Rev.* 36 (5 Sept. 1930), pp. 823–841. DOI: 10.1103/PhysRev.36.823.

[46] H. Risken. *The Fokker-Planck equation. Methods of solution and applications. 2nd ed.* Vol. 18. Springer, Jan. 1996. ISBN: 9783642968099. DOI: 10.1007/978-3-642-96807-5.

[47] J. Mathews and R. L. Walker. *Mathematical Methods of Physics*. W.A. Benjamin, 1964.

[48] L. D. Landau and E. Lifschic. *Course of theoretical physics. vol. 1: Mechanics*. Oxford, 1978.

[49] T. Bätge, I. Fouxon, and M. Wilczek. “Quantitative Prediction of Sling Events in Turbulence at High Reynolds Numbers”. In: *Phys. Rev. Lett.* 131 (5 Aug. 2023), p. 054001. DOI: 10.1103/PhysRevLett.131.054001.

[50] C. Rajarshi and R. Govindarajan. *Caustics of finitely dense inertial particles*. 2026.

[51] A. Daitche. “On the role of the history force for inertial particles in turbulence”. In: *Journal of Fluid Mechanics* 782 (2015), pp. 567–593. DOI: 10.1017/jfm.2015.551.

[52] S. Olivieri et al. “The effect of the Basset history force on particle clustering in homogeneous and isotropic turbulence”. In: *Physics of Fluids* 26.4 (Apr. 2014), p. 041704. ISSN: 1070-6631. DOI: 10.1063/1.4871480.

[53] F. P. Bretherton. “The motion of rigid particles in a shear flow at low Reynolds number”. In: *Journal of Fluid Mechanics* 14.2 (1962), pp. 284–304. DOI: 10.1017/S002211206200124X.

[54] J. Fries, J. Einarsson, and B. Mehlig. “Angular dynamics of small crystals in viscous flow”. In: *Phys. Rev. Fluids* 2 (1 Jan. 2017), p. 014302. DOI: 10.1103/PhysRevFluids.2.014302.

[55] F. Candelier and B. Mehlig. “Settling of an asymmetric dumbbell in a quiescent fluid”. In: *Journal of Fluid Mechanics* 802 (Aug. 2016), pp. 174–185. ISSN: 1469-7645. DOI: 10.1017/jfm.2016.350.

[56] A. Roy et al. “Inertial torques and a symmetry breaking orientational transition in the sedimentation of slender fibres”. In: *Journal of Fluid Mechanics* 875 (2019), pp. 576–596. DOI: 10.1017/jfm.2019.492.

[57] D. Collins et al. “Lord Kelvin’s isotropic helicoid”. In: *Physical Review Fluids* 6.7 (July 2021). ISSN: 2469-990X. DOI: 10.1103/physrevfluids.6.074302.

[58] F. Jiang et al. “Inertial torque on a small spheroid in a stationary uniform flow”. In: *Phys. Rev. Fluids* 6 (2 Feb. 2021), p. 024302. DOI: 10.1103/PhysRevFluids.6.024302.

[59] F. Cabrera-Booman et al. “Experimental validation of fluid inertia models for a cylinder settling in a quiescent flow”. In: *Physical Review Fluids* 7.2 (Feb. 2022). ISSN: 2469-990X. DOI: 10.1103/physrevfluids.7.024301.

[60] T. Miara et al. “Dynamics of inertialess sedimentation of a rigid U-shaped disk”. In: *Communications Physics* 7.1 (Feb. 2024), p. 47. DOI: 10.1038/s42005-024-01537-5.
[61] Z. Maches et al. “Settling of two rigidly connected spheres”. In: *Journal of Fluid Mechanics* 995 (2024), A15. DOI: 10.1017/jfm.2024.711.
[62] T. Bhowmick et al. “Inertia Induces Strong Orientation Fluctuations of Non-spherical Atmospheric Particles”. In: *Phys. Rev. Lett.* 132 (3 Jan. 2024), p. 034101. DOI: 10.1103/PhysRevLett.132.034101.
[63] S. Xiao et al. “Long-distance atmospheric transport of microplastic fibres influenced by their shapes”. In: *Nature Geoscience* 16.10 (Oct. 2023), pp. 863–870. DOI: 10.1038/s41561-023-01264-6.
[64] R. Ouchene. “Numerical simulation and modeling of the hydrodynamic forces and torque acting on individual oblate spheroids”. In: *Physics of Fluids* 32.7 (July 2020), p. 073303. ISSN: 1070-6631. DOI: 10.1063/5.0011618.
[65] E. J. Hinch. *Perturbation Methods*. Cambridge University Press, 1991.
[66] M. Van Dyke. *Perturbation Methods in Fluid Mechanics*. The Parabolic press, 1975. ISBN: 0-915760-01-0.
[67] S. Childress. “The slow motion of a sphere in a rotating, viscous fluid”. In: *Journal of Fluid Mechanics* 20.2 (1964), pp. 305–314. DOI: 10.1017/S0022112064001227.
[68] J. Meibohm et al. “Angular velocity of a spheroid log rolling in a simple shear at small Reynolds number”. In: *Phys. Rev. Fluids* 1 (8 Dec. 2016), p. 084203. DOI: 10.1103/PhysRevFluids.1.084203.
[69] G. K. Batchelor. “Slender-body theory for particles of arbitrary cross-section in Stokes flow”. In: *Journal of Fluid Mechanics* 44.3 (1970), pp. 419–440. DOI: 10.1017/S002211207000191X.
[70] R. G. Cox. “The motion of long slender bodies in a viscous fluid Part 1. General theory”. In: *Journal of Fluid Mechanics* 44.4 (1970), pp. 791–810. DOI: 10.1017/S002211207000215X.
[71] R. E. Khayat and R. G. Cox. “Inertia effects on the motion of long slender bodies”. In: *Journal of Fluid Mechanics* 209 (1989), pp. 435–462. DOI: 10.1017/S0022112089003174.
[72] K. Gustavsson et al. “Effect of Particle Inertia on the Alignment of Small Ice Crystals in Turbulent Clouds”. In: *Journal of the Atmospheric Sciences* 78.8 (2021), pp. 2573–2587. DOI: 10.1175/JAS-D-20-0221.1.
[73] V. Dabade, N. K. Marath, and G. Subramanian. “Effects of inertia and viscoelasticity on sedimenting anisotropic particles”. In: *Journal of Fluid Mechanics* 778 (2015), pp. 133–188. DOI: 10.1017/jfm.2015.360.
[74] H. Brenner. “The Stokes resistance of a slightly deformed sphere”. In: *Chemical Engineering Science* 19.8 (1964), pp. 519–539. ISSN: 0009-2509. DOI: https://doi.org/10.1016/0009-2509(64)85045-4.

[75] J. C. Prata et al. “Environmental exposure to microplastics: An overview on possible human health effects”. In: *Science of The Total Environment* 702 (2020), p. 134455. ISSN: 0048-9697. DOI: https://doi.org/10.1016/j.scitotenv.2019.134455.

[76] D. Allen et al. “Microplastics and nanoplastics in the marine-atmosphere environment”. In: *Nature Reviews Earth & Environment* 3.6 (June 2022), pp. 393–405. DOI: 10.1038/s43017-022-00292-x.

[77] Y. Cai et al. “The origin of microplastic fiber in polyester textiles: The textile production process matters”. In: *Journal of Cleaner Production* 267 (2020), p. 121970. ISSN: 0959-6526. DOI: https://doi.org/10.1016/j.jclepro.2020.121970.

[78] V. Giurgiu et al. “Full Rotational Dynamics of Plastic Microfibers in Turbulence”. In: *Phys. Rev. Lett.* 133 (5 Aug. 2024), p. 054101. DOI: 10.1103/PhysRevLett.133.054101.

[79] E. J. Tozzi et al. “Settling dynamics of asymmetric rigid fibers”. In: *Physics of Fluids* 23.3 (Mar. 2011), p. 033301. ISSN: 1070-6631. DOI: 10.1063/1.3562253.

[80] J. B. Keller and S. I. Rubinow. “Slender-body theory for slow viscous flow”. In: *Journal of Fluid Mechanics* 75.4 (1976), pp. 705–714. DOI: 10.1017/S0022112076000475.

[81] K. Sassen. “Remote Sensing of Planar Ice Crystal Fall Attitudes”. In: *Journal of the Meteorological Society of Japan. Ser. II* 58.5 (1980), pp. 422–429. DOI: 10.2151/jmsj1965.58.5_422.

[82] K. Gustavsson et al. “Effect of fluid inertia on the orientation of a small prolate spheroid settling in turbulence”. In: *New Journal of Physics* 21.8 (Aug. 2019), p. 083008. DOI: 10.1088/1367-2630/ab3062.

[83] G. Subramanian and D. L. Koch. “Inertial effects on fibre motion in simple shear flow”. In: *Journal of Fluid Mechanics* 535 (2005), pp. 383–414. DOI: 10.1017/S0022112005004829.

[84] T. Bhowmick et al. “Twist, turn and encounter: the trajectories of small atmospheric particles unravelled”. In: *Journal of Fluid Mechanics* 1021 (2025), A27. DOI: 10.1017/jfm.2025.10674.

RESEARCH PAPERS

Paper I

https://doi.org/10.1103/PhysRevFluids.9.024302

Caustic formation in a non-Gaussian model for turbulent aerosols

J. Meibohm,[1] L. Sundberg,[2] B. Mehlig,[2] and K. Gustavsson[2]
[1]*Department of Mathematics, King's College London, London WC2R 2LS, United Kingdom*
[2]*Department of Physics, Gothenburg University, SE-41296 Gothenburg, Sweden*

(Received 19 July 2023; accepted 3 January 2024; published 16 February 2024)

Caustics in the dynamics of heavy particles in turbulence accelerate particle collisions. The rate $\mathscr{J}$ at which these singularities form depends sensitively on the Stokes number St, the nondimensional inertia parameter. Exact results for this sensitive dependence have been obtained using Gaussian statistical models for turbulent aerosols. However, direct numerical simulations of heavy particles in turbulence yield much larger caustic-formation rates than predicted by the Gaussian theory. To understand the possible mechanisms explaining this difference, we analyze a non-Gaussian statistical model for caustic formation in the limit of small St. We show that at small St, $\mathscr{J}$ depends sensitively on the tails of the distribution of Lagrangian fluid-velocity gradients. This explains why different authors obtained different St-dependencies of $\mathscr{J}$ in numerical-simulation studies. The most likely gradient fluctuation that induces caustics at small St, by contrast, is the same in the non-Gaussian and Gaussian models. Direct numerical simulation results for particles in turbulence show that the optimal fluctuation is similar, but not identical, to that obtained by the model calculations.

DOI: 10.1103/PhysRevFluids.9.024302

I. INTRODUCTION

Particle inertia causes heavy particles suspended in an incompressible turbulent flow to cluster and form fractal spatial patterns [1], because it allows the particles to detach from the flow. This happens at caustics, singular points of the particle dynamics, where the volume of the infinitesimal particle neighborhood collapses to zero [2–6]. Between caustics, the particle velocities are multivalued, giving rise to anomalously large relative particle velocities at small separations [3,7–9]. This effect is also known as the "sling effect" [3,10,11]. It causes spatial continuum descriptions of the inertial particle velocity field to fail. To some degree, the nonsmooth contribution from multivaluedness can be modeled using spatially uncorrelated fluctuations [12], or more accurate approaches [13–15].

Theoretical analysis of Gaussian statistical models resolving individual particle trajectories shows that, at small Stokes numbers, caustics form by an optimal fluctuation that involves large fluid strain and zero fluid vorticity [16]. In the plane spanned by the invariants $Q = -\frac{1}{2}\mathrm{Tr}\mathbb{A}^2$ and $R = -\det\mathbb{A}$ of the traceless matrix $\mathbb{A}$ of fluid-velocity gradients, the optimal fluctuation that induces a caustic follows the right branch of the Vieillefosse line $\frac{27}{4}R^2 + Q^3 = 0$ [17]. However, turbulent fluid-velocity gradients are not Gaussian-distributed, which raises the question to which extent non-Gaussian fluctuations change these results.

Published by the American Physical Society under the terms of the Creative Commons Attribution 4.0 International license. Further distribution of this work must maintain attribution to the author(s) and the published article's title, journal citation, and DOI. Funded by Bibsam.

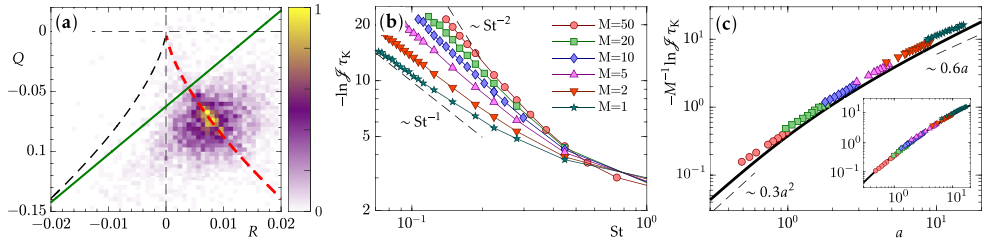

FIG. 1. Caustic formation in a non-Gaussian model for a turbulent aerosol. (a) Probability of Q and R at the onset of caustic formation (color-coded). Parameters: $\mathrm{St} = 0.1$ and $M = 1$. The thick dashed line is the right branch of the Vieillefosse line (see the text). The solid line is the threshold line for caustic formation, Eq. (4). (b) Rate of caustic formation for the non-Gaussian model for different values of M. Also shown are the limiting St scalings, dashed lines. (c) Collapse of the small-St data from panel (b) (markers) onto the scaling function $\mathscr{F}(a)$ given in Eq. (19) (thick black line), using the $\mathrm{St} \to 0$ limit of the scaling variable a in Eq. (1). The inset shows the same, but using the finite Stokes correction for a in Eq. (21) with $\delta\lambda_{\mathrm{th}}$ from the theory in Table I.

To address this question, we formulate a statistical model that exhibits non-Gaussian fluid-velocity statistics, and we analyze caustic formation in the small-St limit [16–20] using optimal-fluctuation theory. We find that the optimal fluctuation agrees with that in the Gaussian models at small St: caustics form along the right branch of the Vieillefosse line [Fig. 1(a)]. The rate of caustic formation $\mathscr{J}\tau_K$, by contrast, depends strongly on the shape of the non-Gaussian tails of the distribution of $\mathbb{A}$. At small Stokes numbers, its St-dependence is determined by a nonuniversal action that is sensitive to the tails of the distribution of fluid-velocity gradients [Fig. 1(b)]. As $\mathrm{St} \to 0$, the rate of caustic formation obeys an asymptotic law in the form

$$-\ln(\mathscr{J}\tau_K) \sim M\mathscr{F}(a) \quad \text{with} \quad a = \frac{\sqrt{d(d+2)}}{4\mathrm{St}\sqrt{M}} + O(\mathrm{St}^{-1/3}), \tag{1}$$

in d spatial dimensions. Here, $\mathscr{F}$ is a scaling function that we determine explicitly, and $M \geqslant 1$ is a model parameter described in Sec. III. Figure 1(c) shows the collapse of the data onto the scaling function $\mathscr{F}(a)$ for small enough St. For $\mathrm{St}\sqrt{M} \gg 1$, the non-Gaussian model coincides with the Gaussian model, and we find inverse quadratic scaling in St, $-\ln(\mathscr{J}\tau_K) \propto \mathrm{St}^{-2}$, in agreement with earlier models [3,18,21]. For $\mathrm{St}\sqrt{M} \ll 1$, by contrast, the St scaling is inversely linear, $-\ln(\mathscr{J}\tau_K) \propto \mathrm{St}^{-1}$. The different St-scalings arise because the rate of caustic formation is determined by the tails of the probability distribution of the fluid-velocity gradients, which depend on the relative magnitudes of M and St. The incomplete collapse of the data in Fig. 1(c) is a finite-St effect discussed in Sec. VI, as indicated by the correction term $O(\mathrm{St}^{-1/3})$ in Eq. (1). Including the leading-order correction in St (Sec. VI) improves the collapse; see the inset of Fig. 1(c).

In contrast to the sensitive dependence of $\mathscr{J}$ on the parameters, the most likely history of fluid-velocity gradients that induces a caustic—the optimal fluctuation—is the same for all parameters M of the non-Gaussian model, and identical to that of the Gaussian model [16,17] for small St. This indicates that the optimal fluctuation that induces a caustic is more robust than the rate of its occurrence, which is strongly model-dependent. To emphasize this point, we compare our results with direct numerical simulations (DNS) of particles in turbulence, and we find qualitative agreement for the optimal fluctuation, providing further evidence for its robustness.

Our results explain why studies aimed at comparing the rate of caustic formation $\mathscr{J}$ from DNS with that from idealized (and often Gaussian) models fail: For small St, $\mathscr{J}$ depends of the tails of the distribution of fluid-velocity gradients, which is non-Gaussian and unknown in general.

II. CAUSTIC FORMATION

In the Stokes approximation, the equation of motion for a small yet heavy spherical particle reads [6]

$$\dot{\boldsymbol{x}} = \boldsymbol{v}, \quad \dot{\boldsymbol{v}} = \tau_{\mathrm{p}}^{-1}[\boldsymbol{u}(\boldsymbol{x}, t) - \boldsymbol{v}]. \tag{2}$$

Here $\boldsymbol{x}$ and $\boldsymbol{v}$ are particle position and velocity, $\boldsymbol{u}(\boldsymbol{x}, t)$ is the turbulent velocity at the particle position at time t, and dots denote time derivatives. Gravitational settling is neglected (the effect of settling on caustic formation is discussed in Refs. [22,23]). The Stokes approximation applies for small enough particles that are much heavier than the fluid. In this limit, particle inertia can nevertheless be important, even when the particles are small. Caustics occur when particle-velocity field folds over configuration space, so that the particle-velocity gradients $\partial v_i/\partial x_j$ tend to $-\infty$ [5,16,17]. To identify caustics, one therefore follows the particle-velocity gradients and determines when they diverge. To this end, one integrates [3]

$$\tau_{\mathrm{p}}\dot{\mathbb{Z}} = \mathbb{A}(\boldsymbol{x}, t) - \mathbb{Z} - \mathbb{Z}^2, \tag{3}$$

alongside Eq. (2). The matrices $\mathbb{A}$ and $\mathbb{Z}$ contain the fluid-velocity gradients $A_{ij} = \tau_{\mathrm{p}}\partial u_i/\partial x_j$ and particle-velocity gradients $Z_{ij} = \tau_{\mathrm{p}}\partial v_i/\partial x_j$ at the particle position, nondimensionalized with the particle-response time τ_{p}. Equations (2) and (3) are used to identify caustic locations. Approaches that aim to resolve the particle number density close to a caustic, by contrast, require also higher-order derivatives of the particle velocity [15,24].

We consider caustic formation at weak particle inertia, $\mathrm{St} \ll 1$. In this case, the dynamics of $\mathbb{Z}$ occurs on a timescale of order τ_{p}, much shorter than τ_{K}, the timescale of changes of $\mathbb{A}$. In this "persistent limit" [16–20], changes of $\mathbb{A}$ can be treated as approximately constant. In this approximation, caustics occur whenever Eq. (3) has no stable fixed points, because then $\mathbb{Z}$ escapes to negative infinity in finite time. In three spatial dimensions, the fixed points of Eq. (3) vanish whenever the fluid-velocity gradients $\mathbb{A}$ exceed a threshold in the Q-R plane, parametrized by the line [17]

$$Q = 4R - \tfrac{1}{16} \quad \text{for} \quad R \geqslant -\tfrac{1}{32}. \tag{4}$$

In the chosen nondimensionalization, the elements of $\mathbb{A}$ are typically of the order of St, and thus small when $\mathrm{St} \ll 1$. Since the threshold (4) is of order unity, this means that rare large fluctuations of $\mathbb{A}$ are needed to reach the threshold line.

An equivalent condition can be formulated in terms of the eigenvalues of $\mathbb{A}$ [16,17,25]. It requires that the most negative eigenvalue of $\mathbb{A}$ be real and drop below a negative threshold that tends to $-1/4$ as $\mathrm{St} \to 0$. In contrast to Eq. (4), this condition is independent of the spatial dimension d.

Inertialess tracers move along the stream lines of the flow and sample configuration space homogeneously [26]. As a consequence, the Lagrangian statistics of $\mathbb{A}$ agrees with the Eulerian one. Inertial particles, by contrast, preferentially sample straining regions [27] and distribute inhomogeneously over configuration space. This leads to different magnitudes of the Lagrangian correlation functions of strain $\mathbb{S} = (\mathbb{A} + \mathbb{A}^{\mathsf{T}})/2$ and vorticity $\mathbb{O} = (\mathbb{A} - \mathbb{A}^{\mathsf{T}})/2$ for finite St [28–31],

$$\langle S_{ij}(t)S_{kl}(t')\rangle = \frac{C_S(\mathrm{St})\mathrm{St}^2}{d(d+2)(d-1)}[d(\delta_{ik}\delta_{jl} + \delta_{il}\delta_{jk}) - 2\delta_{ij}\delta_{kl}]f_S(t-t'), \tag{5a}$$

$$\langle O_{ij}(t)O_{kl}(t')\rangle = \frac{C_O(\mathrm{St})\mathrm{St}^2}{d(d-1)}(\delta_{ik}\delta_{jl} - \delta_{il}\delta_{jk})f_O(t-t'), \quad \langle O_{ij}S_{kl}\rangle = 0. \tag{5b}$$

Here, $f_S(x)$ and $f_O(x)$ are normalized correlation functions with $f_S(0) = f_O(0) = 1$, and $C_S(\mathrm{St})$ and $C_O(\mathrm{St})$ quantify the relative magnitude of strain and vorticity along inertial particle trajectories. Preferential concentration [32,33] leads to $C_S(\mathrm{St}) > C_O(\mathrm{St})$, i.e., strain dominates at finite St [27]. However, preferential concentration is absent for very small St, so that $C_S(\mathrm{St}) = C_O(\mathrm{St}) = 1/2$ for $\mathrm{St} \to 0$.

For Gaussian-distributed fluid-velocity gradients, Eqs. (5) imply that the steady-state probability $P_s(\mathbb{A})$ for the occurrence of a realization $\mathbb{A}$ of fluid-velocity gradients is given by

$$-\ln P_s(\mathbb{A}) \sim \frac{d-1}{4\mathrm{St}^2}\left(\frac{d+2}{C_S}\mathrm{Tr}\mathbb{S}^\mathsf{T}\mathbb{S} + \frac{d}{C_O}\mathrm{Tr}\mathbb{O}^\mathsf{T}\mathbb{O}\right), \tag{6}$$

where we dropped the normalization factor because it is subleading in the limit of small St. To leading order in St, the logarithmic probability for $\mathbb{A}$ to reach the threshold $\mathbb{A}_{\mathrm{th}}$ determines the rate of caustic formation, $-\ln(\mathscr{J}\tau_\mathrm{K}) \sim -\ln P(\mathbb{A}_{\mathrm{th}})$. For Gaussian fluid-velocity gradients (6), this leads to the inverse quadratic scaling in St found in Refs. [16,17], $-\ln(\mathscr{J}\tau_\mathrm{K}) \propto \mathrm{St}^{-2}$ as $\mathrm{St} \to 0$.

III. NON-GAUSSIAN MODEL

Motivated by the fact that turbulent fluid-velocity gradients have non-Gaussian tails, we explore the effects of such tails on caustic formation. To this end, we formulate a non-Gaussian model for the turbulent fluid-velocity gradients $\mathbb{A}$ driving Eq. (3). It is based on an ensemble of M identical, time-independent random velocity fields $\boldsymbol{u}_m(\boldsymbol{x})$, all with identical smooth spatial correlation functions. We superpose these $\boldsymbol{u}_m(\boldsymbol{x})$ with random, time-dependent coefficients $c_m(t)$ to obtain a non-Gaussian model for turbulent fluctuations,

$$\boldsymbol{u}(\boldsymbol{x},t) = \frac{1}{\sqrt{M}}\sum_{m=1}^{M} c_m(t)\boldsymbol{u}_m(\boldsymbol{x}), \quad \mathbb{A}(\boldsymbol{x},t) = \tau_\mathrm{p}\boldsymbol{\nabla}\boldsymbol{u}(\boldsymbol{x},t). \tag{7}$$

Here $c_m(t)$ are independent, identical Gaussian processes with zero mean and covariance,

$$\langle c_m(t)c_n(t')\rangle = \delta_{mn}f(t-t'), \tag{8}$$

where $f(0)=1$ and with the correlation time τ_c of $\boldsymbol{u}(\boldsymbol{x},t)$ defined as $\tau_\mathrm{c} = \int_0^\infty \mathrm{d}t\, f(t)$. For $\sqrt{M} \gg |A_{ij}|$, the central-limit theorem implies that $\mathbb{A}$ is Gaussian-distributed and $P_s(\mathbb{A})$ is given by Eq. (6), so that the results of [16,17] are recovered. For large fluid-velocity gradients and finite M, however, the central-limit theorem does not apply. In this case, the distribution of $\mathbb{A}$ has non-Gaussian tails, whose form we discuss in the next section.

IV. OPTIMAL-FLUCTUATION THEORY

For finite M and large fluid-velocity gradients, the central limit theorem cannot be applied to Eq. (7). In this case, we find by a saddle-point analysis of the non-Gaussian model

$$-\ln P_s(\mathbb{A}) \sim \sqrt{\frac{M(d-1)}{2St^2}\left(\frac{d+2}{C_S}\mathrm{Tr}\,\mathbb{S}^\mathsf{T}\mathbb{S} + \frac{d}{C_O}\mathrm{Tr}\,\mathbb{O}^\mathsf{T}\mathbb{O}\right)}. \tag{9}$$

The derivation of Eq. (9) is summarized in Appendix A. We see that the argument of the square root in Eq. (9) is just $2M$ times the Gaussian action on the right-hand side of Eq. (6), which simplifies the analysis that follows.

As mentioned earlier, at small $\mathrm{St} \ll 1$, caustics form whenever the most negative eigenvalue of $\mathbb{A}$ is real and drops below a negative threshold that tends to $-1/4$ for $\mathrm{St} \to 0$ [16,17,25]. In the persistent limit, the nondimensional rate of caustic formation $\mathscr{J}\tau_\mathrm{K}$ is equal to the probability for this event, $P_s(\mathbb{A}_{\mathrm{th}})$, to leading order in St. To compute this probability, we first express the right-hand side of Eqs. (6) and (9) in terms of the eigenvalues $\boldsymbol{\lambda} = (\lambda_1,\ldots,\lambda_d)^\mathsf{T}$ of $\mathbb{S}$ and in terms of the nonzero singular values $\boldsymbol{\mu} = (\mu_1,\ldots,\mu_{\lfloor d/2\rfloor})^\mathsf{T}$ of $\mathbb{O}$,

$$-\ln P_s(\mathbb{A}) \sim -\ln P_s(\boldsymbol{\lambda},\boldsymbol{\mu}) \sim \mathscr{H}\left[\frac{d-1}{4\mathrm{St}^2}\left(\frac{d+2}{C_S}|\boldsymbol{\lambda}|^2 + \frac{2d}{C_O}|\boldsymbol{\mu}|^2\right)\right], \tag{10}$$

where $\mathscr{H}(x)$ is equal to x for $|A_{ij}| \ll \sqrt{M}$ and equal to $\sqrt{2Mx}$ for $|A_{ij}| \gg \sqrt{M}$. Transforming the joint probability density of $\mathbb{A}$ into the probability of $\boldsymbol{\lambda}$ and $\boldsymbol{\mu}$ in this way involves a Jacobian determinant. This so-called Vandermode determinant, however, is independent of St and therefore does not contribute at this order. We marginalize the distribution (10) over $\lambda_1, \ldots, \lambda_{d-1}$ and $\mu_1, \ldots, \mu_{\lfloor d/2 \rfloor}$ using the contraction principle [34], and we compute

$$-\ln P_s(\lambda_d) \sim \min_{\substack{\lambda_1,\ldots,\lambda_{d-1},\boldsymbol{\mu} \\ \sum_{n=1}^{d}\lambda_n=0}} \mathscr{H}\left[\frac{d-1}{4\mathrm{St}^2}\left(\frac{d+2}{C_S}|\boldsymbol{\lambda}|^2+\frac{2d}{C_O}|\boldsymbol{\mu}|^2\right)\right] \tag{11}$$

by constrained minimization. The constraint $\sum_{n=1}^{d}\lambda_n = 0$ arises because $\mathbb{A}$ must be traceless in incompressible flow. We enforce the constraint by adding a Lagrange multiplier. Evaluating the stationary point of the resulting Lagrangian gives $\lambda_k^* = -\lambda_d/(d-1)$ and $\mu_j^* = 0$, independently of $\mathscr{H}$. This implies that the optimal gradient configuration that leads to a caustic has vanishing vorticity, $\mathbb{O}^* \equiv 0$, as shown in Refs. [16,17], while one of the eigenvalues of $\mathbb{S}^*$, λ_d here, becomes large and negative. All other eigenvalues λ_k are most likely equal and positive, and of $1/(d-1)$ times the magnitude of λ_d, in keeping with the incompressibility constraint. Hence after diagonalization and ordering of the eigenvalues, the most likely threshold configuration to induce a caustic has the form

$$\mathbb{A}_{\mathrm{th}}^* = -\lambda_{\mathrm{th}}\mathbb{e}, \tag{12}$$

where λ_{th} is the threshold value for the most negative eigenvalue of $\mathbb{A}_{\mathrm{th}}^*$, and $\mathbb{e}$ is the diagonal matrix

$$\mathbb{e} = \frac{1}{d-1}\begin{pmatrix} -1 & & & & \\ & -1 & & & \\ & & \cdots & & \\ & & & -1 & \\ & & & & d-1 \end{pmatrix}. \tag{13}$$

For $d = 3$, the fact that all subleading eigenvalues λ_k^* are identical, $\lambda_k^* = \lambda_{\mathrm{th}}/(d-1)$, implies that caustics are most likely induced by fluid-velocity gradients that lie on the Vieillefosse line, not only in the Gaussian [17] but also in the non-Gaussian model. Figure 1(a) shows the excursion of fluid-velocity gradients in the Q-R plane at a time of order τ_{K} before caustic formation, obtained from simulations of the non-Gaussian model with $M = 1$. We see that the fluid-velocity gradients prior to caustic formation lie beyond the threshold (solid line) and close to the Vieillefosse line (thick dashed line), as predicted by our analysis. Note that most gradients in Fig. 1(a) lie considerably below the threshold line. The reason is that at nonzero St [=0.1 in Fig. 1(a)], the threshold λ_{th} is larger than for $\mathrm{St} \to 0$, because the strict separation of timescales breaks down and caustic formation takes a finite time for $\mathrm{St} > 0$. This means that the smallest eigenvalue of the matrix of fluid-velocity gradients must fall below $-1/4$ for a finite time in order to enable caustic formation [16,17,25]. Consequently, at finite St, the threshold value λ_{th} in Eq. (12) must be adjusted, i.e., $\lambda_{\mathrm{th}} = 1/4 + \delta\lambda_{\mathrm{th}}$, where $\delta\lambda_{\mathrm{th}}$ is a correction that vanishes as $\mathrm{St} \to 0$. From the numerical solution of a model system, we show in Sec. V that $\delta\lambda_{\mathrm{th}}$ scales as $\delta\lambda_{\mathrm{th}} \sim \mathrm{St}^{2/3}$ for $\mathrm{St} \ll 1$.

V. SHAPE OF OPTIMAL FLUCTUATION

We now consider the shape of the optimal fluctuation $\mathbb{A}^*(t)$ of fluid-velocity gradients as a function of time that causes the most negative eigenvalue to drop below $-\lambda_{\mathrm{th}}$ at time t_{th}. To this end, we note that the matrix $\mathbb{e}$ in Eq. (12) can be chosen as an element of an orthonormal basis of traceless matrices with respect to the inner product $\langle \mathbb{X}, \mathbb{Y} \rangle = d^{-1}(d-1)\mathrm{Tr}(\mathbb{X}^{\mathsf{T}}\mathbb{Y})$ defined by the trace Tr of the product of two matrices $\mathbb{X}$ and $\mathbb{Y}$. The normalization is chosen here such that $\langle \mathbb{e}, \mathbb{e} \rangle = 1$. In such a basis, the most likely way to reach the threshold $\mathbb{A}_{\mathrm{th}}^*$ is by a large excursion of the amplitude $A^*(t)$ associated with the basis element $\mathbb{e}$,

$$\mathbb{A}^*(t) = A^*(t)\mathbb{e}, \tag{14}$$

while the amplitudes of all other other basis elements remain small. In this way, the amplitude $A^*(t)$ alone determines the shape of the optimal fluctuation $\mathbb{A}^*(t)$ for small St, reflecting the effectively one-dimensional nature of caustic formation at small St [16–18,25]. The eigenvalue threshold $-\lambda_{\rm th}$ in Eq. (12) is then reached when $A^*(t)$ reaches $A^*(t_{\rm th}) = -\lambda_{\rm th}$ at time $t_{\rm th}$.

In the previous section, we discussed that the breakdown of timescale separation increases the threshold value $\lambda_{\rm th}({\rm St})$ for finite St. Using the one-dimensional parametrization (14), we now make this statement more precise by considering the combined dynamics of the optimal fluctuations of fluid-velocity gradients and particle-velocity gradients. To this end, we model the optimal fluctuation $A^*(t)$ as the optimal fluctuation of an Ornstein-Uhlenbeck process. For this particular Gaussian process, the joint optimal fluctuations of the fluid-velocity gradient $A^*(t)$ and the escaping part of the particle-velocity gradient $Z^*(t)$ obey a closed set of differential equations, see e.g. [21] for a derivation. These equations read

$$\frac{\mathrm{d}}{\mathrm{d}t}Z^*(t) = \frac{1}{\rm St}(A^* - Z^* - Z^{*2}), \quad \frac{\mathrm{d}}{\mathrm{d}t}A^*(t) = -A^* + 2\frac{\sigma_S^2}{\kappa_S}p_A, \tag{15a}$$

$$\frac{\mathrm{d}}{\mathrm{d}t}p_z(t) = \frac{1}{\rm St}(1 + 2Z^*)p_z, \quad \frac{\mathrm{d}}{\mathrm{d}t}p_A(t) = \frac{p_A}{\kappa_S} - \frac{1}{\rm St}p_z, \tag{15b}$$

where $0 \leqslant t \leqslant t_{\rm c}$, and p_z and p_A are conjugate momenta that enable nontrivial optimal fluctuations A^* and Z^*. The parameter

$$\sigma_S^2 = \frac{2C_S({\rm St})}{d(d+2)} \tag{16}$$

and the nondimensionalized Lagrangian strain correlation time $\kappa_S = \tau_{\rm K}^{-1}\int_0^\infty \mathrm{d}t\, f_S(t)$ reflect the properties of fluid-velocity gradients along Lagrangian trajectories [28,31] in dimensions $d > 1$. To generate a caustic, Z^* in Eq. (15) must escape from the trivial fixed point $(Z^*, A^*, p_z, p_A) = (0, 0, 0, 0)$ at $t = 0$ and arrive at $Z^* \to -\infty$ at time $t = t_{\rm c}$, the time at which a caustic forms. The condition that the fluctuation be optimal leads to the additional boundary conditions $p_z(t_{\rm c}) = p_A(t_{\rm c}) = 0$.

To find the optimal fluctuation that satisfies Eq. (15) with the prescribed boundary conditions, we employ a numerical shooting method. Taking initial conditions on the unstable subspace of the trivial fixed point, we "shoot" trajectories obeying (15) to "hit" the target boundary condition at $t = t_{\rm th}$. Since the trivial fixed point has two unstable directions, we can parametrize the initial conditions by a single angle θ and write $(Z^*, A^*, p_z, p_A) = \varepsilon(\cos\theta\boldsymbol{e}_1 + \sin\theta\boldsymbol{e}_2)$, with $\varepsilon \ll 1$ at $t = 0$. Here, the vectors $\boldsymbol{e}_1$ and $\boldsymbol{e}_2$ furnish an orthonormal basis of the unstable subspace of the trivial fixed point. By shooting trajectories that obey Eq. (15) with initial conditions parametrized by θ, we optimize θ to hit the target boundary conditions $Z^*(t_{\rm c}) \to -\infty$ and $p_z(t_{\rm c}) = p_A(t_{\rm c}) = 0$. The trajectory $A^*(t)$ obtained in this way gives the amplitude $A^*(t)$ of the optimal fluctuation $\mathbb{A}^*(t)$ in Eq. (14) for small but finite St when the fluid-velocity gradients are Ornstein-Uhlenbeck processes.

To understand how the optimal fluctuation obtained from the shooting method compares with the optimal fluctuation of the non-Gaussian model, we first consider a simplified, one-dimensional model with $\sigma_S^2 = \kappa_S = 1$. Figure 2(a) shows the resulting amplitude $A^*(t)$ for different St plotted versus $t - t_{\rm th}$. We observe that the optimal fluctuation approaches the shape of the correlation function $A^*(t) \to -\frac{1}{4}f_S(t) = -\frac{1}{4}\exp(-|t - t_{\rm th}|/\kappa_S)$ of the Ornstein-Uhlenbeck process with $\kappa_S = 1$ as ${\rm St} \to 0$ [Fig. 2(a)]. This has been shown to be the case for all Gaussian processes in this limit [16,17]. In Appendix B we show that this also holds for the non-Gaussian process studied here, which indicates that the optimal fluctuation of the non-Gaussian model approaches the correlation function in a similar way.

To verify that the optimal fluctuations of the non-Gaussian model for small St follow the same trend as observed in Fig. 2(a) for the Ornstein-Uhlenbeck process, we compare $A^*(t)$ obtained from the shooting method with results of numerical simulations of the non-Gaussian model. To simplify the simulations and to thus allow for smaller St, we consider again the one-dimensional version

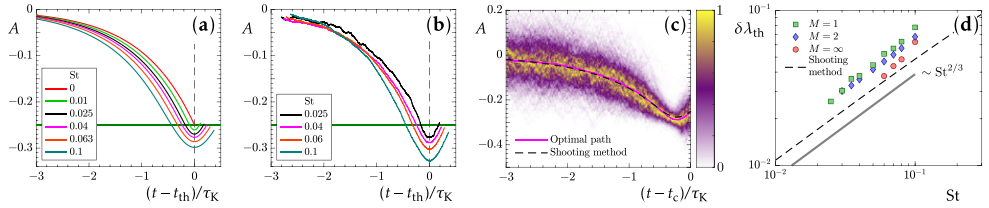

FIG. 2. One-dimensional model for caustic formation. (a) Optimal fluctuations of fluid-velocity gradients, $A^*(t)$, obtained from the shooting method for the Gaussian case (see text) for different St vs $t - t_{\mathrm{th}}$. The thick horizontal line shows the threshold $-\lambda_{\mathrm{th}} = -1/4$. (b) Same as (a) but for simulations of the non-Gaussian model with $M = 1$. The lines show the mean over realizations at each time step. (c) Optimal fluctuation as a function of $t - t_{\mathrm{c}}$ using $M = 1$ and $\mathrm{St} = 0.04$, where t_{c} is the time at which the caustic forms. The color map shows the probability distribution of $A(t)$, normalized at each time step by the maximal probability. The solid line is the mean obtained in panel (b) and the dashed line shows the result from the shooting method in panel (a). (d) The depth $\delta\lambda_{\mathrm{th}}$ of the optimal fluctuation from simulations of the one-dimensional models with $M = 1,\ 2$, and ∞. Also shown are the results of the shooting method (see the text), shown as a dashed line.

of the non-Gaussian model, obtained from Eqs. (7) and (3) with $d = 1$. In the one-dimensional model, the spatial dependence of the fluid-velocity gradients is neglected and the $c_m(t)$ are taken as independent Ornstein-Uhlenbeck processes with $\sigma_S^2 = \kappa_S = 1$. To obtain the optimal fluctuation, we integrate Eqs. (7) and (3) until a caustic forms, and we backtrace the history of the fluid-velocity gradient $A(t)$ prior to caustic formation at $t = t_{\mathrm{c}}$. From the resulting gradient trajectories, we compute for $M = 1$ the mean, shown in Fig. 2(b) for different values of St, and the trajectory density, shown in Fig. 2(c) for one small value of St. We observe that the trajectory density in Fig. 2(c) sharply focuses in a narrow region of high density. This is the optimal fluctuation, which is well approximated by the mean value of the fluid-gradient at each time step (red line).

The mean values in Fig. 2(b) show a similar trend to the Ornstein-Uhlenbeck process in Fig. 2(a), approaching the shape of the correlation function as St becomes smaller. Moreover, Fig. 2(b) shows that for decreasing St the threshold time t_{th} where $A^*(t)$ has its minimum approaches the caustic formation time t_{c}. This implies that after a caustic has been initiated at $t = t_{\mathrm{th}}$, it takes shorter and shorter time for it to form at $t = t_{\mathrm{c}}$ as St decreases. Thus, as $\mathrm{St} \to 0$ caustics form instantaneously whenever the amplitude $A^*(t)$ reaches $-1/4$ [16,17]. Note also that the smaller St is, the larger is the magnitude of $A^*(t)$ at $t = t_{\mathrm{c}}$. Since the optimal fluctuation $A^*(t)$ is a pure strain in our model, this implies that caustic formation events at small St are strongly correlated with straining regions of the flow. This provides an explanation for increased particle collisions in straining regions observed in Refs. [35–37].

The mean value for small St in Fig. 2(c) agrees well with the optimal fluctuation obtained from the shooting method (dashed line), even though $M = 1$, while the shooting method applies strictly only in the limit $M \to \infty$. This suggests that the optimal fluctuation is insensitive to changes of the model when St is small. Further evidence for the robustness of the optimal fluctuation is presented in Fig. 2(d). The figure shows $\delta\lambda_{\mathrm{th}}$, the magnitude by which the optimal fluctuation falls below the value $-1/4$ as a function of St, obtained from numerical simulations of the one-dimensional model and from the shooting method. We observe a mild dependence of $\delta\lambda_{\mathrm{th}}$ on M at finite St, where $M = \infty$ corresponds to the Gaussian model. In the limit $\mathrm{St} \to 0$ all threshold values approach $-1/4$ with scaling $\delta\lambda_{\mathrm{th}} \propto \mathrm{St}^{2/3}$ extracted numerically, albeit with M-dependent prefactors. The same $\mathrm{St}^{2/3}$ scaling can also be obtained from a bound derived in Bätge *et al.* [25] by using the optimal fluctuation to establish a relation between the duration of exceeding the threshold and $\delta\lambda_{\mathrm{th}}$, D, and Δ in their Eq. (8), respectively. We conclude that the optimal fluctuation of fluid-velocity gradients is generally robust against changes of the model. The rate of caustic formation, by contrast, is sensitive to the tails of the distribution, as shown in Fig. 1(b).

TABLE I. Numerically obtained nondimensional Lagrangian strain correlation times κ_S and scaling prefactors $\delta\lambda_{\rm th}{\rm St}^{-2/3}$ for different parameters M in the non-Gaussian model.

M	1	2	5	10	20	50
κ_S	1.33	1.57	1.72	1.81	1.82	1.82
$\delta\lambda_{\rm th}{\rm St}^{-2/3}$	0.19	0.17	0.16	0.16	0.15	0.15

The observed robustness of the optimal fluctuation with respect to changes of M justifies using $A^*(t)$ obtained from the shooting method for finite St as the amplitude for the d-dimensional optimal fluctuation in Eq. (14). With the appropriate parameters $\sigma_S^2 = 2C_S d^{-1}(d+2)^{-1} \sim 1/15$ and κ_S obtained from simulations of the non-Gaussian model in three spatial dimensions, $d = 3$, we numerically extract the small-St scaling of $\delta\lambda_{\rm th}$ from the shooting method. The results are given in Table I. We observe that κ_S depends on M, which introduces a weak M-dependence of the scaling prefactor of $\delta\lambda_{\rm th}$ extracted from the shooting method.

VI. DATA COLLAPSE ONTO SCALING FUNCTION

With the one-dimensional picture (14) of caustic formation developed in the previous section, we now derive the scaling function [black line in Fig. 1(c)] onto which the caustic formation data collapse for small St. To this end, we again diagonalize $\mathbb{A}(t)$ at the time of caustic formation. We then obtain from Eq. (7) the following expression for the component of the fluid velocity gradient that reaches the threshold $\mathbb{A}_{\rm th}$:

$$A(\boldsymbol{x}, t) = \frac{1}{\sqrt{M}} \sum_{m=1}^{M} c_m(t) A_m(\boldsymbol{x}), \tag{17}$$

where $A_m = \langle \mathbb{A}_m, \mathbb{e} \rangle$ is the amplitude of $\mathbb{A}_m$ along the basis matrix $\mathbb{e}$ in Eq. (13). Due to homogeneity and stationarity, the steady-state distribution $P_s(A)$ of A is independent of $\boldsymbol{x}$ and t for any single point in space and time. Furthermore, since c_m and A_m are independent, A follows a large-deviation principle [34] for $M \gg 1$,

$$P_s(A) \propto \exp\left[-M \mathscr{F}\left(\frac{A}{\sqrt{M}\sigma_s {\rm St}}\right)\right], \tag{18}$$

with rate function $\mathscr{F}(a)$. For Gaussian c_m and A_m, the function $\mathscr{F}(a)$ can be obtained explicitly by first computing the generating function of A and applying a Legendre transform [34]. We find

$$\mathscr{F}(a) = \frac{1}{2}\left\{\sqrt{1+(2a)^2} - 1 - \ln\left[\frac{\sqrt{1+(2a)^2}+1}{2}\right]\right\}. \tag{19}$$

For a caustic to form, A in (18) must reach $-\lambda_{\rm th} = -1/4 - \delta\lambda_{\rm th}$. With the large-deviation form in Eq. (18), this leads us to

$$-M^{-1} \ln(\mathscr{J}\tau_{\rm K}) = \mathscr{F}\left(\frac{\lambda_{\rm th}}{\sqrt{M}\sigma_S {\rm St}}\right). \tag{20}$$

Hence, the argument a of the scaling function $\mathscr{F}$ is given by

$$a = \frac{1/4 + \delta\lambda_{\rm th}}{\sqrt{M}\sigma_S {\rm St}}. \tag{21}$$

In the limit of ${\rm St} \to 0$, Eqs. (20) and (21) simplify to Eq. (1). When plotted against the parameter a, the data collapse onto the scaling function $\mathscr{F}(a)$ in Eq. (19) as ${\rm St} \to 0$; see Fig. 1(c). The inset of

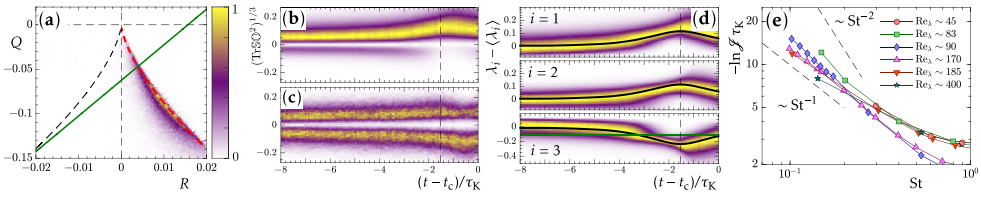

FIG. 3. Caustic formation using direct numerical simulations of turbulence to integrate Eqs. (2) and (3). (a) Color-coded probability density of Q and R at the onset of caustic formation $[(t_{\rm th} - t_{\rm c})/\tau_{\rm K} = -1.53]$. (b) Probability density of the real cube root of the invariant $\mathrm{Tr}(\mathbb{SO}^2)$ before the formation of a caustic at $t = t_{\rm c}$. Dashed line shows the onset time for panel (a). (c) Same as panel (b), but for the statistical model with $M = 1$ and $\mathrm{St} = 0.1$ [the case in Fig. 1(a)]. (d) Probability density of eigenvalues λ_i of $\mathbb{S}$ minus their average values, $\langle\lambda_i\rangle$, evaluated along particle trajectories independent from the formation of caustics. The solid green line shows the $\mathrm{St} \to 0$ limit of the threshold, $\lambda_{\rm th}(\mathrm{St} \to 0) = -1/4$. Solid blue lines show the optimal fluctuation according to theory for the eigenvalues, $\lambda_3(t) - \langle\lambda_3\rangle \sim \lambda_{\rm th}(\mathrm{St}) f_S(t - t_{\rm th})$ and $\lambda_1(t) - \langle\lambda_1\rangle = \lambda_2(t) - \langle\lambda_2\rangle \sim -\frac{1}{2}\lambda_{\rm th}(\mathrm{St}) f_S(t - t_{\rm th})$, with a fitted threshold $\lambda_{\rm th}(\mathrm{St}) \approx -0.23$. Parameters: $\mathrm{Re}_\lambda = 185$ and $\mathrm{St} = 0.3$. The maximal values of the densities are at each time scaled to unity. (e) Rate of caustic formation against Stokes number St. Dashed lines indicate scalings St^{-1} and St^{-2}. Data are obtained from Ref. [10] ($\mathrm{Re}_\lambda = 45, 83$), Ref. [38] ($\mathrm{Re}_\lambda = 90, 170$), and new results using the DNS underlying Refs. [39] ($\mathrm{Re}_\lambda = 185$) and [7] ($\mathrm{Re}_\lambda = 400$).

Fig. 1(c) shows that, for finite values of St, using $\delta\lambda_{\rm th}$ from the shooting method with the prefactors in Table I improves the collapse, even though the shooting method was derived for $M \to \infty$.

We now show that one obtains Eqs. (6) and (9) from the scaling function $\mathscr{F}$ in different limits. First, for $\mathrm{St} \ll 1$ and $\sqrt{M}\mathrm{St} \gg 1$, we have $a \ll 1$ in Eq. (19), so that

$$M\mathscr{F}\left(\frac{\lambda_{\rm th}}{\sqrt{M}\sigma_S \mathrm{St}}\right) \sim \frac{\lambda_{\rm th}^2}{2\sigma_S^2 \mathrm{St}^2}. \tag{22}$$

Second, for $\mathrm{St} \ll 1$ and $\sqrt{M}\mathrm{St} \ll 1$, one has $a \gg 1$, and

$$M\mathscr{F}\left(\frac{\lambda_{\rm th}}{\sqrt{M}\sigma_S \mathrm{St}}\right) \sim \frac{\sqrt{M}\lambda_{\rm th}}{\sigma_S \mathrm{St}}. \tag{23}$$

These expressions agree with Eqs. (6) and (9) at the threshold configuration (12). Hence, the scaling function $\mathscr{F}$ interpolates between the asymptotic St scalings derived in Eqs. (6) and (9).

VII. TURBULENCE

Finally, we discuss the implication of the non-Gaussian model for DNS of particles in turbulence. To this end, we have analyzed data of particle trajectories from DNS [7,39] and earlier DNS results for the rate of caustic formation [10,38]. Figure 3(a) displays the optimal fluctuation at the time of onset of caustic formation, using the trajectory-data set from Ref. [39]. It shows the trajectory density in the Q-R-plane at the time $t_{\rm th}$ when a caustic is initiated. As in the statistical model data shown in Fig. 1(a), the largest probability density lies below the threshold line and close to the right branch of the Vieillefosse line (red dashed line), in qualitative agreement with the theory described above, and with earlier unpublished DNS data [40]. However, we also see quantitative differences between the shapes of the gradient distributions in Figs. 1(a) and 3(a). In particular, the data for turbulent fluid-velocity gradients scatter broadly along and slightly below the Vieillefosse line. For the non-Gaussian model [Fig. 1(a)], by contrast, the scatter appears more centered on the Vieillefosse line.

The elongated scatter of turbulent fluid-velocity gradients is likely due the fact that the nonlinear terms in the Navier-Stokes equations self-amplify fluid-velocity gradients along this branch [41,42].

This generates large gradient excursions and thus leads to anomalously large fluctuations along the right branch of the Vieillefosse line. That the turbulent gradients scatter below the Vieillefosse line, instead of centering on the line as in the non-Gaussian model, can be understood by decomposing $Q = -\mathrm{tr}\mathbb{S}^2/2 + \mathrm{tr}\mathbb{O}\mathbb{O}^{\mathrm{T}}/2$ and $R = -\mathrm{tr}\mathbb{S}^3/3 - \mathrm{tr}\mathbb{S}\mathbb{O}^2$. If $\mathbb{O} = 0$, no pair of (R, Q) may lie above the Vieillefosse line by its definition. In this case, the distribution is concentrated just below the Vieillefosse line, for both the Gaussian model and the DNS (not shown). The effect of nonzero $\mathbb{O}$ is to first shift Q upwards, because $\mathrm{tr}\mathbb{O}\mathbb{O}^{\mathrm{T}} \geqslant 0$. Second, a negative value of $\mathrm{tr}\mathbb{S}\mathbb{O}^2$ shifts R to the right, and vice versa. This explains why the DNS data lie below the Vieillefosse line in the Q-R plane. The reason is that $\mathrm{tr}\mathbb{S}\mathbb{O}^2$ is unlikely to take negative values. This is apparent from Figure 3(b), which shows that the probability to have negative $\mathrm{tr}\mathbb{S}\mathbb{O}^2$ is very small at the onset of caustic formation (the onset time is indicated by the vertical dashed line). This peculiar coupling between strain and vorticity as the strain grows large is specific to turbulence. In the statistical model, the distribution of $\mathrm{tr}\mathbb{S}\mathbb{O}^2$ is almost symmetric, see Fig. 3(c), explaining why the data in Fig. 1(a) are scattered both above and below the Vieillefosse line.

The strong interrelation between strain and vorticity in turbulence discussed above also results in vorticity giving a finite, correlated contribution to the optimal fluctuation of Q (not shown) [43]. This is in contrast to the Gaussian and non-Gaussian models considered here, where the optimal vorticity contribution vanishes [16,17]. Despite these differences, the shape of the optimal fluctuation in the DNS is still quite well approximated by the correlation function, as shown in Fig. 3(d), where the trajectory density of the eigenvalues of the turbulent strain $\mathbb{S}$ is depicted prior to caustic formation. The optimal fluctuation theory described above assumes that the mean values $\langle\lambda_i\rangle$ vanish. This is consistent, because they are of higher order than $\delta\lambda \sim \mathrm{St}^{2/3}$ for small St. Since the Stokes number in Fig. 3(d) is not very small, we subtracted the mean values from λ_i. The solid blue lines show the theoretical predictions for the optimal fluctuations, given by the correlation function f_S of $\mathbb{S}$ normalised to a fitted threshold value. We observe qualitative agreement.

Finally, Fig. 3(e) shows the St-dependence of the rate of caustic formation $\mathscr{J}\tau_{\mathrm{K}}$ for particles in turbulence from Refs. [10,38], using DNS with different Reynolds numbers Re_λ. In the literature, different authors have fitted different exponents, ranging between -1 and -2, to the St-dependence of $-\ln \mathscr{J}\tau_{\mathrm{K}}$ [10,38], motivated by results for the rate of caustic formation in Gaussian statistical models [5]. The data in Fig. 3(e) appear to be consistent with inverse linear scaling St^{-1} for some of the cases, but the scaling exponent depends strongly on Re_λ. This is consistent with the observations in Ref. [25] and supported by the analysis of the non-Gaussian statistical model: the small-St scaling of $-\ln \mathscr{J}\tau_{\mathrm{K}}$ is strongly affected by the extreme-value statistics of fluid-velocity gradients in turbulence, not captured by Gaussian models.

VIII. CONCLUSIONS

We formulated a non-Gaussian statistical model for turbulent aerosols, with non-Gaussian tails of the distribution of fluid-velocity gradients. We analyzed how caustics form in this model at small Stokes numbers, in the persistent limit. Using large-deviation theory, we computed the rate of caustic formation for the non-Gaussian model, and we demonstrated that caustic formation is sensitive to the tails of the distribution of fluid-velocity gradients, because they must overcome a threshold for a caustic to form: The smaller the Stokes number, the larger the fluid-velocity gradients must be to initiate a caustic. For $\mathrm{St} \lessapprox 0.1$, the required fluid-velocity gradients lie far in the tails of the distribution.

While the rate of caustic formation depends sensitively on the tails of the fluid-velocity gradient distribution seen by the particles, the form of the optimal fluctuation is robust against changes of the parameters in the non-Gaussian model. In particular, the optimal fluctuation of the non-Gaussian model has small vorticity, just like the Gaussian one, and it follows the right branch of the Vieillefosse line at small Stokes numbers.

What are the implications of these results for caustics in three-dimensional homogeneous isotropic turbulent flow? First, our analysis of the non-Gaussian model shows that the rate of caustic

formation is sensitive to the tails of the fluid-velocity gradient distribution. As a consequence, the rate of caustic formation is not expected to have a simple scaling form such as St^{-1} or St^{-2}. This explains why numerical studies of the rate of caustic formation using direct numerical simulation of turbulence at different Reynolds numbers yielded inconclusive results [10,38], simply because the St-dependence of $-\ln(\mathscr{J}\tau_{\mathrm{K}})$ is not a power law. These conclusions are consistent with the results of Ref. [25], in which the Reynolds-number dependence of the rate of caustic formation was analyzed using DNS of turbulence. Second, the optimal fluctuation of fluid-velocity gradients leading to caustic formation in turbulence is similar to the predictions of our non-Gaussian model. In particular, the fluid-velocity gradients that initiate caustics in turbulence lie close to the right branch of the Vieillefosse line. This robustness explains why particle collisions in turbulence tend to occur close to the Vieillefosse line [37]. Third, the vorticity contribution to the optimal fluctuation in turbulence, however, is not simply scattered around zero but performs a small yet correlated excursion. This suggests an interdependence of vorticity and strain in the tails of the joint distribution of turbulent strain and vorticity [25]. We remark that one can produce an optimal fluctuation with nonzero vorticity by adding third- and fourth-order terms to the (quadratic) Gaussian action in Eq. (6). Whether or not the finite optimal vorticity in turbulence has a similar origin is an open question.

ACKNOWLEDGMENTS

The research of L.S. and B.M. was supported in part by VR Grant No. 2021-4452. K.G. was supported by VR Grant No. 2018-03974. J.M. was funded by a Feodor-Lynen Fellowship of the Alexander von Humboldt-Foundation. The statistical-model simulations were conducted using the resources of HPC2N provided by the Swedish National Infrastructure for Computing (SNIC), partially funded by the Swedish Research Council through Grant Agreement No. 2018-05973. We thank Luca Biferale for granting access to the DNS data needed to generate the results in Fig. 3.

APPENDIX A: DERIVATION OF EQ. (1)

Here we show that the rate of caustic formation for the non-Gaussian model (7) is of the form (1) at small St. To this end, we express $\mathbb{A}$ in terms of the uncorrelated components

$$A^i(t) = \langle \mathbb{e}^i, \mathbb{A}(t)\rangle, \tag{A1}$$

where $\mathbb{e}_i$, $i = 1, \ldots, N_d$ furnish a basis of traceless matrices, such that $\langle \mathbb{e}^i, \mathbb{e}^j\rangle = \delta_{ij}$, with the inner product defined in Sec. V and $\mathbb{e}^{N_s} \equiv \mathbb{e}$ given in Eq. (13). These $N_d = d^2 - 1$ basis elements can be split into a set of $N_s = (d-1)(d+2)/2$ symmetric and $N_O = d(d-1)/2$ antisymmetric traceless matrices, where d is the spatial dimension. From the non-Gaussian model (7), we then obtain

$$A^i(\boldsymbol{x}, t) = \frac{1}{\sqrt{M}} \sum_{m=1}^{M} c_m(t) A_m^i(\boldsymbol{x}). \tag{A2}$$

For different m, the $A_m^i(\boldsymbol{x}) = \langle \mathbb{e}^i, \mathbb{A}_m\rangle$ are uncorrelated Gaussian random variables with zero mean, and thus independent. We define $\boldsymbol{A} = (A^1, \ldots, A^{N_d})^{\mathsf{T}} = (\boldsymbol{S}, \boldsymbol{O})^{\mathsf{T}}$, where $\boldsymbol{S} = (S^1, \ldots, S^{N_S})^{\mathsf{T}}$ and $\boldsymbol{O} = (O^1, \ldots, O^{N_O})^{\mathsf{T}}$. The vectors $\boldsymbol{S}$ and $\boldsymbol{O}$ correspond to the strain $\mathbb{S}$ and vorticity $\mathbb{O}$ parts of $\mathbb{A}$, respectively. We also introduce $\boldsymbol{A}_m = (A_m^1, \ldots, A_M^{N_d})^{\mathsf{T}} = (\boldsymbol{S}_m, \boldsymbol{O}_m)^{\mathsf{T}}$, where $\boldsymbol{S}_m = (S_m^1, \ldots, S_m^{N_S})^{\mathsf{T}}$ and $\boldsymbol{O}_m = (O_m^1, \ldots, O_m^{N_O})^{\mathsf{T}}$. The latter have the covariances

$$\left\langle S_m^i(\boldsymbol{x}) S_n^j(\boldsymbol{x})\right\rangle = \delta_{nm}\delta^{ij}\mathrm{St}^2\sigma_S^2, \quad \left\langle O_m^i(\boldsymbol{x}) O_n^j(\boldsymbol{x})\right\rangle = \delta_{nm}\delta^{ij}\mathrm{St}^2\sigma_O^2, \tag{A3}$$

and $\langle S_m^i(\boldsymbol{x}) O_n^j(\boldsymbol{x})\rangle = 0$, where σ_S^2 is given in Eq. (16) and

$$\sigma_O^2 = \frac{2C_O(\mathrm{St})}{d^2}. \tag{A4}$$

For the following calculation, it is convenient to introduce the variables $\tilde{\boldsymbol{A}} = (\boldsymbol{S}, \boldsymbol{O}\sigma_S/\sigma_O)^{\mathsf{T}}$ and $\tilde{\boldsymbol{A}}_m = (S_m, O_m\sigma_S/\sigma_O)$, so that all $\tilde{A}^i$ and $\tilde{A}^i_m$ with $i = 1, \ldots, N_d$ have the same variance σ_S. We now write the time and space independent steady-state distribution $P_s(\mathbb{A})$ in terms of $\boldsymbol{S}$ and $\boldsymbol{O}$. To this end, we first compute $P_s(\tilde{\boldsymbol{A}})$ and transform the result to obtain $P_s(\mathbb{A})$ for $\mathbb{A} \gg \mathrm{St}$. We have

$$P_s(\tilde{\boldsymbol{A}}) = \left\langle \prod_{i=1}^{N_S} \delta\left(\tilde{A}^i - \frac{\boldsymbol{c}\cdot\boldsymbol{A}^i}{\sqrt{M}}\right) \prod_{i=1}^{N_O} \delta\left(\tilde{A}^{N_S+i} - \frac{\boldsymbol{c}\cdot\boldsymbol{A}^{N_S+i}\sigma_S/\sigma_O}{\sqrt{M}}\right)\right\rangle, \tag{A5}$$

where $\boldsymbol{A}^i = (A^i_1, \ldots, A^i_M)^{\mathsf{T}}$ and $\boldsymbol{c} = (c_1, \ldots, c_M)^{\mathsf{T}}$. The random variables A^i_m and $c_m(t)$ are independent and Gaussian. After the change of variables $\boldsymbol{c} \to \boldsymbol{c}/\sqrt{\sigma_S}$, $\boldsymbol{A}^i \to \boldsymbol{A}^i\sqrt{\sigma_S}$, $\boldsymbol{A}^{N_S+i} \to \boldsymbol{A}^{N_S+i}\sigma_O/\sqrt{\sigma_S}$, the average in Eq. (A5) is expressed as the multidimensional Gaussian integral:

$$P_s(\tilde{\boldsymbol{A}}) = N_{\boldsymbol{A}} N_{\boldsymbol{c}} \int_{\mathbb{R}^{M\times N_d}} \prod_{i=1}^{N_d} \mathrm{d}\boldsymbol{A}^i \int_{\mathbb{R}^M} \mathrm{d}\boldsymbol{c} \prod_{i=1}^{N_d} \delta\left(\tilde{A}^i - \frac{\boldsymbol{c}\cdot\boldsymbol{A}^i}{\sqrt{M}}\right) \mathrm{e}^{-\frac{1}{2\sigma_S \mathrm{St}^2}(|\boldsymbol{c}|^2 + \sum_{i=1}^{N_d}|\boldsymbol{A}^i|^2)}, \tag{A6}$$

where $N_{\boldsymbol{A}}$ and $N_{\boldsymbol{c}}$ are appropriate normalization factors. For $\mathrm{St} \ll 1$ the integral can be evaluated by a saddle-point approximation, subject to the constraints in the δ-functions. We thus minimize the Lagrange function

$$\mathscr{L} = \frac{|\boldsymbol{c}|^2}{2} + \sum_{i=1}^{N_d} \frac{|\boldsymbol{A}^i|^2}{2} - \sum_{i=1}^{N_d} \beta_i(\tilde{A}^i - \boldsymbol{c}\cdot\boldsymbol{A}^i/\sqrt{M}), \tag{A7}$$

where β_i are Lagrange multipliers that enforce the constraints. Minimization

$$\left.\frac{\partial\mathscr{L}}{\partial\boldsymbol{A}^i}\right|_{\boldsymbol{A}^*,\boldsymbol{c}^*} = 0, \quad \left.\frac{\partial\mathscr{L}}{\partial\boldsymbol{c}}\right|_{\boldsymbol{A}^*,\boldsymbol{c}^*} = 0, \tag{A8}$$

leads to the saddle-point equations

$$\boldsymbol{A}^{*i} + \frac{\beta_i\boldsymbol{c}^*}{\sqrt{M}} = 0, \quad \boldsymbol{c}^* + \sum_{j=1}^{N_d} \frac{\beta_j\boldsymbol{A}^{*j}}{\sqrt{M}} = 0. \tag{A9}$$

We take the inner product of $\boldsymbol{A}^{*i}$ and the second equation in Eq. (A9). Using the constraints on the inner product gives

$$\tilde{A}^i + \frac{1}{M}\sum_{j=1}^{N_d} \beta_j \boldsymbol{A}^{*i}\cdot\boldsymbol{A}^{*j} = 0 \tag{A10}$$

for $i = 1, \ldots, N_d$. Taking the inner product of the first equation in Eq. (A9) with $\boldsymbol{A}^{*i}$ and $\boldsymbol{A}^{*j}$, $j \neq i$, and substituting the result into the previous equation, gives the relations

$$|\boldsymbol{\beta}|^2 = M, \quad \beta_i\tilde{A}^j = \beta_j\tilde{A}^i, \tag{A11}$$

where $\boldsymbol{\beta} = (\beta_1, \ldots, \beta_{N_d})^{\mathsf{T}}$. Solving these equations for $\boldsymbol{\beta}$ gives

$$\beta_i = -\frac{\sqrt{M}\tilde{A}^i}{\sqrt{\sum_{j=1}^{N_d}(\tilde{A}^j)^2}}. \tag{A12}$$

Further, substituting Eq. (A9) into Eq. (A7), we obtain

$$\mathscr{L} = -\sum_{i=1}^{N_d} \beta_i\tilde{A}^i = \sqrt{M|\tilde{A}|^2}. \tag{A13}$$

Transforming back, $\tilde{A} \to (\boldsymbol{S}, \boldsymbol{O})$, we find that the joint probability density of $\boldsymbol{S}$ and $\boldsymbol{O}$ takes the form

$$-\ln P(\boldsymbol{S}, \boldsymbol{O}) \sim \mathrm{St}^{-1}\sqrt{M\big(|\boldsymbol{S}|^2/\sigma_S^2 + |\boldsymbol{O}|^2/\sigma_O^2\big)}. \tag{A14}$$

Hence, up to the prefactor $\sqrt{M}$ and a factor of 2, the asymptotic action of the components A^i in the non-Gaussian model is equal to the square-root of the Gaussian action. This shows that $\mathscr{H}(x) = \sqrt{2Mx}$ for $|A_{ij}| \gg \sqrt{M}$ as stated in the main text.

APPENDIX B: OPTIMAL FLUCTUATION

Here we analyze the shape of the optimal fluctuation $\mathbb{A}^*(t)$ of fluid-velocity gradients in the non-Gaussian model for $\mathrm{St} \to 0$ in terms of the amplitude $A^*(t)$ given in Eq. (14). For Gaussian processes, an optimal fluctuation $A^*(t)$ that reaches a given threshold $|\lambda_{\mathrm{th}}| \gg \sigma_S$ at time $t = t_{\mathrm{th}}$ is given by the correlation function, $A^*(t) = \lambda_{\mathrm{th}} f_S(t - t_{\mathrm{th}})$, normalized to the threshold value λ_{th} [16,17]. We now show that the optimal fluctuation has the same form for the non-Gaussian model when $\mathrm{St} \to 0$.

Since we are dealing with a one-dimensional process, it is enough to consider single component $A(t) \equiv A^{N_s}(t)$ along $\mathbb{e}^{N_s} \equiv \mathbb{e}$. For the probability $P_s(A = -\lambda_{\mathrm{th}})$, this is equivalent to considering the Gaussian integral in Eq. (A6) with $N_d = 1$. For $|\lambda_{\mathrm{th}}| \gg \sqrt{M}$, the integral is dominated by the saddle point $(\boldsymbol{A}^*, \boldsymbol{c}^*)$, where $\boldsymbol{A}^* = (A_1^{*N_s}, \ldots, A_M^{*\,N_s})^{\mathsf{T}}$ and $\boldsymbol{c}^* = (c_1^{*N_s}, \ldots, c_M^{*\,N_s})^{\mathsf{T}}$. Since the process $\boldsymbol{c}(t)$ is Gaussian, $\boldsymbol{c}^*(t)$ reaches $\boldsymbol{c}^*$ at time t by an optimal fluctuation $\boldsymbol{c}^*(t)$ of the form [16,17]

$$\boldsymbol{c}^*(t) = \boldsymbol{c}^* f_S(t - t_{\mathrm{th}}). \tag{B1}$$

The saddle point $(A^*, \boldsymbol{c}^*)$ is determined by Eq. (A9). The optimal fluctuation $A^*(t)$ is then obtained by taking the inner product with $\boldsymbol{A}^*$ and dividing by $\sqrt{M}$:

$$A^*(t) = \frac{1}{\sqrt{M}}\boldsymbol{A}^* \cdot \boldsymbol{c}^* f_S(t - t_{\mathrm{th}}) = -\lambda_{\mathrm{th}} f_S(t - t_{\mathrm{th}}). \tag{B2}$$

This shows that in the limit $\mathrm{St} \to 0$, the optimal fluctuation $A^*(t)$ for the non-Gaussian process $A(t)$ that reaches $-\lambda_{\mathrm{th}}$ at time t has, just as in the Gaussian case, the shape of the correlation function of the constituting processes $\boldsymbol{c}(t)$, normalized to the threshold value $-\lambda_{\mathrm{th}}$, as stated in the main text.

[1] J. Bec, Fractal clustering of inertial particles in random flows, Phys. Fluids **15**, L81 (2003).

[2] A. Crisanti, M. Falcioni, A. Provenzale, P. Tanga, and A. Vulpiani, Dynamics of passively advected impurities in simple two-dimensional flow models, Phys. Fluids **4**, 1805 (1992).

[3] G. Falkovich, I. Fouxon, and M. G. Stepanov, Acceleration of rain initiation by cloud turbulence, Nature (London) **419**, 151 (2002).

[4] M. Wilkinson and B. Mehlig, Caustics in turbulent aerosols, Europhys. Lett. **71**, 186 (2005).

[5] K. Gustavsson and B. Mehlig, Statistical models for spatial patterns of heavy particles in turbulence, Adv. Phys. **65**, 1 (2016).

[6] J. Bec, K. Gustavsson, and B. Mehlig, Statistical models for the dynamics of heavy particles in turbulence, Annu. Rev. Fluid Mech. **56**, 189 (2024).

[7] J. Bec, L. Biferale, M. Cencini, A. Lanotte, and F. Toschi, Intermittency in the velocity distribution of heavy particles in turbulence, J. Fluid Mech. **646**, 527 (2010).

[8] J. P. L. C. Salazar and L. R. Collins, Inertial particle relative velocity statistics in homogeneous isotropic turbulence, J. Fluid Mech. **696**, 45 (2012).

[9] K. Gustavsson and B. Mehlig, Relative velocities of inertial particles in turbulent aerosols, J. Turbul. **15**, 34 (2014).

[10] G. Falkovich and A. Pumir, Sling effect in collisions of water droplets in turbulent clouds, J. Atmos. Sci **64**, 4497 (2007).
[11] G. Bewley, E. W. Saw, and E. Bodenschatz, Observation of the sling effect, New J. Phys. **15**, 083051 (2013).
[12] P. Fevrier, O. Simonin, and K. D. Squires, Partitioning of particle velocities in gas-solid turbulent flows into a continuous field and a spatially uncorrelated random distribution: Theoretical formalism and numerical study, J. Fluid Mech. **533**, 1 (2005).
[13] L. Ducasse and A. Pumir, Inertial particle collisions in turbulent synthetic flows: Quantifying the sling effect, Phys. Rev. E **80**, 066312 (2009).
[14] R. H. A. Ijzermans, E. Meneguz, and M. W. Reeks, Segregation of particles in incompressible random flows: singularities, intermittency and random uncorrelated motion, J. Fluid Mech. **653**, 99 (2010).
[15] A. Papoutsakis, O. D. Rybdylova, T. S. Zaripov, L. Danaila, A. N. Osiptsov, and S. S. Sazhin, Modelling of the evolution of a droplet cloud in a turbulent flow, Int. J. Multiphase Flow **104**, 233 (2018).
[16] J. Meibohm, V. Pandey, A. Bhatnagar, K. Gustavsson, D. Mitra, P. Perlekar, and B. Mehlig, Paths to caustic formation in turbulent aerosols, Phys. Rev. Fluids **6**, L062302 (2021).
[17] J. Meibohm, K. Gustavsson, and B. Mehlig, Caustics in turbulent aerosols form along the Vieillefosse line at weak particle inertia, Phys. Rev. Fluids **8**, 024305 (2023).
[18] S. A. Derevyanko, G. Falkovich, K. Turitsyn, and S. Turitsyn, Lagrangian and Eulerian descriptions of inertial particles in random flows, J. Turbul. **8**, N16 (2007).
[19] J. Meibohm, L. Pistone, K. Gustavsson, and B. Mehlig, Relative velocities in bidisperse turbulent suspensions, Phys. Rev. E **96**, 061102(R) (2017).
[20] J. Meibohm and B. Mehlig, Heavy particles in a persistent random flow with traps, Phys. Rev. E **100**, 023102 (2019).
[21] K. Gustavsson and B. Mehlig, Distribution of velocity gradients and rate of caustic formation in turbulent aerosols at finite Kubo numbers, Phys. Rev. E **87**, 023016 (2013).
[22] J. Bec, H. Homann, and S. Sankar Ray, Gravity-driven enhancement of heavy particle clustering in turbulent flow, Phys. Rev. Lett. **112**, 184501 (2014).
[23] K. Gustavsson, S. Vajedi, and B. Mehlig, Clustering of particles falling in a turbulent flow, Phys. Rev. Lett. **112**, 214501 (2014).
[24] A. Papoutsakis and M. Gavaises, A model for the investigation of the second-order structure of caustic formations in dispersed flows, J. Fluid Mech. **892**, A4 (2020).
[25] T. Bätge, I. Fouxon, and M. Wilczek, Quantitative prediction of sling events in turbulence at high reynolds numbers, Phys. Rev. Lett. **131**, 054001 (2023).
[26] G. Falkovich, K. Gawędzki, and M. Vergassola, Particles and fields in fluid turbulence, Rev. Mod. Phys. **73**, 913 (2001).
[27] M. R. Maxey, The gravitational settling of aerosol particles in homogeneous turbulence and random flow fields, J. Fluid Mech. **174**, 441 (1987).
[28] S. S. Girimaji and S. B. Pope, A diffusion model for velocity gradients in turbulence, Phys. Fluids A **2**, 242 (1990).
[29] B. K. Brunk, D. L. Koch, and L. W. Lion, Hydrodynamic pair diffusion in isotropic random velocity fields with application to turbulent coagulation, Phys. Fluids **9**, 2670 (1997).
[30] L. I. Zaichik and V. M. Alipchenkov, Pair dispersion and preferential concentration of particles in isotropic turbulence, Phys. Fluids **15**, 1776 (2003).
[31] D. Vincenzi, S. Jin, E. Bodenschatz, and L. R. Collins, Stretching of polymers in isotropic turbulence: A statistical closure, Phys. Rev. Lett. **98**, 024503 (2007).
[32] K. D. Squires and J. K. Eaton, Preferential concentration of particles by turbulence, Phys. Fluids A **3**, 1169 (1991).
[33] J. K. Eaton and J. R. Fessler, Preferential concentration of particles by turbulence, Int. J. Multiphase Flow **20**, 169 (1994).
[34] H. Touchette, The large deviation approach to statistical mechanics, Phys. Rep. **478**, 1 (2009).
[35] V. E. Perrin and H. J. J. Jonker, Preferred location of droplet collisions in turbulent flows, Phys. Rev. E **89**, 033005 (2014).

[36] J. R. Picardo, L. Agasthya, R. Govindarajan, and S. S. Ray, Flow structures govern particle collisions in turbulence, Phys. Rev. Fluids **4**, 032601(R) (2019).
[37] S. Lee and C. Lee, Identification of a particle collision as a finite-time blowup in turbulence, Sci. Rep. **13**, 181 (2023).
[38] A. Bhatnagar, V. Pandey, P. Perlekar, and D. Mitra, Rate of formation of caustics in heavy particles advected by turbulence, Philos. Trans. R. Soc. A **380**, 20210086 (2022).
[39] J. Bec, L. Biferale, G. Boffetta, M. Cencini, S. Musacchio, and F. Toschi, Lyapunov exponents of heavy particles in turbulence, Phys. Fluids **18**, 091702 (2006).
[40] A. Bhatnagar (unpublished).
[41] P. Vieillefosse, Local interaction between vorticity and shear in a perfect incompressible fluid, J. Phys. France **43**, 837 (1982).
[42] P. Vieillefosse, Internal motion of a small element of fluid in an inviscid flow, Physica A **125**, 150 (1984).
[43] T. Bätge (private communication).

Paper II

https://doi.org/10.1103/PhysRevResearch.7.013179

Torques on curved atmospheric fibers

F. Candelier [1], K. Gustavsson [2], P. Sharma [3], L. Sundberg,[2] A. Pumir [4,3], G. Bagheri [3], and B. Mehlig [2]

[1]*Aix-Marseille Université, CNRS, IUSTI, Marseille, France*

[2]*Department of Physics, Gothenburg University, Gothenburg SE-40530, Sweden*

[3]*Max Planck Institute for Dynamics and Self-Organization, 37077 Göttingen, Germany*

[4]*CNRS and Ecole Normale Supérieure de Lyon, Laboratoire de Physique UMR55672, F-69364 Lyon, France*

(Received 20 September 2024; accepted 17 January 2025; published 18 February 2025)

Small particles are transported over long distances in the atmosphere, with significant environmental impact. The transport of symmetric particles is well understood, but atmospheric particles, such as curved microplastic fibers or ash particles, are generally asymmetric. This makes the description of their transport properties uncertain. Here, we derive a model of how planar curved fibers settle in quiescent air. The model explains that fluid-inertia torques may align such fibers at oblique angles with gravity as seen in recent laboratory experiments, and shows that inertial alignment is a general and thus important factor for the transport of atmospheric particles.

DOI: 10.1103/PhysRevResearch.7.013179

I. INTRODUCTION

Atmospheric transport is a major dispersal pathway of microplastic particles [1,2], with negative environmental impact [3,4], and potentially affecting cloud-formation processes [5,6]. Therefore it is important to develop reliable models of particle transport in the atmosphere [3,7]. A challenge is that atmospheric particles, such as curved microplastic fibers [8,9], tend to be asymmetric. Theoretical models have focused on symmetric shapes [10,11], which are now considered in the most advanced numerical models of atmospheric transport [12,13]. However, shape asymmetry may affect the transport of atmospheric fibers. This aspect is at best taken into account by empirical correlations, derived from experimental measurements [14].

Fluid-inertia torques may align fibers as they settle in the atmosphere. Particle-shape symmetry dictates how this happens: axisymmetric fibers with fore-aft symmetry for example align so that their broad side points down, as they settle in a quiescent fluid at moderate particle Reynolds numbers [15–22]. In this case, only one angle matters (the angle between the symmetry vector of the fiber and its center-of-mass velocity). This mechanism is important in the atmospheric sciences, as it is thought to align symmetric ice platelets and columns in weakly turbulent ice clouds [11,23–27]. Laboratory experiments in viscous cellular flow [28], in a turbulent water-oil mixture [20], for ensembles of fibers in quiescent and turbulent air [29–31], and for spheroids in quiescent air [32] show that the inertial-torque models work quantitatively for axisymmetric particles with fore-aft symmetry. Moreover, breaking of fore-aft symmetry causes small axisymmetric particles to tilt as they settle [33–36].

Curved atmospheric fibers neither possess fore-aft symmetry nor are they axisymmetric. How do shape asymmetries of curved fibers affect inertial torques and thus the angular dynamics? To answer this question, we developed a model for the angular dynamics of curved microplastic fibers. The model predicts how forces and torques depend on the fiber orientation, parametrized by its tilt angle θ and its spin angle ψ, see Fig. 1(a), as well as its shape and size. The model explains why current transport models of atmospheric fibers [10,12,13] work for the component of the settling speed in the direction of gravity, but fail to describe the sensitive shape dependence of the angular dynamics seen in the experiments [14]. In particular, fibers may align at oblique angles [Fig. 1(b)], resulting for example in fiber transport perpendicular to gravity. More generally, our results highlight how shape asymmetry affects the delicate effects of fluid inertia for typical atmospheric particles.

II. MODEL

Newton's equations of motion read

$$\frac{\mathrm{d}}{\mathrm{d}t}\boldsymbol{x}_{\mathrm{com}} = \boldsymbol{v}, \quad m\dot{\boldsymbol{v}} = \boldsymbol{F}_{\mathrm{h}} + \boldsymbol{F}_{g}, \tag{1a}$$

$$\frac{\mathrm{d}}{\mathrm{d}t}\boldsymbol{n} = \boldsymbol{\omega}\wedge\boldsymbol{n}, \quad \frac{\mathrm{d}}{\mathrm{d}t}\boldsymbol{p} = \boldsymbol{\omega}\wedge\boldsymbol{p}, \quad \frac{\mathrm{d}}{\mathrm{d}t}(\mathbb{J}\boldsymbol{\omega}) = \boldsymbol{T}_{\mathrm{h}}, \tag{1b}$$

with mass m, center of mass $\boldsymbol{x}_{\mathrm{com}}$, and inertia tensor $\mathbb{J}$ of the fiber, gravity force $\boldsymbol{F}_{g} = m\boldsymbol{g}$, hydrodynamic force $\boldsymbol{F}_{\mathrm{h}}$, and torque $\boldsymbol{T}_{\mathrm{h}}$. Equation (1b) is written with respect to the center of mass $\boldsymbol{x}_{\mathrm{com}}$ of the fiber, so there is no gravity torque. The vectors $\boldsymbol{p}$, $\boldsymbol{q}$, and $\boldsymbol{n}$ denote the particle-fixed coordinate system [Fig. 1(a)]. We consider fibers in the form of circle segments with different radii of curvature, R. Examples are semicircular fibers and quarter circles. The fiber diameter is denoted by $2b$, the contour length by $2a$. The aspect ratio is $\kappa = a/b$.

Published by the American Physical Society under the terms of the Creative Commons Attribution 4.0 International license. Further distribution of this work must maintain attribution to the author(s) and the published article's title, journal citation, and DOI. Funded by Bibsam.

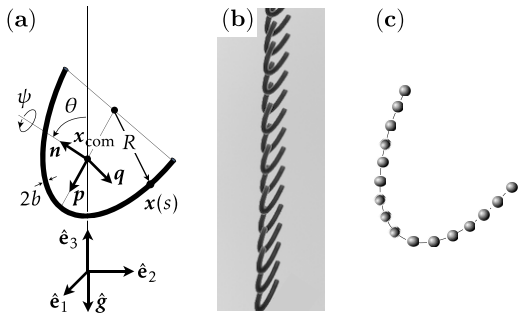

FIG. 1. (a) Particle geometry and particle-fixed coordinate system $\boldsymbol{p}, \boldsymbol{q}, \boldsymbol{n}$. Euler angles θ and ψ ($Z_\phi Y_\theta Z_\psi$ convention; see Supplemental Material [37] for details). We refer to θ as the tilt angle and ψ as the spin angle. For $\phi = \theta = \psi = 0$, the system $\boldsymbol{p}, \boldsymbol{q}, \boldsymbol{n}$ aligns with the laboratory system $\hat{\mathbf{e}}_1, \hat{\mathbf{e}}_2, \hat{\mathbf{e}}_3$. Also shown is the center of mass $\boldsymbol{x}_{\rm com}$, the origin of the particle-fixed coordinate system, and the two radii of the fiber, b and R. The fiber is drawn to depict the stable orientation of the experimentally observed semicircular fibers with length 1 mm, diameter 50 μm. (b) Stacked video stills of a semicircular microplastic fiber settling in air with an oblique tilt angle θ; fiber length 1 mm, diameter 50 μm, data from Ref. [14]. Gravity $\hat{\boldsymbol{g}}$ points down. (c) Illustration of the model used in the Stokes limit, consisting of hydrodynamically interacting beads.

III. STOKES LIMIT

In a quiescent fluid, the Stokes force and torque on the particle are [38]

$$\begin{bmatrix} \boldsymbol{F}_{\rm h}^{(0)} \\ \boldsymbol{T}_{\rm h}^{(0)} \end{bmatrix} = -\mu \begin{bmatrix} \mathbb{A} & \mathbb{B}^{\mathsf{T}} \\ \mathbb{B} & \mathbb{C} \end{bmatrix} \begin{bmatrix} \boldsymbol{v} \\ \boldsymbol{\omega} \end{bmatrix}. \tag{2}$$

Here $\boldsymbol{v}$ is the center-of-mass velocity, $\boldsymbol{\omega}$ is the angular velocity around $\boldsymbol{x}_{\rm com}$, μ is the dynamic viscosity of the fluid, and $\mathbb{A}, \mathbb{B}, \mathbb{C}$ are resistance tensors. These tensors are constrained by particle-shape symmetries [39]. Two reflection symmetries cause all elements of $\mathbb{B}$ to vanish in the particle-fixed coordinate system, except $B_{qn} = \boldsymbol{q} \cdot \mathbb{B}\boldsymbol{n}$, and B_{nq}. The tensors $\mathbb{A}$ and $\mathbb{C}$ are diagonal in this coordinate system.

In order to determine how the fibers settle in the Stokes limit, we seek the steady states of Eqs. (1) with $\boldsymbol{F}_{\rm h} = \boldsymbol{F}_{\rm h}^{(0)}$ and $\boldsymbol{T}_{\rm h} = \boldsymbol{T}_{\rm h}^{(0)}$. This is accurate when the particle Reynolds number $\mathrm{Re}_a = av^*/\nu$ is very small, where v^* is the steady-state settling speed of the fiber, and ν is the kinematic viscosity of air. Setting $\dot{\boldsymbol{v}} = \dot{\boldsymbol{n}} = \dot{\boldsymbol{p}} = \dot{\boldsymbol{\omega}} = 0$ in Eqs. (1) yields two steady states: $(\theta^*, \psi^*) = (\frac{\pi}{2}, 0)$ ($\boldsymbol{p}$ points down), and $(\frac{\pi}{2}, \pi)$ ($\boldsymbol{p}$ points up). Both steady states have $\boldsymbol{\omega}^* = 0$ and $\boldsymbol{v}^* = (0, 0, -v_g^*)$ with $v_g^* = mg/(\mu A_{pp})$. Linear stability analysis shows that the stability of the steady states depends on the signs of B_{qn} and B_{nq} (see Supplemental Material (SM) [37] for details). We computed the nonzero elements of the resistance tensors using the method of Durlofsky [40–42], modeling the fibers as chains of hydrodynamically interacting beads with radius b [Fig. 1(c)]. This gives $B_{qn} > 0$ and $B_{nq} < 0$ (Table S1 in the SM [37]). In this case, $\psi^* = 0$ is stable, while $\psi^* = \pi$ is unstable. So the fibers settle with $\boldsymbol{n}$ orthogonal to the settling velocity, and $\boldsymbol{p}$ points down.

IV. FLUID-INERTIA TORQUE

At larger Re_a, the Stokes approximation fails because fluid-inertia torques affect the angular dynamics. We calculated the fluid-inertia torque for our curved fibers by expanding slender-body theory [16] to order $\mathrm{Re}_a = av^*/\nu$. In the (right-handed) particle-fixed coordinate system from Fig. 1(a) we find

$$T_{p,M}^{(1)}/(2\pi\mu\nu a^2) = \frac{av}{\nu(\ln\kappa)^2} a_{p,M}\hat{v}_q\hat{v}_n, \tag{3a}$$

$$T_{q,M}^{(1)}/(2\pi\mu\nu a^2) = \frac{av}{\nu(\ln\kappa)^2} a_{q,M}\hat{v}_p\hat{v}_n, \tag{3b}$$

$$T_{n,M}^{(1)}/(2\pi\mu\nu a^2) = \frac{av}{\nu(\ln\kappa)^2}\big(a_{n,M}\hat{v}_q\hat{v}_p + b_{n,M}\hat{v}_q + c_{n,M}\hat{v}_q\hat{v}_n^2 + d_{n,M}\hat{v}_q^3\big). \tag{3c}$$

Here $\hat{v}_p = \boldsymbol{p} \cdot \hat{\boldsymbol{v}}$ with $\hat{\boldsymbol{v}} = \boldsymbol{v}/v$, and so forth. The geometrical coefficients $a_{p,M}, a_{q,M}, \ldots$ are given in the SM [37]. They depend only on the parameter M determining the central angle $2\pi/M$ of the circle segment ($M = 2$ for a semicircle, $M = 4$ for a quarter circle). Figure 2 shows the angular dependence of the fluid-inertia torque (3) for a semicircular fiber with $\hat{\boldsymbol{v}} = -\hat{\mathbf{e}}_3$.

Circle segments lack fore-aft symmetry and axisymmetry, but the remaining shape symmetry constrains the possible terms in Eq. (3). However, symmetry arguments allow for terms that do not occur in Eq. (3). The reason may be that the slender-body approximation for $\boldsymbol{T}^{(1)}$ neglects hydrodynamic interactions between different parts of the fiber to order $(\ln\kappa)^{-2}$ [41,43].

To understand how fluid inertia changes the angular dynamics, we search for steady states using $\boldsymbol{F}_{\rm h} = \boldsymbol{F}_{\rm h}^{(0)}$ and $\boldsymbol{T}_{\rm h} = \boldsymbol{T}_{\rm h}^{(0)} + \boldsymbol{T}_{\rm h}^{(1)}$ in Eqs. (1), neglecting Re_a corrections to the force at first. Symmetry implies that $v_q^* = 0$ and $\psi^* = 0$. Thus we seek solutions of

$$0 = -\mu A_{pp} v_p + mg\sin\theta, \tag{4a}$$

$$0 = -\mu A_{nn} v_n - mg\cos\theta, \tag{4b}$$

$$0 = -\mu B_{qn} v_n + \frac{\mu a^3}{\nu(\ln\kappa)^2} 2\pi a_{q,M} v_p v_n. \tag{4c}$$

Equations (4) admit two steady states, one with $v_n^* = 0$, and the other one with $v_n^* \neq 0$. The first steady state is stable when $T_q^{(1)}$ is weak enough, and it is the same as in the Stokes limit: $\theta^* = \pi/2$, $\psi_1^* = 0$, $v_q^* = v_n^* = 0$, and $v_p^* = v_g^* = mg/(\mu A_{pp})$. This fixed point becomes unstable in a pitchfork bifurcation as the fluid-inertia torque increases. The bifurcation occurs when

$$A'_{pp} B'_{qn} (\ln\kappa)^2 = 2\pi a_{q,M} \mathscr{R}\mathscr{V}. \tag{5}$$

Here we use nondimensional variables and parameters: $A'_{pp} = A_{pp}/a$, $B'_{qn} = B_{qn}/a^2$, the particle-to-fluid mass-density ratio $\mathscr{R} = \rho_p/\rho_f$, and $\mathscr{V} = 2\pi ab^2 g/\nu^2 = \pi d_{\rm eq}^3 g/(6\nu^2)$, a nondimensional volume [32], and $d_{\rm eq}$ is the volume-equivalent diameter of the fiber. The product $\mathscr{R}\mathscr{V}$ is proportional to Ga^2. The Galileo number Ga measures the ratio of gravity to viscous forces [44]. For small particle Reynolds numbers, $\mathscr{R}\mathscr{V} \propto \mathrm{Re}_a$ up to a geometry-dependent factor. Thus

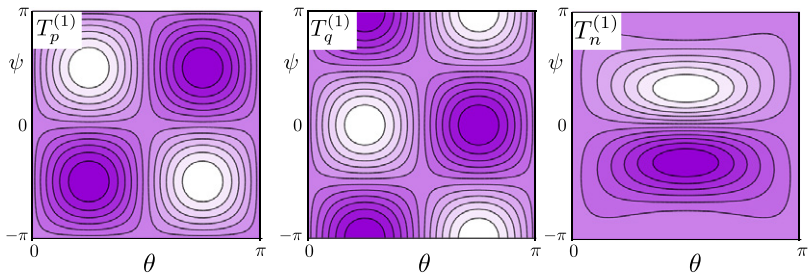

FIG. 2. Inertial torques for the semicircular fiber. Shown are the angular dependencies of $T_p^{(1)}/T_p^{(1,\max)}$, $T_q^{(1)}/T_q^{(1,\max)}$, and $T_n^{(1)}/T_n^{(1,\max)}$ of the inertial torque around the three axes of the particle-fixed coordinate system, obtained from Eq. (3) for $\hat{\boldsymbol{v}} = -\hat{\mathbf{e}}_3$ ($\hat{v}_p = \sin\theta\cos\psi$, $\hat{v}_q = -\sin\theta\sin\psi$, and $\hat{v}_n = -\cos\theta$). Color bar: from -1 (white) to 1 (violet).

larger $\mathscr{RV}$ implies larger fluid-inertia torques. Beyond the bifurcation—for large enough $\mathscr{RV}$—two stable steady states form, with stable orientation

$$\theta^* = \arcsin\left(\frac{A'_{pp}B'_{qn}(\ln\kappa)^2}{2\pi a_{q,M}\mathscr{RV}}\right) \tag{6}$$

(and the equivalent $\pi - \theta^*$ due to symmetry). We conclude: the plane containing the curved fiber in its steady-state orientation tilts when the argument of arcsin in Eq. (6) is smaller than unity, so that $\theta^* \neq \pi/2$. Equation (6) for θ^* is qualitatively similar to that for axisymmetric particles with broken fore-aft symmetry [33,34,36]. For the curved fibers, Eq. (6) is a consequence of broken symmetry under $\boldsymbol{p} \to -\boldsymbol{p}$. We note that fluid inertia does not change the value of ψ^*.

V. EXPERIMENTAL DATA

Using the Göttingen turret [32], Tatsii *et al.* [14] measured the settling speeds of curved fibers (quarter circles and semicircles) with different lengths L and aspect ratios κ, and mass density $\varrho_p = 1200\ \mathrm{kg/m^3}$, comparable to that of common microplastic fibers in the atmosphere. Here we extracted the angular dynamics from the video recordings (see SM [37] for details). The results (Table I) are qualitatively consistent with the theory outlined above, except for the fibers with the largest fluid-inertia parameters $\mathscr{RV}$ which do not align. As predicted by the theory, all other fibers settle with steady orientations with $\psi^* = 0$. For quarter circles, the steady tilt angle is $\theta^* \approx \frac{\pi}{2}$, so $\mathscr{RV}$ is below the bifurcation analyzed above. Semicircular fibers, by contrast, settle with a $\mathscr{RV}$-dependent tilt angle. As predicted by the theory, $\theta^* \approx \frac{\pi}{2}$ for small $\mathscr{RV}$, and θ^* decreases as $\mathscr{RV}$ increases.

For a quantitative comparison, the model must be improved to account for the fact that Re_a is not small in the experiment, so that the small-Re_a theory (3) does not directly apply. Moreover, we expect that fluid-inertia corrections to the force—neglected above—may be significant. To improve the model, we computed the fluid-inertia corrections to torque and force in the full slender-body theory [16] by numerical integration of Eqs. (S13), (S14), and (S19) in the SM [37]. Then we searched for steady-state values $\boldsymbol{v}^*$ and θ^* numerically, for the fibers listed in Table I. The results of these calculations are summarized in Fig. 3. Panels (a) and (b) compare the experimental $\langle v_g\rangle$ (Fig. 2(a) in Ref. [20]) for the fibers from Table I with the full theory for the gravity component v_g^* of the steady settling velocity, as functions of the fluid-inertia parameter $\mathscr{RV}$. We observe excellent agreement.

Panel (c) compares the theory for θ^* with the experiments for semicircular fibers. For small $\mathscr{RV}$, the Stokes torque dominates, yielding stable settling $\theta^* = \frac{\pi}{2}$. For larger $\mathscr{RV}$, the fibers settle at oblique angles with gravity. Compared with the experiment, theory gives smaller values of θ^* in the transition region between small and large $\mathscr{RV}$. Here the steady-state tilt angle is sensitive to the precise form of the hydrodynamic torque, as evident from the estimate of the theoretical uncertainty shown in panel (c) (see discussion below). Panel (d) shows that the theory works well for the quarter circles too.

TABLE I. Summary of experimental results for semicircular and quarter-circular fibers. Parameters: contour length $2a$ (mm), diameter $2b$ (mm), average settling speed $\langle v_g\rangle$ (m/s) from Table 1 in Ref. [14], experimental particle Reynolds number $\mathrm{Re}_a \approx a\langle v_g\rangle/\nu$, with kinematic viscosity of air $\nu = 1.5\times10^{-5}\ \mathrm{m^2/s}$, inertia parameter $\mathscr{RV}$ (see text). Steady-state angles ψ^* (rad) and θ^* (rad) [Fig. 1(a)] extracted from the data [14] as described in the SM [37]. Number N of experiments analyzed.

κ	$2a$	$2b$	$\langle v_g\rangle$	Re_a	$\mathscr{RV}$	ψ^*	θ^*	N
Semicircular fibers								
20	2	0.1	0.704	47	660	[a]	[a]	9
	1	0.05	0.288	9.6	83	0.013 ± 0.024	1.21 ± 0.1	8
50	2	0.04	0.218	14.5	110	0	0.79	1
	1	0.02	0.086	2.9	13	0	1.54	1
100	2	0.02	0.094	6.2	26	0	1.48 ± 0.13	5
	1	0.01	0.037	1.24	3.3	[b]	[b]	0
Quarter-circular fibers								
20	2	0.1	0.631	42	660	[a]	[a]	8
	1	0.05	0.265	8.8	83	-0.03 ± 0.01	1.34 ± 0.13	10
	0.5	0.025	0.096	1.6	10	-0.017	1.414	1
50	2	0.04	0.209	14.0	110	-0.003 ± 0.017	1.48 ± 0.06	11
	1	0.02	0.074	2.5	13	0	1.43 ± 0.07	2
100	2	0.02	0.080	5.3	26	0	1.379	1
	1	0.01	0.026	0.88	3.3	[b]	[b]	0

[a]No steady state observed.
[b]Fiber images blurred; orientations could not be determined.

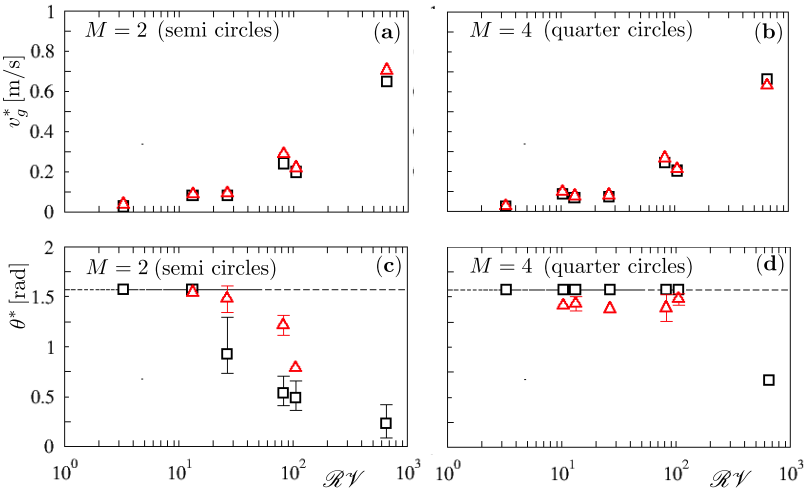

FIG. 3. Comparison between theory and experiment (Table I). (a) Full slender-body theory (see text) for v_g^* for semicircular fibers versus the inertia parameter $\mathscr{RV}$ (□); experimental $\langle v_g \rangle$ (red △). (b) Same, but for quarter circles. (c) Theory for steady-state tilt angle θ^* for semicircular fibers (□). Estimated theoretical uncertainties (see text) are shown when larger than the symbol size. Experiment (red △) with errors from Table I. Dashed line corresponds to $\theta^* = \frac{\pi}{2}$. (d) Same, but for quarter circles (theoretical uncertainty not shown).

For $\mathscr{RV} = 660$, quarter circles and semicircles continue to tumble in the experiments. Our model indicates that this may be explained by a second bifurcation around $\mathscr{RV} = 660$ that results in either a long transient toward, or a change of stability of, θ^*.

VI. DISCUSSION

Our model shows that the component v_g^* of the settling velocity is almost independent of the nondimensional radius of curvature $R/a = M/\pi$, and only weakly dependent on its aspect ratio κ, in agreement with the experiment [Figs. 3(a) and 3(b) and Table I]. For slender fibers, the weak κ dependence is explained because the aspect ratio enters only as $\ln \kappa$ in the model (at fixed $\mathscr{V}$). The weak dependence on R/a is explained by the fact that the elements of $\mathbb{A}$ are similar for quarter circles and semicircles, and that the M dependence of the fluid-inertia force compensates for this dependence, in part. In summary, our model shows that the variation of v_g^* for different fibers is mainly determined by the parameter $\mathscr{RV}$. We conclude: this is the most important parameter for empirical settling models for slender fibers (but note that v_g^* for a slender fiber differs from that of a sphere of equivalent volume [10,14,32]).

Regarding the angular dynamics, the conclusions are quite different. The experiments show that curved fibers settle at a steady tilt angle θ^* that depends sensitively on the nondimensional radius of curvature R/a, as well as on $\mathscr{RV}$. In particular, quarter circles and semicircles settle quite differently [Figs. 3(c) and 3(d)] for the same size and value of $\mathscr{RV}$. Our theory shows that this difference is a consequence of the bifurcation. The Stokes torque decreases more slowly than the fluid-inertia torque as one straightens the fiber by increasing R/a, shifting the location of the bifurcation for quarter circles to larger values of $\mathscr{RV}$. Beyond the bifurcation, the model predicts significant motion perpendicular to gravity that is not explained by existing empirical models. We find $v_\perp/v_g \approx 0.13$ to 0.15 for the first three data points after the bifurcation in Fig. 3(c). In conclusion, atmospheric transport models of slender fibers must account not only for $\mathscr{RV}$, but also for the radius of curvature.

The theory also explains why fluid inertia does not change the steady-state spin angle; it remains $\psi^* = 0$ as in the Stokes limit. This follows from the shape symmetry of the fiber. But note that imperfections (shape asymmetries or density inhomogeneities) may break this symmetry, causing ψ^* to change, distorting the patterns in Fig. 2. Note also that nonplanar fibers may continue to rotate in the Stokes limit [45], like chiral ribbons [42] and taco-shaped disks [46]. How fluid inertia affects this dynamics is not known.

Overall, Fig. 3 shows good agreement between model and experiment, except near the bifurcation, where the tilt angle is sensitive to the details of the hydrodynamic torque. We stress that the model does not contain any fitting parameters, unlike that in, e.g., Ref. [32].

We now discuss possible shortcomings of the full model, and the deviations between model and experiment for θ^* near the bifurcation. For straight cylinders, Fintzi *et al.* [47] assessed the accuracy of slender-body theory by direct numerical simulation (DNS), comparing to Ref. [16], and to higher-order calculations [48]. They find that the theory of Khayat and Cox [16] fails to quantitatively account for contributions to force and torque from the lateral surfaces (end caps) of the cylinder for $\mathrm{Re}_a > 1$ and $\kappa < 30$. The upstream end cap causes larger deviations than the downstream one. Since the end caps of our steadily settling fibers tend to lie downstream,

we expect slender-body theory to work somewhat better for that orientation. Near the bifurcation, θ^* depends sensitively on forces and torques; therefore it is hard to say whether these shortcomings of slender-body theory increase or decrease θ^*. For this reason, we include an estimate of the theoretical uncertainty in Fig. 3(c), showing by how much θ^* changes when increasing/decreasing fluid-inertia torque and force by $\pm 10\%$. Slender-body theory for the Stokes torque requires even larger values of κ [43]. We avoided the latter problem by computing the Stokes torque using the method of Ref. [40].

In some cases, the experiments show that steady-state alignment is approached in an oscillatory fashion, for example as $\psi(t) \sim \cos(\omega t + \varphi)\exp(-\lambda t)$ (Fig. S3 in the SM [37]). This is qualitatively explained by linear stability theory in the Stokes limit. Fluid inertia, however, is expected to have a significant effect on the transient. This remains to be worked out.

For the largest values of $\mathscr{RV}$, the experiments show unsteady angular dynamics (no steady state within $\sim$30 s; Fig. S2 in the SM [37]). This is analogous to the DNS results of Auguste *et al.* [49] and the experiments of Tinklenberg *et al.* [50] for disks settling at Re ~ 100, where periodic angular dynamics can coexist with steady alignment. Our model may qualitatively explain such behavior, because our numerics indicates that there is a second bifurcation near $\mathscr{RV} = 660$ where oblique settling becomes unstable. However, the DNS results for straight fibers of Fintzi *et al.* [47] indicate that our model is at best qualitatively correct for $\mathscr{RV} = 660$.

VII. CONCLUSIONS

Microplastic fibers in the atmosphere settle rapidly because their mass density is about 1000 times higher than that of air. Particle Reynolds numbers based on the fiber half-length are of order 10 for 1 mm fibers. Since microplastic fibers tend to be curved, we analyzed through model calculations how curvature affects the settling dynamics of such fibers. Our model explains why curved fibers may align at oblique angles, depending intricately on their shapes, causing transport perpendicular to the settling direction. The model exemplifies how shape-symmetry breaking affects the angular dynamics of atmospheric particles. This is important because such particles are often asymmetric, just like the curved fibers discussed here, atmospheric ice crystals which usually have imperfections that break shape symmetries [51], and volcanic-ash particles. For atmospheric particles with highly irregular shapes it may be of interest to generalize the present model to random aggregates.

The angular dynamics of symmetric particles settling in turbulent air has recently been studied in detail [11,32,52], indicating that the effect of weak air turbulence can be described by adding a stochastic driving to Eq. (1). Since the observed alignment timescale is of the same order as typical Kolmogorov times for air turbulence [32], the alignment dynamics analyzed in still air matters also for turbulence, and it must be accounted for in transport models of atmospheric particles. A crucial difference to symmetric particles is, however, that asymmetric particles can exhibit intricate angular dynamics already in the Stokes limit [9,53].

To conclude, we stress that the conceptually simple case of curved fibers considered here is only one example of the many asymmetric shapes found in the atmosphere, and that the present study uncovers essential physics relevant for a broad class of atmospheric particles.

ACKNOWLEDGMENTS

This work was supported by Vetenskapsrådet under Grants No. 2021-4452 (B.M., L.S.), No. 2018-03974, and No. 2023-03617 (K.G.). F.C. thanks J. Gissinger for testing the implementation of the bead model. We thank E. Bodenschatz for support and discussions.

[1] S. Allen, D. Allen, F. Baladima, V. R. Phoenix, J. L. Thomas, G. Le Roux, and J. E. Sonke, Evidence of free tropospheric and long-range transport of microplastic at Pic du Midi Observatory, Nat. Commun. **12**, 7242 (2021).

[2] Y. Zhang, S. Kang, S. Allen, D. Allen, T. Gao, and M. Sillanpää, Atmospheric microplastics: A review on current status and perspectives, Earth Sci. Rev. **203**, 103118 (2020).

[3] D. Allen, S. Allen, S. Abbasi, A. Baker, M. Bergmann, J. Brahney, T. Butler, R. A. Duce, S. Eckhardt, N. Evangeliou *et al.*, Microplastics and nanoplastics in the marine-atmosphere environment, Nat. Rev. Earth Environ. **3**, 393 (2022).

[4] J. C. Prata, J. P. da Costa, I. Lopes, A. C. Duarte, and T. Rocha-Santos, Environmental exposure to microplastics: An overview on possible human health effects, Sci. Total Environ. **702**, 134455 (2020).

[5] M. Aeschlimann, G. Li, Z. A. Kanji, and D. M. Mitrano, Potential impacts of atmospheric microplastics and nanoplastics on cloud formation processes, Nat. Geosci. **15**, 967 (2022).

[6] L. E. Revell, P. Kuma, E. C. Le Ru, W. R. C. Somerville, and S. Gaw, Direct radiative effects of airborne microplastics, Nature (London) **598**, 462 (2021).

[7] J. Brahney, N. Mahowald, M. Prank, G. Cornwell, Z. Klimont, H. Matsui, and K. A. Prather, Constraining the atmospheric limb of the plastic cycle, Proc. Natl. Acad. Sci. USA **118**, e2020719118 (2021).

[8] Y. Cai, D. M. Mitrano, M. Heuberger, R. Hufenus, and B. Nowack, The origin of microplastic fiber in polyester textiles: The textile production process matters, J. Cleaner Prod. **267**, 121970 (2020).

[9] V. Giurgiu, G. C. A. Caridi, M. De Paoli, and A. Soldati, Full rotational dynamics of plastic microfibers in turbulence, Phys. Rev. Lett. **133**, 054101 (2024).

[10] S. Xiao, Y. Cui, J. Brahney, N. M. Mahowald, and Q. Li, Long-distance atmospheric transport of microplastic fibres influenced by their shapes, Nat. Geosci. **16**, 863 (2023).

[11] K. Gustavsson, M. Z. Sheikh, A. Naso, A. Pumir, and B. Mehlig, Effect of particle inertia on the alignment of small ice crystals in turbulent clouds, J. Atmos. Sci. **78**, 2573 (2021).

[12] F. Beckett, E. Rossi, B. Devenish, C. Witham, and C. Bonadonna, Modelling the size distribution of aggregated volcanic ash and implications for operational atmospheric dispersion modelling, Atmos. Chem. Phys. **22**, 3409 (2022).

[13] L. Bakels, D. Tatsii, A. Tipka, R. Thompson, M. Dütsch, M. Blaschek, P. Seibert, K. Baier, S. Bucci, M. Cassiani *et al.*, FLEXPART version 11: Improved accuracy, efficiency, and flexibility, EGUsphere **2024**, 1 (2024).

[14] D. Tatsii, S. Bucci, T. Bhowmick, J. Guettler, L. Bakels, G. Bagheri, and A. Stohl, Shape matters: Long-range transport of microplastic fibers in the atmosphere, Environ. Sci. Technol. **58**, 671 (2024).

[15] R. G. Cox, The steady motion of a particle of arbitrary shape at small Reynolds numbers, J. Fluid Mech. **23**, 625 (1965).

[16] R. E. Khayat and R. G. Cox, Inertia effects on the motion of long slender bodies, J. Fluid Mech. **209**, 435 (1989).

[17] G. Subramanian and D. L. Koch, Inertial effects on fibre motion in simple shear flow, J. Fluid Mech. **535**, 383 (2005).

[18] V. Dabade, N. K. Marath, and G. Subramanian, Effects of inertia and viscoelasticity on sedimenting anisotropic particles, J. Fluid Mech. **778**, 133 (2015).

[19] U. Menon, A. Roy, S. Kramel, G. Voth, and D. Koch, Theoretical predictions of the orientation distribution of high-aspect-ratio, inertial particles settling in isotropic turbulence, abstract Q36.00011, 70th Annual Meeting of the APS Division of Fluid Dynamics, Denver, Colorado, 2017 (unpublished).

[20] A. Roy, S. Kramel, U. Menon, G. A. Voth, and D. L. Koch, Orientation of finite Reynolds number anisotropic particles settling in turbulence, J. Non-Newtonian Fluid Mech. **318**, 105048 (2023).

[21] F. Cabrera-Booman, M. Z. Sheikh, B. Mehlig, N. Plihon, M. Bourgoin, A. Pumir, and A. Naso, Experimental validation of fluid inertia models for a cylinder settling in a quiescent flow, Phys. Rev. Fluids **7**, 024301 (2022).

[22] F. Jiang, L. Zhao, H. I. Andersson, K. Gustavsson, A. Pumir, and B. Mehlig, Inertial torque on a small spheroid in a stationary uniform flow, Phys. Rev. Fluids **6**, 024302 (2021).

[23] K. Sassen, Remote sensing of planar ice crystal fall attitudes, J. Meteorol. Soc. Jpn. **58**, 422 (1980).

[24] J. D. Klett, Orientation model for particles in turbulence, J. Atmos. Sci. **52**, 2276 (1995).

[25] F.-M. Bréon and B. Dubrulle, Horizontally oriented plates in clouds, J. Atmos. Sci. **61**, 2888 (2004).

[26] V. Noel and K. Sassen, Study of planar ice crystal orientations in ice clouds from scanning polarization lidar observations, J. Appl. Meteorol. **44**, 653 (2005).

[27] K. Gustavsson, M. Z. Sheikh, D. Lopez, A. Naso, A. Pumir, and B. Mehlig, Effect of fluid inertia on the orientation of a small prolate spheroid settling in turbulence, New J. Phys. **21**, 083008 (2019).

[28] D. Lopez and E. Guazzelli, Inertial effects on fibers settling in a vortical flow, Phys. Rev. Fluids **2**, 024306 (2017).

[29] R. K. Newsom and C. W. Bruce, The dynamics of fibrous aerosols in a quiescent atmosphere, Phys. Fluids **6**, 521 (1994).

[30] R. K. Newsom and C. W. Bruce, Orientational properties of fibrous aerosols in atmospheric turbulence, J. Aerosol Sci. **29**, 773 (1998).

[31] J.-L. Pierson, Inertial settling of an arbitrarily oriented cylinder in a quiescent flow: From short-time to quasisteady motion, Phys. Rev. Fluids **8**, 104301 (2023).

[32] T. Bhowmick, J. Seesing, K. Gustavsson, J. Guettler, Y. Wang, A. Pumir, B. Mehlig, and G. Bagheri, Inertia induces strong orientation fluctuations of nonspherical atmospheric particles, Phys. Rev. Lett. **132**, 034101 (2024).

[33] F. Candelier and B. Mehlig, Settling of an asymmetric dumbbell in a quiescent fluid, J. Fluid Mech. **802**, 174 (2016).

[34] A. Roy, R. J. Hamati, L. Tierney, D. L. Koch, and G. A. Voth, Inertial torques and a symmetry breaking orientational transition in the sedimentation of slender fibres, J. Fluid Mech. **875**, 576 (2019).

[35] S. Ravichandran and J. S. Wettlaufer, Orientation dynamics of two-dimensional concavo-convex bodies, Phys. Rev. Fluids **8**, L062301 (2023).

[36] Z. Maches, M. Houssais, A. Sauret, and E. Meiburg, Settling of two rigidly connected spheres, J. Fluid Mech. **995**, A15 (2024).

[37] See Supplemental Material at http://link.aps.org/supplemental/10.1103/PhysRevResearch.7.013179 for detailed information regarding the theory, the analysis of the video recordings, and the results of this analysis, which contains Ref. [54].

[38] S. Kim and S. J. Karrila, *Microhydrodynamics: Principles and Selected Applications* (Butterworth-Heinemann, Boston, 1991).

[39] J. Happel and H. Brenner, *Low Reynolds Number Hydrodynamics* (Martinus Nijhoff Publishers, The Hague, 1983).

[40] L. Durlofsky, J. F. Brady, and G. Bossis, Dynamic simulation of hydrodynamically interacting particles, J. Fluid Mech. **180**, 21 (1987).

[41] D. Collins, R. J. Hamati, F. Candelier, K. Gustavsson, B. Mehlig, and G. A. Voth, Lord Kelvin's isotropic helicoid, Phys. Rev. Fluids **6**, 074302 (2021).

[42] E. Huseby, J. Gissinger, F. Candelier, N. Pujara, G. Verhille, B. Mehlig, and G. Voth, Helical ribbons: Simple chiral sedimentation, arXiv:2403.18157 [Phys. Rev. Fluids (to be published)].

[43] J. B. Keller and S. I. Rubinow, Slender-body theory for slow viscous flow, J. Fluid Mech. **75**, 705 (1976).

[44] W. Fornari, F. Picano, G. Sardina, and L. Brandt, Reduced particle settling speed in turbulence, J. Fluid Mech. **808**, 153 (2016).

[45] O. Gonzalez, A. B. A. Graf, and J. H. Maddocks, Dynamics of a rigid body in a Stokes fluid, J. Fluid Mech. **519**, 133 (2004).

[46] T. Miara, C. Vaquero-Stainer, D. Pihler-Puzović, M. Heil, and A. Juel, Dynamics of inertialess sedimentation of a rigid U-shaped disk, Commun. Phys. **7**, 47 (2024).

[47] N. Fintzi, L. Gamet, and J.-L. Pierson, Inertial loads on a finite-length cylinder embedded in a steady uniform flow, Phys. Rev. Fluids **8**, 044302 (2023).

[48] A. S. Khair and N. G. Chisholm, A higher-order slender-body theory for axisymmetric flow past a particle at moderate Reynolds number, J. Fluid Mech. **855**, 421 (2018).

[49] F. Auguste, J. Magnaudet, and D. Fabre, Falling styles of disks, J. Fluid Mech. **719**, 388 (2013).

[50] A. Tinklenberg, M. Guala, and F. Coletti, Thin disks falling in air, J. Fluid Mech. **962**, A3 (2023).

[51] A. J. Heymsfield, Laboratory and field observations of the growth of columnar and plate crystals from frozen droplets, J. Atmos. Sci. **30**, 1650 (1973).

[52] A. Tinklenberg, M. Guala, and F. Coletti, Turbulence effect on disk settling dynamics, J. Fluid Mech. **992**, A4 (2024).

[53] E. J. Tozzi, C. T. Scott, D. Vahey, and D. J. Klingenberg, Settling dynamics of asymmetric rigid fibers, Phys. Fluids **23**, 033301 (2011).

[54] J. Gissinger, Dynamique d'une particule de forme quelconque en écoulement de Stokes (unpublished).

Paper III

Preprint, https://arxiv.org/abs/2512.17822

Fluid-inertia torques from particle-shape symmetry

L. Sundberg,[1] F. Candelier,[2] N. Fintzi,[3] G. Voth,[4] J. L. Pierson,[3] K. Gustavsson,[1] and B. Mehlig[1]

[1] *Department of Physics, Gothenburg University, Gothenburg, SE-40530 Sweden*
[2] *Aix-Marseille Univ., CNRS, IUSTI, Marseille, France*
[3] *IFP Energies Nouvelles, Rond-Point de l'echangeur de Solaize, 69360, Solaize, France*
[4] *Department of Physics, Wesleyan University, Middletown, CT 06459, USA*

Numerical simulation of particle motion in fluids at low particle Reynolds numbers is often based on empirical force and torque models obtained by fitting force and torque from *ab-initio* computations for simple particle shapes such as spheres, spheroids, or cylindrical disks and fibres. To do the same for more complex particles shapes, one needs to first know how particle shape constrains the dependence of force and torque on flow velocity, its gradient, and on particle orientation. Here we use symmetry analysis and perturbation theory to determine the form of the hydrodynamic torque on a particle settling in a quiescent fluid at low but non-zero particle Reynolds numbers, for particle shapes with different point-group symmetries. The symmetry conclusions are verified by comparing with explicit calculations for nearly spherical particles.

Keywords: non-spherical particles, particle-shape symmetry, fluid-inertia torques

I. INTRODUCTION

Consider a small particle moving in a fluid. How does particle shape constrain the hydrodynamic force and torque experienced by the particle? This is an important question, because numerical studies of particle motion in complex flows tend to rely on models for force and torque, which allow for efficient computer simulation. A common way to derive such models is to use parameterisations of force and torque obtained by ab-initio simulations [1–7], requiring an *ansatz* for how force and torque depend on the flow velocity and its gradients. Any such ansatz, in turn, depends on particle shape. In Stokes flow, it is known how particle-shape symmetries determine force and torque on small particles in a viscous fluid [8–15]. In many applications, however, the particles are too large or move too rapidly for the Stokes approximation to apply, because it neglects corrections to hydrodynamic force and torque that arise at non-zero particle Reynolds number $\mathrm{Re_p}$. Examples include ice crystals in cold clouds [16–20], and other atmospheric particles [21–25]. Atmospheric particles are frequently modelled using highly symmetric shapes such as spheroids [24], but often atmospheric particles are asymmetric, meaning that certain rotation and reflection symmetries are broken [16, 26].

At small but non-zero particle Reynolds number $\mathrm{Re_p}$, hydrodynamic forces and torques on axisymmetric particles (such as straight fibres and flat disks) settling in a quiescent fluid have been calculated in perturbation theory [27–29], *ab-initio* computer simulations [30], and verified in laboratory experiments [31–33]. This has led to reliable parameterisations of inertial forces and torques for such particles. Brenner and Cox [34] and Cox [35] derived general expressions for the steady force on a particle of arbitrary shape settling in a quiescent fluid, in terms of of tensors and pseudo-tensors of ranks two and three. They also considered how shape symmetries (reflections and $\pi/2$ as well as π rotations) constrain certain contributions to force and torque to vanish. Here we analyse how particle-shape symmetries constrain the general form of the non-zero contributions to the hydrodynamic torque on a particle with arbitrary shape settling in a quiescent fluid, and determine in particular how many parameters are needed to fully parameterise the torque to order $\mathrm{Re_p}$ (the general conclusion is: the more shape symmetries are broken, the more parameters are needed). We verify our symmetry considerations by comparing with explicit calculations for nearly spherical particles [36, 37] with different point-group symmetries, and discuss the implications of our results for steady settling of small asymmetrical particles in a quiescent fluid. Last but not least, we generalise the results of Cox [35] to unsteady motion of small asymmetrical particles at non-zero $\mathrm{Re_p}$, indicating how history effects may change the transient angular dynamics for such particles.

Our calculations are motivated in part by recent experiments, numerical simulations, and calculations that show how breaking of fore-aft symmetry changes the fluid-inertia torque [38–40]. Another motivation comes from recent experimental results for the fluid-inertia torque on curved atmospheric fibres settling in a quiescent fluid [25, 41] which indicate that breaking a reflection symmetry can have a significant effect on how the fluid-inertia torque depends on the orientation of an asymmetric particle (Figure 1) that settles in a quiescent fluid at small but non-zero particle Reynolds numbers.

The remainder of this article is organised as follows. In Section II, we first recall results in the Stokes limit [8, 10]. Then we describe the general form of fluid-inertia corrections to Stokes torque for small but non-zero values of $\mathrm{Re_p}$,

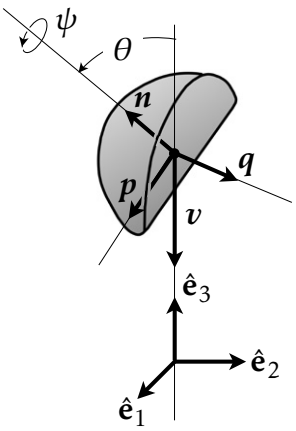

FIG. 1. Particle with C_{2v} shape symmetry moving through a quiescent fluid with velocity $\boldsymbol{v}$. The particle has the shape of a bent disk [14]. It has one C_2-rotation axis $\boldsymbol{n}$ and two reflection symmetries $\boldsymbol{p} \to -\boldsymbol{p}$ and $\boldsymbol{q} \to -\boldsymbol{q}$. Here $\boldsymbol{p}, \boldsymbol{q}, \boldsymbol{n}$ are the basis vectors of a coordinate system that rotates with the particle. The basis vectors of the laboratory coordinate system are denoted by $\hat{\mathbf{e}}_1, \hat{\mathbf{e}}_2, \hat{\mathbf{e}}_3$, and the velocity is $\boldsymbol{v} = -v\hat{\mathbf{e}}_3$. Also shown are the Euler angles θ, ψ that specify particle orientation. We use the $Z_\phi Y_\theta Z_\psi$ convention, as described in the supplemental material of Ref. [25].

for particles of arbitrary shape in a uniform flow. In Section III we derive the form of the fluid-inertia torque for the particle shapes illustrated in Figure 2, to order $\mathrm{Re_p}$. In Section IV we summarise explicit results for nearly spherical yet asymmetrical particles that confirm the symmetry analysis. We discuss our findings in Section V, and relate them to known results for nearly spherical [35], slender [28], and ellipsoidal [42] particles. Section VI contains our conclusions and a brief discussion of open questions, as well as possible applications.

II. BACKGROUND

Consider a particle moving with velocity $\boldsymbol{v}$ and angular velocity $\boldsymbol{\omega}$ in a quiescent fluid (Figure 1). Hydrodynamic force and torque upon a particle in a fluid are determined by integrals of components of the stress tensor over the particle surface $\mathscr{S}$:

$$\boldsymbol{F} = \int_{\mathscr{S}} \varpi \cdot \mathrm{d}\boldsymbol{s} \quad \text{and} \quad \boldsymbol{T} = \int_{\mathscr{S}} \boldsymbol{r} \wedge (\varpi \cdot \mathrm{d}\boldsymbol{s}) \,. \tag{1}$$

Here $\boldsymbol{r}$ is the vector from the chosen reference point to a point on the particle surface (we take the centre-of-mass as the reference). The elements of the stress tensor ϖ are given by $\sigma_{mn} = -p\delta_{mn} + 2\mu S_{mn}$, where μ denotes the viscosity, and S_{mn} are the elements of the strain-rate matrix, the symmetric part of the matrix of disturbance-velocity gradients $\partial w_i/\partial x_j$. In the frame translating with the particle, the disturbance flow $\boldsymbol{w}$ satisfies the Navier-Stokes equations:

$$\mathrm{Re}_p \,\mathrm{Sl}\, \frac{\partial \boldsymbol{w}}{\partial t} - \mathrm{Re}_p \boldsymbol{v} \cdot \boldsymbol{\nabla} \boldsymbol{w} + \mathrm{Re_p}\, \boldsymbol{w} \cdot \boldsymbol{\nabla} \boldsymbol{w} = -\boldsymbol{\nabla} p + \triangle \boldsymbol{w} \,, \quad \boldsymbol{\nabla} \cdot \boldsymbol{w} = 0 \,. \tag{2}$$

We impose no-slip boundary conditions on the particle surface, $\boldsymbol{w} = \boldsymbol{v} + \boldsymbol{\omega} \wedge \boldsymbol{r}$, and require that $\boldsymbol{w} \to \boldsymbol{0}$ as $|\boldsymbol{r}| \to \infty$. Equation (2) was non-dimensionalised using an estimate v_0 of the particle velocity, the particle size a, the time scale τ_0 at which the particle boundary conditions change, the angular-velocity scale $\omega_0 = v_0/a$, and the pressure scale $\mu v_0/a$. Force and torque are non-dimensionalised as

$$\boldsymbol{F}/(\mu a v_0) \to \boldsymbol{F} \quad \text{and} \quad \boldsymbol{T}/(\mu a^2 v_0) \to \boldsymbol{T} \,. \tag{3}$$

From here on, we quote all expressions in non-dimensional variables. The non-dimensional numbers in Eq.(2) are the particle Reynolds number $\mathrm{Re_p}$ and the Strouhal number Sl (a non-dimensional measure of the time scale at which the particle boundary conditions change):

$$\mathrm{Re_p} = a v_0/\nu \,, \quad \mathrm{Sl} = a/(v_0 \tau_0) \,. \tag{4}$$

For $\mathrm{Re_p} = 0$, the left-hand side of Eq. (2) vanishes, and one obtains the steady Stokes approximation to the disturbance flow. Integrating the resulting $\varpi^{(0)}$ over the particle surface as specified in Eqs. (1) yields Stokes force $\boldsymbol{F}^{(0)}$ and torque $\boldsymbol{T}^{(0)}$. Both are linearly related to the particle velocity $\boldsymbol{v}$ and its angular velocity $\boldsymbol{\omega}$. In a quiescent fluid, this relation is written as [43]

$$\begin{bmatrix} \boldsymbol{F}^{(0)} \\ \boldsymbol{T}^{(0)} \end{bmatrix} = - \begin{bmatrix} \mathbb{A} & \mathbb{B}^{\mathsf{T}} \\ \mathbb{B} & \mathbb{C} \end{bmatrix} \begin{bmatrix} \boldsymbol{v} \\ \boldsymbol{\omega} \end{bmatrix} . \tag{5}$$

Here $\mathbb{A}, \mathbb{B}$, and $\mathbb{C}$ are Stokes resistance tensors which depend on particle orientation, on particle shape, but not on particle size a. The superscript T denotes the transpose.

Happel and Brenner [10] analysed how the resistance tensors in Eq. (5) depend on particle shape (for corresponding results in shear flow, see Refs. [8, 11, 44, 45]). Using the fact that the energy dissipation is a scalar, they determined how the Stokes resistance tensors transform under orthogonal coordinate transformations, and concluded the following: if the boundary conditions imposed by the particle upon the flow are invariant under an orthogonal coordinate transformation $\mathbb{O}$, this constrains the elements of the Stokes tensors as follows [10]:

$$A_{ij} = O_{mi} A_{mn} O_{nj} \,, \tag{6a}$$
$$B_{ij} = \det[\mathbb{O}] O_{mi} B_{mn} O_{nj} \,, \tag{6b}$$
$$C_{ij} = O_{mi} C_{mn} O_{nj} \,. \tag{6c}$$

Alternatively, these transformation rules can be derived from the covariance of Eq. (5). Transform $\boldsymbol{F}(\boldsymbol{v}, \boldsymbol{\omega})$ and $\boldsymbol{T}(\boldsymbol{v}, \boldsymbol{\omega})$ as $\boldsymbol{F}' = \mathbb{O}\boldsymbol{F}$ and $\boldsymbol{T}' = \det[\mathbb{O}]\mathbb{O}\boldsymbol{T}$, where $\boldsymbol{F}' = \boldsymbol{F}(\mathbb{O}\boldsymbol{v}, \det[O]\mathbb{O}\boldsymbol{\omega})$ and $\boldsymbol{T}' = \boldsymbol{T}(\mathbb{O}\boldsymbol{v}, \det[O]\mathbb{O}\boldsymbol{\omega})$, and $\mathbb{O}$ is a particle symmetry [11]. Eq. (6b) shows that the translation-rotation coupling tensor $\mathbb{B}$ transforms in a different way from $\mathbb{A}$ and $\mathbb{C}$. The factor $\det[\mathbb{O}]$ ensures that $\mathbb{B} = 0$ for particles with sufficient numbers of reflection symmetries (spheroid, ellipsoid).

For non-zero particle Reynolds number $\mathrm{Re_p}$, the left side of Eq. (2) matters. To first order in $\mathrm{Re_p}$, general expressions for the steady hydrodynamic force and torque ($\mathrm{Sl} = 0$) were derived in Refs. [27, 34, 35]. Lovalenti and Brady [46] derived the first-order force corrections in $\mathrm{Re_p}$ for unsteady flow. Here we obtain the corresponding expressions for the unsteady torque, for particles of arbitrary shapes. In the steady limit, our results simplify to those in Refs. [27, 34, 35].

To compute the effects of weak fluid inertia upon hydrodynamic force and torque, one must account for the fact that the perturbation problem in $\mathrm{Re_p}$ is singular, due to the slow spatial decay of the disturbance flow [47, 48]. We use matched asymptotic expansions [47, 48] to deal with this problem. In this approach, an inner solution valid near the particle is matched to an outer solution valid far from the particle. In the following, it is assumed that $1 \gg \mathrm{Re_p} \gg \mathrm{Re_p Sl}$. Far from the particle, its boundary condition is replaced by a point-source forcing, so that Eq. (2) becomes

$$\mathrm{Re}_p \, \mathrm{Sl} \, \frac{\partial \boldsymbol{w}_{\mathrm{out}}}{\partial t} - \mathrm{Re}_p \, \boldsymbol{v} \cdot \boldsymbol{\nabla} \boldsymbol{w}_{\mathrm{out}} + \mathrm{Re}_p \, \boldsymbol{w}_{\mathrm{out}} \cdot \boldsymbol{\nabla} \boldsymbol{w}_{\mathrm{out}} = -\boldsymbol{\nabla} p_{\mathrm{out}} + \triangle \boldsymbol{w}_{\mathrm{out}} + \boldsymbol{f}^{(0)} \, \delta(\boldsymbol{r}) \,. \tag{7}$$

Here $\boldsymbol{f}^{(0)} = -\boldsymbol{F}^{(0)}$ denotes the force exerted by the particle on the fluid in the Stokes limit. This outer problem can be solved by Fourier transform. The outer solution in Fourier space can be expanded as a series in the small parameter $\sqrt{\mathrm{Re}_p \, \mathrm{Sl}}$, keeping in mind that this expansion must be carried out in the sense of distributions [49, 50]. In configuration space, the corresponding series expansion takes the form

$$\boldsymbol{w}_{\mathrm{out}} = \frac{1}{8\pi} \left(\frac{\mathbb{1}}{r} + \frac{\boldsymbol{r} \otimes \boldsymbol{r}}{r^3} \right) \boldsymbol{f}^{(0)} - \mathrm{Re_p} \boldsymbol{v} \cdot \boldsymbol{\nabla} \left[\frac{3r}{32\pi} \left(\mathbb{1} - \frac{1}{3} \frac{\boldsymbol{r} \otimes \boldsymbol{r}}{r^2} \right) \boldsymbol{f}^{(0)} \right] + \sqrt{\mathrm{Re_p Sl}} \, \boldsymbol{\mathcal{U}} \,. \tag{8}$$

The term $\boldsymbol{\mathcal{U}}$ corresponds to a uniform flow and originates from a singular contribution to the expansion of the outer solution in Fourier space, namely, a term proportional to the Dirac distribution $\delta(\boldsymbol{k})$. This uniform contribution takes the form

$$\sqrt{\mathrm{Re_p Sl}} \boldsymbol{\mathcal{U}} = \sqrt{\mathrm{Re_p Sl}} \int_0^t \mathrm{d}\tau \; \mathbb{K}^{(1)}(t, \tau) \cdot \frac{\mathrm{d} \boldsymbol{f}^{(0)}(\tau)}{\mathrm{d}\tau} + \mathrm{Re_p} \int_0^t \mathrm{d}\tau \; \mathbb{K}^{(2)}(t, \tau) \cdot \boldsymbol{f}^{(0)}(\tau) \,. \tag{9}$$

The kernels $\mathbb{K}^{(1)}(t, \tau)$ and $\mathbb{K}^{(2)}(t, \tau)$ are given in Appendix A. They are equivalent to the kernel involved in the $\mathrm{Re_p}$-correction to the force in unsteady flow, derived by Lovalenti and Brady [46]. The kernels also appear in the work of Redaelli *et al.* [50], except that there the expressions were simplified using the fact that the force $\boldsymbol{f}^{(0)}$ and the velocity $\boldsymbol{v}$ are collinear for a spherical particle.

In the inner region, disturbance velocity and pressure are expanded as

$$\boldsymbol{w}_{\rm in} = \boldsymbol{w}_{\rm in}^{(0)} + \sqrt{\mathrm{Re_pSl}}\,\boldsymbol{w}_{\rm in}^{(1)} + \dots, \qquad p_{\rm in} = p_{\rm in}^{(0)} + \sqrt{\mathrm{Re_pSl}}\,p_{\rm in}^{(1)} + \dots . \tag{10}$$

These inner fields are then matched order by order with their counterparts in the outer solution. The leading-order term $\boldsymbol{w}_{\rm in}^{(0)}$ is the solution of the steady Stokes problem. The term $\mathrm{Re_pSl}\,\partial_t \boldsymbol{w}_{\rm in}^{(0)}$ can be neglected here because it is of higher order in the regular inner expansion. This leading-order solution matches the first term of the outer expansion (8). The next correction $\boldsymbol{w}_{\rm in}^{(1)}$ satisfies the inhomogeneous Stokes problem [50]

$$\sqrt{\frac{\mathrm{Re}_p}{\mathrm{Sl}}}\left[-\boldsymbol{v}\cdot\boldsymbol{\nabla}\boldsymbol{w}_{\rm in}^{(0)} + \boldsymbol{w}_{\rm in}^{(0)}\cdot\boldsymbol{\nabla}\boldsymbol{w}_{\rm in}^{(0)}\right] = -\boldsymbol{\nabla}p^{(1)} + \triangle\boldsymbol{w}_{\rm in}^{(1)} . \tag{11}$$

The function $\boldsymbol{w}_{\rm in}^{(1)}$ satisfies no-slip condition on the particle surface (i.e., $\boldsymbol{w}_{\rm in}^{(1)} = \boldsymbol{0}$) and matches the last two terms of the outer expansion (8). The solution of the inhomogeneous problem Eq. (11) is sought in the form $\boldsymbol{w}_{\rm in}^{(1)} = (\boldsymbol{w}_{\rm p} + \boldsymbol{\mathcal{U}}) + \boldsymbol{w}_h$, that is as the sum of a particular (forced) solution $\boldsymbol{w}_{\rm p} + \boldsymbol{\mathcal{U}}$, and a homogeneous solution $\boldsymbol{w}_h$. Here, $\boldsymbol{w}_{\rm p}$ satisfies (11), while $\boldsymbol{w}_h$ satisfies the Stokes equations together with the boundary condition $\boldsymbol{w}_h = -(\boldsymbol{w}_{\rm p} + \boldsymbol{\mathcal{U}})$ on the particle surface, ensuring that $\boldsymbol{w}_{\rm in}^{(1)}$ fulfills the no-slip condition. The particular solution $\boldsymbol{w}_{\rm p}$ depends quadratically on $\boldsymbol{v}$ and $\boldsymbol{\omega}$, due to the quadratic convective term in (11). Similarly, the component of $\boldsymbol{w}_h$ linked to $\boldsymbol{w}_{\rm p}$ inherits this quadratic dependence because of the boundary condition imposed on the homogeneous part. Consequently, the total force and torque at order $\mathrm{Re_p}$ are

$$\boldsymbol{F} = \boldsymbol{F}^{(0)} + \mathrm{Re_p}\,\boldsymbol{F}_{\rm reg}^{(1)} + \sqrt{\mathrm{Re_pSl}}\,\boldsymbol{F}_{\rm sing}^{(1)}, \qquad \boldsymbol{T} = \boldsymbol{T}^{(0)} + \mathrm{Re_p}\,\boldsymbol{T}_{\rm reg}^{(1)} + \sqrt{\mathrm{Re_pSl}}\,\boldsymbol{T}_{\rm sing}^{(1)}, \tag{12}$$

where the so-called 'singular' contributions come from the singular part of the outer expansion,

$$\boldsymbol{F}_{\rm sing}^{(1)} = \mathbb{A}\cdot\boldsymbol{\mathcal{U}}, \quad \boldsymbol{T}_{\rm sing}^{(1)} = \mathbb{B}\cdot\boldsymbol{\mathcal{U}}, \tag{13}$$

and the 'regular' contributions take the form

$$\boldsymbol{F}_{\rm reg}^{(1)} = \mathbb{M}^{(vv)} : \boldsymbol{v}\otimes\boldsymbol{v} + \mathbb{M}^{(\omega\omega)} : \boldsymbol{\omega}\otimes\boldsymbol{\omega} + \mathbb{M}^{(v\omega)} : \boldsymbol{v}\otimes\boldsymbol{\omega}, \tag{14a}$$

$$\boldsymbol{T}_{\rm reg}^{(1)} = \mathbb{N}^{(vv)} : \boldsymbol{v}\otimes\boldsymbol{v} + \mathbb{N}^{(\omega\omega)} : \boldsymbol{\omega}\otimes\boldsymbol{\omega} + \mathbb{N}^{(v\omega)} : \boldsymbol{v}\otimes\boldsymbol{\omega}. \tag{14b}$$

Here the colon denotes double contraction (the elements of $\mathbb{M} : \mathbb{S}$ with the second order tensor $\mathbb{S}$ are $\sum_{jk} M_{ijk}S_{jk}$). We remark that terms of the form $\mathbb{M}^{(\omega v)} : \boldsymbol{\omega}\otimes\boldsymbol{v}$ and $\mathbb{N}^{(\omega v)} : \boldsymbol{\omega}\otimes\boldsymbol{v}$ can be omitted since they have the same structure and transformation rules as $\mathbb{M}^{(v\omega)} : \boldsymbol{v}\otimes\boldsymbol{\omega}$ and $\mathbb{N}^{(v\omega)} : \boldsymbol{v}\otimes\boldsymbol{\omega}$. Because the contributions (14) are determined by the inner solution, they are valid instantaneously, also for non-zero angular velocities. Such quadratic terms were obtained in Refs. [27, 34, 35] using a reformulation of the reciprocal theorem.

In the steady limit, Eq. (9) simplifies. In order to obtain a steady disturbance flow, $\boldsymbol{v}$, $\boldsymbol{\omega}$, and $f^{(0)}$ must be independent of time (or at least vary very slowly). Equation (5) relates these three vectors: $\boldsymbol{f}^{(0)} = -\boldsymbol{F}^{(0)} = \mathbb{A}\boldsymbol{v} + \mathbb{B}^{\mathsf{T}}\boldsymbol{\omega}$. Accounting for a possible time dependence of $\mathbb{A}$, one finds:

$$\frac{\mathrm{d}\boldsymbol{f}^{(0)}}{\mathrm{d}t} = \boldsymbol{\omega}\wedge\boldsymbol{f}^{(0)} - \mathbb{A}\cdot(\boldsymbol{\omega}\wedge\boldsymbol{v}) + \mathbb{A}\cdot\frac{\mathrm{d}\boldsymbol{v}}{\mathrm{d}t} + \mathbb{B}^{\mathsf{T}}\cdot\frac{\mathrm{d}\boldsymbol{\omega}}{\mathrm{d}t} . \tag{15}$$

We conclude that it is not possible in general to simultaneously satisfy $\frac{\mathrm{d}}{\mathrm{d}t}\boldsymbol{v} = \frac{\mathrm{d}}{\mathrm{d}t}\boldsymbol{\omega} = \frac{\mathrm{d}}{\mathrm{d}t}\boldsymbol{f}^{(0)} = \boldsymbol{0}$, at least when $\mathbb{B} \neq \mathbb{0}$. An exception to this rule is the following example: an axisymmetric pear-shaped particle that rotates around its symmetry axis with constant angular velocity $\boldsymbol{\omega}$, so that $\boldsymbol{f}^{(0)}$, $\boldsymbol{\omega}$, and $\boldsymbol{v}$ are collinear.

A second example is a particle moving at constant velocity with zero angular velocity. In this case, Eq. (15) allows for both $\boldsymbol{f}^{(0)}$ and $\boldsymbol{v}$ to be constant. When $\boldsymbol{f}^{(0)}$ varies slowly (so that its time scale of variation is much larger than a^2/ν, or equivalently $\mathrm{Sl} \to 0$), Eq. (9) simplifies. The first integral on the right-hand side of Eq. (9) vanishes, and $\boldsymbol{f}^{(0)}$ can be pulled out from the second integral. Upon performing the remaining integral, one obtains

$$\boldsymbol{\mathcal{U}} = -\sqrt{\frac{\mathrm{Re_p}}{\mathrm{Sl}}}\,\frac{3v}{32\pi}\left(\mathbb{I} - \frac{1}{3}\,\hat{\boldsymbol{v}}\otimes\hat{\boldsymbol{v}}\right)\cdot\boldsymbol{f}^{(0)} , \tag{16}$$

where $\hat{\boldsymbol{v}}$ denotes the unit vector in the direction of $\boldsymbol{v}$, and $\mathbb{I}$ is the identity matrix. Since $\boldsymbol{\mathcal{U}}$ corresponds to a uniform flow at infinity, the singular contributions simplify to

$$\boldsymbol{F}_{\rm sing}^{(1)} = -\sqrt{\frac{\mathrm{Re_p}}{\mathrm{Sl}}}\,\frac{3v}{32\pi}\mathbb{A}\cdot\left[\mathbb{A}\cdot\boldsymbol{v} - \tfrac{1}{3}(\hat{\boldsymbol{v}}\otimes\hat{\boldsymbol{v}})\cdot\mathbb{A}\cdot\boldsymbol{v}\right], \quad \boldsymbol{T}_{\rm sing}^{(1)} = -\sqrt{\frac{\mathrm{Re_p}}{\mathrm{Sl}}}\,\frac{3v}{32\pi}\mathbb{B}\cdot\left[\mathbb{A}\cdot\boldsymbol{v} - \tfrac{1}{3}(\hat{\boldsymbol{v}}\otimes\hat{\boldsymbol{v}})\cdot\mathbb{A}\cdot\boldsymbol{v}\right]. \tag{17}$$

These contributions to the steady force and torque approximation were first obtained in Refs. [27, 34, 35] using the reformulation of the reciprocal theorem mentioned above. Cox [35] includes terms with $\boldsymbol{\omega} \neq 0$ in his $\mathrm{Re_p}$-contributions for force and torque. As pointed out above, this is consistent in certain special cases, but not in general.

Asymptotic matching, employed here, offers additional insights. First, it gives a clear interpretation of where the different terms to the fluid-inertia forces and torques come from. The contributions (17) originate from the far field and may contain transient, time-dependent terms, while the terms (14) are instantaneous contributions deriving from the inner solution. Second, asymptotic matching allows to compute the transient, time-dependent terms (9), so-called history forces and torques that affect the transient dynamics of the particle. Third, the derivation of Eqs. (17) from the unsteady $\mathcal{U}$ highlights that Eqs. (17) assume that the particle velocity is steady. Upon a change of centre of reference at non-zero $\boldsymbol{\omega}$ this assumption may fail. Therefore one needs to go back to (9) and (13) in order to see that the particle dynamics does not depend on the arbitrary choice of the centre-of-reference.

Now consider how particle-shape symmetries constrain force and torque to order $\mathrm{Re_p}$. The tensors $\mathbb{A}$ and $\mathbb{B}$ in Eq. (13) are defined in the Stokes limit, and their components must obey Eqs. (6). This in turn implies the same for $\boldsymbol{F}^{(1)}_{\mathrm{reg}}$ and $\boldsymbol{T}^{(1)}_{\mathrm{reg}}$, which constrains the components of the tensors $\mathbb{M}$ and $\mathbb{N}$ as follows:

$$N^{(vv)}_{ijk} = \det[\mathbb{O}]\, O_{mi} N^{(vv)}_{mnl} O_{nj} O_{lk} \quad \text{and} \quad M^{(vv)}_{ijk} = O_{mi} M^{(vv)}_{mnl} O_{nj} O_{lk}\,, \tag{18a}$$

$$N^{(\omega\omega)}_{ijk} = \det[\mathbb{O}]\, O_{mi} N^{(\omega\omega)}_{mnl} O_{nj} O_{lk} \quad \text{and} \quad M^{(\omega\omega)}_{ijk} = O_{mi} M^{(\omega\omega)}_{mnl} O_{nj} O_{lk}\,, \tag{18b}$$

$$N^{(v\omega)}_{ijk} = O_{mi} N^{(v\omega)}_{mnl} O_{nj} O_{lk}\,, \qquad \text{and} \quad M^{(v\omega)}_{ijk} = \det[\mathbb{O}]\, O_{mi} M^{(v\omega)}_{mnl} O_{nj} O_{lk}\,. \tag{18c}$$

Note that the rank-3 tensors $\mathbb{M}$ and $\mathbb{N}$ arise in the first order of a systematic expansion in $\mathrm{Re_p}$. So their elements are determined by Stokes solutions, but the tensors depend on particle shape in a more complex way than solely through the rank-two Stokes resistance tensors $\mathbb{A}$, $\mathbb{B}$, and $\mathbb{C}$. Equation (18) implies that $\mathbb{N}^{(vv)}$, $\mathbb{N}^{(\omega\omega)}$, and $\mathbb{M}^{(v\omega)}$ transform as the Stokes tensor $\mathbb{H}$ that couples $\boldsymbol{T}^{(0)}$ to the strain $\mathbb{S}$ [8, 11, 44, 45]. Likewise, $\mathbb{M}^{(vv)}$, $\mathbb{M}^{(\omega\omega)}$, and $\mathbb{N}^{(v\omega)}$ have the same transformation properties.

Brenner and Cox [34] and Cox [35] determined under which circumstances the components of the vectors $\mathbb{M}^{(vv)} : \boldsymbol{v}\otimes\boldsymbol{v}$ and $\mathbb{N}^{(vv)} : \boldsymbol{v} \otimes \boldsymbol{v}$ (and the corresponding contributions for the other rank-3 tensors) vanish, by considering $\frac{\pi}{2}$- and π-rotations as well as reflections. In general, these contributions do not vanish. Here we use Eqs. (6), (14), (17), and (18) to derive constraints on the non-zero components of the fluid-inertia torque for asymmetric particles, obtained from symmetric shapes by breaking rotation and/or reflection symmetries. This allows to understand similarities and differences in the dynamics of asymmetric particles settling in a quiescent fluid [14, 25, 38, 39, 51].

III. SYMMETRY CONSTRAINTS ON TORQUE

Figure 2 illustrates particles with different point-group symmetries. The first row shows particles with reflection and discrete rotation symmetries, such as cuboid, prism, and cube. In the limit where the rotation symmetry becomes continuous, these generalize to ellipsoid, spheroid, and sphere. The second row shows shapes with broken reflection symmetries, namely broken fore-aft symmetry (point-group symmetry C_{2v}), and the isotropic helicoid [52] (point-group symmetry O).

A. Prismatic symmetry D_{2h}

The cuboid shown in Figure 2(**a**) has three reflection symmetries in the planes orthogonal to the three principal axes (point group symmetry D_{2h}). The three orthogonal reflections constrain the three Stokes resistance tensors to be $\mathbb{A} = \mathrm{diag}[A_{pp}, A_{qq}, A_{nn}]$, $\mathbb{C} = \mathrm{diag}[C_{pp}, C_{qq}, C_{nn}]$, and $\mathbb{B} = 0$. Further, the reflections constrain the inertial rank-3 tensors to $\mathbb{N}^{(v\omega)} = 0$, and

$$\mathbb{N}^{(vv)}_{p::} = \begin{bmatrix} 0 & 0 & 0 \\ 0 & 0 & N^{(vv)}_{pqn} \\ 0 & N^{(vv)}_{pnq} & 0 \end{bmatrix}, \quad \mathbb{N}^{(vv)}_{q::} = \begin{bmatrix} 0 & 0 & N^{(vv)}_{qpn} \\ 0 & 0 & 0 \\ N^{(vv)}_{qnp} & 0 & 0 \end{bmatrix}, \quad \mathbb{N}^{(vv)}_{n::} = \begin{bmatrix} 0 & N^{(vv)}_{npq} & 0 \\ N^{(vv)}_{nqp} & 0 & 0 \\ 0 & 0 & 0 \end{bmatrix}. \tag{19}$$

It follows from the discussion in Section II that the tensors $\mathbb{N}^{(\omega\omega)}$ and $\mathbb{M}^{(v\omega)}$ have the same form as $\mathbb{N}^{(vv)}$, but with independent parameters. The tensors $\mathbb{M}^{(vv)}$ and $\mathbb{M}^{(\omega\omega)}$ vanish. The above constraints yield the following expressions

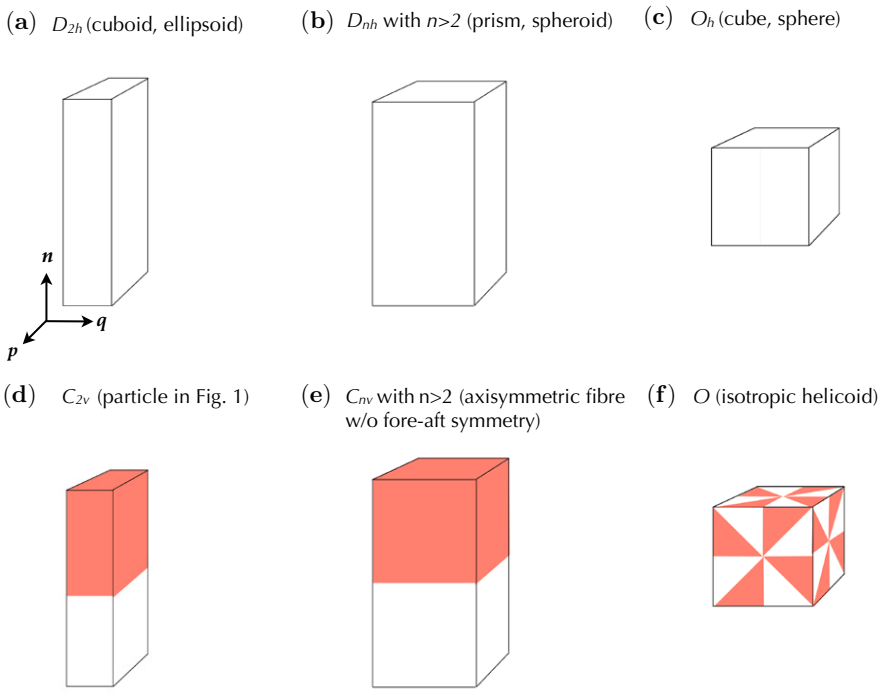

FIG. 2. Particle-shape symmetries considered in Section III (see that Section for the names of the six point groups). In panel (**a**), the orientation of the body-centered coordinate system $\boldsymbol{p}$, $\boldsymbol{q}$, $\boldsymbol{n}$ is shown (same for other panels). Point-group symmetries represented as in Figs. 7.2 and 7.3 in Ref. [53].

for the $\mathrm{Re_p}$-corrections to the torque

$$T_p^{(1)} = 2N_{p(nq)}^{(vv)} v_n v_q + 2N_{p(nq)}^{(\omega\omega)} \omega_n \omega_q \,, \tag{20a}$$

$$T_q^{(1)} = 2N_{q(pn)}^{(vv)} v_p v_n + 2N_{q(pn)}^{(\omega\omega)} \omega_p \omega_n \,, \tag{20b}$$

$$T_n^{(1)} = 2N_{n(pq)}^{(vv)} v_p v_q + 2N_{n(pq)}^{(\omega\omega)} \omega_p \omega_q \tag{20c}$$

in the basis $\boldsymbol{p}, \boldsymbol{q}, \boldsymbol{n}$ (Figure 2). Here, $N_{p(nq)}^{(vv)} = \frac{1}{2}(N_{pnq}^{(vv)} + N_{pqn}^{(vv)}), \ldots$ are symmetrised coupling-coefficients. Since $\mathbb{B} = 0$, the singular contributions to the inertial torque, Eq. (17), vanish. Thus, only the instantaneous terms from the inner solution contribute, meaning that Eqs. (20) are valid in the unsteady case, in particular for non-zero values of $\boldsymbol{\omega}$.

B. Prismatic symmetry (D_{nh} for $n > 2$)

Straight columns with a regular n-gon cross sections with $n > 2$ (*prismatic symmetry* D_{nh} with $n > 2$) possess discrete n-fold rotational symmetry (C_n) about the $\boldsymbol{n}$-axis. The case $n = 4$ is illustrated in Fig. 2(**b**). Another example is cloud-ice crystals, often possessing hexagonal ($n = 6$) cross sections [54, 55]. Imposing C_n-rotation symmetry with $n > 2$ around $\boldsymbol{n}$ imposes additional constraints on the non-zero coefficients in Eq. (20) compared with $n = 2$:

$$A_{pp} = A_{qq} = A_\perp, \quad A_{nn} = A_\parallel, \quad C_{pp} = C_{qq} = C_\perp, \quad C_{nn} = C_\parallel, \tag{21a}$$

$$N_{pqn}^{(vv)} = -N_{qpn}^{(vv)} = N_1^{(vv)}, N_{pnq}^{(vv)} = -N_{pnq}^{(vv)} = N_2^{(vv)}, N_{npq}^{(vv)} = -N_{nqp}^{(vv)} = N_3^{(vv)} . \tag{21b}$$

The elements of $\mathbb{N}^{(\omega\omega)}$ are constrained in the same way. This leaves six undetermined parameters in the $\mathbb{N}$-tensors. The $\mathrm{Re_p}$-contributions to the torque simplify to:

$$T_p^{(1)} = (N_1^{(vv)} + N_2^{(vv)})v_q v_n + (N_1^{(\omega\omega)} + N_2^{(\omega\omega)})\omega_q\omega_n\,, \tag{22a}$$

$$T_q^{(1)} = -(N_1^{(vv)} + N_2^{(vv)})v_p v_n - (N_1^{(\omega\omega)} + N_2^{(\omega\omega)})\omega_p\omega_n\,, \tag{22b}$$

$$T_n^{(1)} = 0 \tag{22c}$$

in the basis $\boldsymbol{p}, \boldsymbol{q}, \boldsymbol{n}$ (Figure 2). Similar to Eqs. (20), these expressions are valid in the unsteady case. The rotational symmetry around $\boldsymbol{n}$ causes the torque T_n to vanish. This follows because $\mathbb{N}_{n::}^{(vv)}$ and $\mathbb{N}_{n::}^{(\omega\omega)}$ are anti-symmetric, and contracted with the symmetric $\boldsymbol{v}\otimes\boldsymbol{v}$ and $\boldsymbol{\omega}\otimes\boldsymbol{\omega}$, respectively. If $\boldsymbol{\omega} = 0$, the torque is orthogonal to $\boldsymbol{n}$, and proportional to the velocity component v_n: $\boldsymbol{T} = (N_1^{(vv)} + N_2^{(vv)})(\boldsymbol{v}\cdot\boldsymbol{n})(\boldsymbol{v}\wedge\boldsymbol{n})$, consistent with Refs. [28–30].

C. Full octahedral symmetry (O_h)

Now consider particles with *full octahedral symmetry* O_h [(Figure 2(**c**)]. An example is the cube, but also the sphere with continuous rotation symmetry. For both examples, rotation and reflection symmetries further constrain Eqs. (21). The Stokes tensors $\mathbb{A}$ and $\mathbb{C}$ become proportional to the identity matrix, and the tensors $\mathbb{N}^{(vv)}$ and $\mathbb{N}^{(\omega\omega)}$ become proportional to the anti-symmetric Levi-Civita tensor $\boldsymbol{\epsilon}$: $A_\perp = A_\parallel = A$, $C_\perp = C_\parallel = C$, $\mathbb{N}^{(vv)} = N^{(vv)}\boldsymbol{\epsilon}$, and $\mathbb{N}^{(\omega\omega)} = N^{(\omega\omega)}\boldsymbol{\epsilon}$. The latter conditions cause the torque (22) to vanish.

As discussed in Section II, $\mathbb{M}^{(v\omega)}$ is constrained in the same way as $\mathbb{N}^{(vv)}$, so $\mathbb{M}^{(v\omega)} = M^{(v\omega)}\boldsymbol{\epsilon}$, yielding a contribution proportional to $\boldsymbol{v}\wedge\boldsymbol{\omega}$, the Rubinow-Keller lift force for a spherical particle (Eq. (71) in Ref. [56]), and its generalisation to particles with O_h symmetry. See Appendix B for details.

Using that $\mathbb{A} = A\mathbb{I}$ and that $\hat{\boldsymbol{v}}$ is a unit vector, the singular contribution to the force (17) is isotropic, proportional to $\frac{2}{3}A^2v^2\hat{\boldsymbol{v}}$ [34, 35]. The theory to linear order in $\mathrm{Re_p}$ is isotropic, but does not rule out the existence of anisotropic terms at higher orders in in the Reynolds number. It is instructive to compare this conclusion with a more general symmetry argument that assumes only that force and torque to order $\mathrm{Re_p}$ are third-order polynomials in the components of $\hat{\boldsymbol{v}}$ with coefficients that are constrained by symmetry. Requiring invariance of force and torque under particle-shape symmetry transformations yields results consistent with the above conclusions, but they constrain force and torque less because the relation between force and torque encoded in Eq. (13) is not accounted for.

D. Orthorhombic pyramidal symmetry (C_{2v})

Figure 2(**d**) shows a particle that has the same symmetry as D_{2h}, but with broken reflection symmetry in the $\boldsymbol{n}$-direction (orthorhombic pyramidal symmetry C_{2v}). Examples of such particles are curved planar fibres with constant radius of curvature [25], and symmetrically bent disks [14] (Fig. 1). The tensors $\mathbb{A}$, $\mathbb{C}$, $\mathbb{N}^{(vv)}$, and $\mathbb{N}^{(\omega\omega)}$ of particles with C_{2v} symmetry have the same form as for particles with D_{2h} symmetry (discussed above). But the broken reflection symmetry results in a non-zero Stokes translation-rotation coupling:

$$\mathbb{B} = \begin{bmatrix} 0 & B_{pq} & 0 \\ B_{qp} & 0 & 0 \\ 0 & 0 & 0 \end{bmatrix}, \tag{23}$$

as well as a non-zero $\mathbb{N}^{(v\omega)}$:

$$\mathbb{N}_{p::}^{(v\omega)} = \begin{bmatrix} 0 & 0 & N_{ppn}^{(v\omega)} \\ 0 & 0 & 0 \\ N_{pnp}^{(v\omega)} & 0 & 0 \end{bmatrix} \quad \mathbb{N}_{q::}^{(v\omega)} = \begin{bmatrix} 0 & 0 & 0 \\ 0 & 0 & N_{qqn}^{(v\omega)} \\ 0 & N_{qnq}^{(v\omega)} & 0 \end{bmatrix}, \quad \mathbb{N}_{n::}^{(v\omega)} = \begin{bmatrix} N_{npp}^{(v\omega)} & 0 & 0 \\ 0 & N_{nqq}^{(v\omega)} & 0 \\ 0 & 0 & N_{nnn}^{(v\omega)} \end{bmatrix}. \tag{24}$$

Now consider the corresponding expression for the fluid-inertia correction to the hydrodynamic torque. Since the general symmetry analysis of the unsteady contribution $\mathcal{U}$ is complicated, we only consider the steady limit, which requires $\boldsymbol{\omega} = 0$, as discussed in the previous Section. For the steady $\mathrm{Re_p}$-contributions to the torque we find:

$$T_p^{(1)} = -\tfrac{1}{32\pi}vB_{pq}[3A_{qq} - (A_{pp}\hat{v}_p^2 + A_{qq}\hat{v}_q^2 + A_{nn}\hat{v}_n^2)]v_q + 2N_{p(nq)}^{(vv)}v_n v_q\,, \tag{25a}$$

$$T_q^{(1)} = -\tfrac{1}{32\pi}vB_{qp}[3A_{pp} - (A_{pp}\hat{v}_p^2 + A_{qq}\hat{v}_q^2 + A_{nn}\hat{v}_n^2)]v_p + 2N_{q(np)}^{(vv)}v_n v_p\,, \tag{25b}$$

$$T_n^{(1)} = 2N_{n(qp)}^{(vv)}v_q v_p \tag{25c}$$

in the basis $\boldsymbol{p}, \boldsymbol{q}, \boldsymbol{n}$ (Figure 2). Comparing with Eq. (20) for the ellipsoid, we see that the form of the quadratic terms is unaffected by the reflection symmetry for $\boldsymbol{\omega} = 0$. Broken reflection symmetry still changes the fluid-inertia torque, due to the non-zero translation-rotation coupling $\mathbb{B}$ in the Stokes limit, yielding a non-zero singular contribution from Eq. (17).

E. Pyramidal symmetry (C_{nv} with $n > 2$)

Particles with n-fold axisymmetry without fore-aft symmetry have C_{nv}-symmetry, $n > 2$ [Figure 2(**e**)]. Other examples invariant under C_{nv} are dumbbells with spheres of different radii [38, 57], and straight fibres with continuous rotation symmetry but varying cross section [39]. For particles invariant under this symmetry, we find the following non-zero coefficients

$$A_{pp} = A_{qq} = A_\perp, \quad A_{nn} = A_\parallel, \quad C_{pp} = C_{qq} = C_\perp, \quad C_{nn} = C_\parallel, \quad B_{pq} = -B_{qp} = B. \tag{26a}$$

as well as

$$N^{(v\omega)}_{ppn} = N^{(v\omega)}_{qqn} = N^{(v\omega)}_1, \quad N^{(v\omega)}_{pnp} = N^{(v\omega)}_{qnq} = N^{(v\omega)}_2, \quad N^{(v\omega)}_{npp} = N^{(v\omega)}_{nqq} = N^{(v\omega)}_3, \quad N^{(v\omega)}_{nnn} = N^{(v\omega)}_4, \tag{26b}$$

$$N^{(vv)}_{pqn} = -N^{(vv)}_{qpn} = N^{(vv)}_1, \quad N^{(vv)}_{pnq} = -N^{(vv)}_{pmq} = N^{(vv)}_2, \quad N^{(vv)}_{npq} = -N^{(vv)}_{nqp} = N^{(vv)}_3. \tag{26c}$$

The tensor $\mathbb{N}^{(\omega\omega)}$ has the same form as $\mathbb{N}^{(vv)}$. The steady $\mathrm{Re_p}$-contributions to the torque components are

$$T^{(1)}_p = \tfrac{-1}{32\pi} v B[A_\perp(3 - (\hat{v}_p^2 + \hat{v}_q^2)) - A_\parallel \hat{v}_n^2] v_q + (N^{(vv)}_1 + N^{(vv)}_2) v_q v_n \,, \tag{27a}$$

$$T^{(1)}_q = \tfrac{1}{32\pi} v B[A_\perp(3 - (\hat{v}_p^2 + \hat{v}_q^2)) - A_\parallel \hat{v}_n^2] v_p - (N^{(vv)}_1 + N^{(vv)}_2) v_p v_n \,, \tag{27b}$$

$$T^{(1)}_n = 0 \,. \tag{27c}$$

Comparing with Eq. (22), we see that breaking of fore-aft symmetry introduces additional terms in the steady $\mathrm{Re_p}$-corrections to the torque, depending on the translation-rotation coupling B in the Stokes limit. The form of the quadratic terms in the steady torque does not change, as was mentioned for the fibres. The steady fluid-inertia torque (27) can be written as [30]

$$\boldsymbol{T}^{(1)} = v^2 g(\hat{v}_n)(\hat{\boldsymbol{v}} \wedge \hat{\boldsymbol{n}}) \,, \tag{28}$$

with $g(\hat{v}_n) = -B[2A_\perp + (A_\perp - A_\parallel)\hat{v}_n^2]/(32\pi) + (N^{(vv)}_1 + N^{(vv)}_2)\hat{v}_n$. The general form of Eq. (28) is consistent with Eq. (2.11) in Roy *et al.* [39] who considered particles without fore-aft symmetry made out of non-slender rods with changing cross section or inhomogeneous mass distribution. However, Eq. (2.11) in Ref. [39] implies that g is proportional to $\hat{v}_n$. This is explained by the fact that Eq. (2.11) was derived in the slender-body approximation including terms up to $1/(\log\kappa)^2$, whereas the first two terms in the above expression for g are at least of order $1/(\log\kappa)^3$ (see Section V). Candelier and Mehlig [38] computed the torque on an asymmetric dumbbell settling in a quiescent fluid. In this case, g is a linear function of $\hat{v}_n$. We do not know why the coefficient of the quadratic term vanishes. It may be a consequence of the fact that the authors considered the special case of a slender and weakly asymmetric dumbbell, constraining the coefficients in Eq. (27) further.

F. Chiral octahedral symmetry O

Lord Kelvin's isotropic helicoid [52] is a particle which has *chiral octahedral symmetry* O. That is, it has the same rotational symmetries as O_h but no reflection symmetries [Figure 2(**f**)]. The rotation symmetries constrains $\mathbb{A}, \mathbb{B}$ and $\mathbb{C}$ to be isotropic: $\mathbb{A} = A\mathbb{I}$, $\mathbb{B} = B\mathbb{I}, \mathbb{C} = C\mathbb{I}$. It thus has the same structure as a cube/sphere but with an isotropic translation-rotation coupling [13, 52]. Here we conclude in addition that all $\mathbb{N}$-tensors are proportional to $\boldsymbol{\epsilon}$. For the sphere we found $\mathbb{N}^{(v\omega)} = 0$, but here $\mathbb{N}^{(v\omega)} = \boldsymbol{\epsilon}$ because there are no reflection symmetries, so $\det[\mathbb{O}] \equiv 1$. As a consequence, the steady translation-rotation coupling remains isotropic to order $\mathrm{Re_p}$,

$$\boldsymbol{T}^{(1)} = -\frac{3v}{32\pi} B\,(\mathbb{I} - \tfrac{1}{3}\hat{\boldsymbol{v}} \otimes \hat{\boldsymbol{v}}) \cdot (A\boldsymbol{v} + B\boldsymbol{\omega}) + N^{(v\omega)}\, \boldsymbol{v} \wedge \boldsymbol{\omega} \,. \tag{29}$$

Note that $\boldsymbol{f}^{(0)}$ is constant for an isotropic helicoid that translates with constant velocity $\boldsymbol{v}$ and rotates with constant angular velocity $\boldsymbol{\omega}$, regardless of how this vectors align. Therefore we quoted the steady result for non-zero frequency above. The last term on the right-hand side is the analogue of the Rubinow-Keller lift force on a translating and rotating sphere.

TABLE I. Summary of geometric constraints and contributions to the force and torque for different particle symmetries. The form of the tensor $\mathbb{C}$ is the same as $\mathbb{A}$ (with independent elements). The forms of $\mathbb{M}^{(vv)}$ and $\mathbb{M}^{(\omega\omega)}$ are the same as the form of $\mathbb{N}^{(v\omega)}$, and the forms of $\mathbb{M}^{(v\omega)}$ and $\mathbb{N}^{(\omega\omega)}$ are the same as that of $\mathbb{N}^{(vv)}$.

Symmetry	Constraints on $\mathbb{A}, \mathbb{B}, \mathbb{C}, \mathbb{N}$	Examples (nearly spherical particles)
Full octahedral (O_h)	$\mathbb{A} = A\mathbb{1}$, $\mathbb{B} = \mathbb{0}$, $\mathbb{N}^{(v\omega)} = \mathbb{0}$, $\mathbb{N}^{(vv)} = N^{(vv)}\boldsymbol{\epsilon}$ ($\boldsymbol{\epsilon} \equiv$ Levi-Civita tensor).	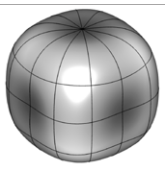 $r = 1 - \frac{1}{2}\varepsilon(\sin^4\vartheta\cos^4\varphi + \sin^4\vartheta\sin^4\varphi + \cos^4\vartheta)$ $(\varepsilon = 0.5)$
Prismatic (D_{2h})	$\mathbb{A} = \mathrm{diag}[A_{pp}, A_{qq}, A_{nn}]$, $\mathbb{B} = \mathbb{0}$, $\mathbb{N}^{(v\omega)} = \mathbb{0}$, $\mathbb{N}^{(vv)} = N^{(vv)}_{pqn}\,\boldsymbol{p}\otimes\boldsymbol{q}\otimes\boldsymbol{n} + N^{(vv)}_{pnq}\,\boldsymbol{p}\otimes\boldsymbol{n}\otimes\boldsymbol{q}$ $+N^{(vv)}_{qpn}\,\boldsymbol{q}\otimes\boldsymbol{p}\otimes\boldsymbol{n} + N^{(vv)}_{qnp}\,\boldsymbol{q}\otimes\boldsymbol{n}\otimes\boldsymbol{p}$ $+N^{(vv)}_{npq}\,\boldsymbol{n}\otimes\boldsymbol{p}\otimes\boldsymbol{q} + N^{(vv)}_{nqp}\,\boldsymbol{n}\otimes\boldsymbol{q}\otimes\boldsymbol{p}$.	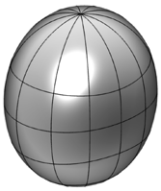 $r = 1 - \varepsilon\sin^2\vartheta(\alpha - \alpha\sin^2\varphi + \sin^2\varphi)$ $(\varepsilon = 0.3\,, \alpha = 0.5)$
Pyramidal ($C_{\infty v}$)	$\mathbb{A} = \mathrm{diag}[A_\perp, A_\perp, A_\parallel]$, $\mathbb{B} = B\,(\boldsymbol{p}\otimes\boldsymbol{q} - \boldsymbol{q}\otimes\boldsymbol{p})$, $\mathbb{N}^{(v\omega)} = N^{(v\omega)}_1(\boldsymbol{p}\otimes\boldsymbol{p}\otimes\boldsymbol{n} + \boldsymbol{q}\otimes\boldsymbol{q}\otimes\boldsymbol{n})$, $+N^{(v\omega)}_2(\boldsymbol{p}\otimes\boldsymbol{n}\otimes\boldsymbol{p} + \boldsymbol{q}\otimes\boldsymbol{n}\otimes\boldsymbol{q})$ $+N^{(v\omega)}_3(\boldsymbol{n}\otimes\boldsymbol{p}\otimes\boldsymbol{p} + \boldsymbol{n}\otimes\boldsymbol{q}\otimes\boldsymbol{q})$ $+N^{(v\omega)}_4(\boldsymbol{n}\otimes\boldsymbol{n}\otimes\boldsymbol{n})$, $\mathbb{N}^{(vv)} = N^{(vv)}_1(\boldsymbol{p}\otimes\boldsymbol{q}\otimes\boldsymbol{n} - \boldsymbol{q}\otimes\boldsymbol{p}\otimes\boldsymbol{n})$ $+N^{(vv)}_2(\boldsymbol{p}\otimes\boldsymbol{n}\otimes\boldsymbol{q} - \boldsymbol{q}\otimes\boldsymbol{n}\otimes\boldsymbol{p})$ $+N^{(vv)}_3(\boldsymbol{n}\otimes\boldsymbol{p}\otimes\boldsymbol{q} - \boldsymbol{n}\otimes\boldsymbol{q}\otimes\boldsymbol{p})$.	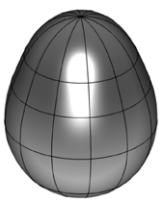 $r = 1 - \varepsilon(\sin^2\vartheta + \frac{\gamma}{2}\cos\vartheta)$ $(\varepsilon = 0.3\,, \gamma = 1.5)$
Orthorhombic pyramidal (C_{2v})	$\mathbb{A} = \mathrm{diag}[A_{pp}, A_{qq}, A_{nn}]$, $\mathbb{B} = B_{pq}\boldsymbol{p}\otimes\boldsymbol{q} + B_{qp}\boldsymbol{q}\otimes\boldsymbol{p}$, $\mathbb{N}^{(v\omega)} = N^{(v\omega)}_{ppn}\boldsymbol{p}\otimes\boldsymbol{p}\otimes\boldsymbol{n} + N^{(v\omega)}_{pnp}\boldsymbol{p}\otimes\boldsymbol{n}\otimes\boldsymbol{p}$ $+ N^{(v\omega)}_{qqn}\boldsymbol{q}\otimes\boldsymbol{q}\otimes\boldsymbol{n} + N^{(v\omega)}_{qnq}\boldsymbol{q}\otimes\boldsymbol{n}\otimes\boldsymbol{q}$ $+ N^{(v\omega)}_{npp}\boldsymbol{n}\otimes\boldsymbol{p}\otimes\boldsymbol{p} + N^{(v\omega)}_{nqq}\boldsymbol{n}\otimes\boldsymbol{q}\otimes\boldsymbol{q}$, $+N^{(v\omega)}_{nnn}\boldsymbol{n}\otimes\boldsymbol{n}\otimes\boldsymbol{n}$, $\mathbb{N}^{(vv)} = N^{(vv)}_{pqn}\boldsymbol{p}\otimes\boldsymbol{q}\otimes\boldsymbol{n} + N^{(vv)}_{pnq}\boldsymbol{p}\otimes\boldsymbol{n}\otimes\boldsymbol{q}$ $+N^{(vv)}_{qpn}\boldsymbol{q}\otimes\boldsymbol{p}\otimes\boldsymbol{n} + N^{(vv)}_{qnp}\boldsymbol{q}\otimes\boldsymbol{n}\otimes\boldsymbol{p}$ $+ N^{(vv)}_{npq}\boldsymbol{n}\otimes\boldsymbol{p}\otimes\boldsymbol{q} + N^{(vv)}_{nqp}\boldsymbol{n}\otimes\boldsymbol{q}\otimes\boldsymbol{p}$.	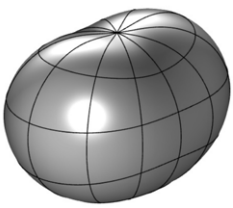 $r = 1 - \varepsilon(1 + \frac{\beta}{2}\cos\vartheta - \cos^2\varphi\sin^2\vartheta)$ $(\varepsilon = 0.3\,, \beta = 1.5)$

IV. NEARLY SPHERICAL PARTICLES

Table I summarises the structure of the coupling tensors derived in the previous Section for the symmetries O_h, $D_{2\mathrm{h}}$, $C_{\infty\mathrm{v}}$, and $C_{2\mathrm{v}}$. We tested these results for nearly spherical particles with the shape symmetries listed in Figure 2. To this end, we parameterised the particle boundary by the radius $r(\varphi,\vartheta)$. Here φ and ϑ are azimuthal and polar angles, that is $x = r(\varphi,\vartheta)\sin\vartheta\cos\varphi$, $y = r(\varphi,\vartheta)\sin\vartheta\sin\varphi$, $z = r(\varphi,\vartheta)\cos\vartheta$. Table I lists parameterisations for four particle shapes, namely O_h, $D_{2\mathrm{h}}$, $C_{\infty\mathrm{v}}$, and $C_{2\mathrm{v}}$. Using the theory described in Section II, we computed hydrodynamic force and torque as a joint perturbation expansion in Re_p and ε [36, 37]. The former is a singular expansion, the latter a regular one. This allows to extract the elements of the tensors discussed in the previous Section, or at least of certain sums of their elements. Our results for the particles in Table I confirm the symmetry analysis in Section III (Appendix B). We remark, however, that some coefficients vanish although they are allowed to be non-zero by particle-shape symmetries (Section V).

For example, for the special case $\alpha = 1$ in the second row of Table I, one obtains a parameterisation of the hydrodynamic torque on a nearly spherical spheroid. In this case, the torque component T_n vanishes, confirming the results of the symmetry analysis, Eq. (21a). The case of a nearly spherical spheroid was also considered by Cox [35]. He parameterised the major axis as $1+2\epsilon$ and the minor axis as $1-\epsilon$, in terms of a small parameter ϵ. Comparing with our parameterisation ($c = 1$ and $a = b = 1-\varepsilon$), we see that $\varepsilon = 3\epsilon$. Accounting for this factor of three, as well as a factor of 6π in the non-dimensionalisation of the torque in Ref [35], one concludes that our results agree with those of Cox [35].

V. DISCUSSION

The results summarised in Section III show how particle-shape symmetries constrain the hydrodynamic torque, including fluid-inertia contributions to order Re_p, extending earlier work by Brenner and Cox on corresponding constraints on the hydrodynamic force [34]. They determined under which circumstances the contributions from the $\mathbb{M}$ tensor to the hydrodynamic force vanish, by analysing how reflections as well as $\frac{\pi}{2}$- and π-rotations constrain $\mathbb{M}^{(vv)} : \boldsymbol{v}\otimes\boldsymbol{v}$. In a similar fashion, Cox [35] considered under which conditions the components of the vectors $\mathbb{N}^{(vv)} : \boldsymbol{v}\otimes\boldsymbol{v}$, $\mathbb{N}^{(v\omega)} : \boldsymbol{v}\otimes\boldsymbol{\omega}$ and $\mathbb{N}^{(\omega\omega)} : \boldsymbol{\omega}\otimes\boldsymbol{\omega}$ to vanish, because in that case steady force and torque are solely determined by the Stokes resistance tensors $\mathbb{A}$ (drag) and $\mathbb{B}$ (translation-rotation coupling).

For general shapes, these contributions do not vanish. In this case, the question is: how many parameters are needed to parameterise the dependence of the torque (and the force) upon particle velocity and angular velocity? Here we used symmetry analysis to answer this question. We determined how particle-shape symmetry constrains the non-zero elements of the coupling tensors. This determines the form of the torque, and in particular how many parameters are needed in parameterisations. The general structure of the torque becomes more complex (involves more parameters to be determined) as more shape symmetries are broken. In particular, any given shape symmetry implies that the resistance tensors $\mathbb{A}$ and $\mathbb{C}$ commute with the generator of the corresponding symmetry transformation. Full octahedral symmetry O_h requires that $\mathbb{A},\mathbb{B}$, and $\mathbb{C}$ commute with all rotational generators. This implies that these tensors are proportional to the unit matrix (isotropy). Now consider how rotations constrain the rank-3 tensors: the symmetries in the point-group O_h require that all rank-3 tensors are proportional to the Levi-Civita tensor $\boldsymbol{\epsilon}$, the only antisymmetric rank-3 tensor. Reflection symmetries constrain the rank-3 tensors further, namely $\mathbb{N}^{(v\omega)}$ as well as $\mathbb{M}^{(vv)}$ and $\mathbb{M}^{(\omega\omega)}$ must vanish. Reflection symmetries also cause $\mathbb{B}$ to vanish. The last two statements apply to all particles in the top row of Fig. 2.

For nearly spherical particles with different shape symmetries (Section IV), we found some cases where the symmetry analysis from Section III allows a non-zero coupling, but the coupling nevertheless vanishes to a certain order in perturbation theory. For $C_{\infty v}$-symmetry for example, the translation-rotation coupling $\mathbb{B}$ vanishes to order ε^2, although allowed by symmetry. In general, one expects that all coupling allowed by symmetry are non-zero unless there are additional symmetries not considered. The elements of $\mathbb{B}$ vanish to order ε^2 because the parameterisation $r = 1-\varepsilon(\sin^2\vartheta + \frac{\gamma}{2}\cos\vartheta)$ corresponds to a shifted spheroid. Expressing the torque w.r.t. the centre of mass cancels any potential contributions to the torque up to order ε^2. This happens also for C_{2v}-symmetry. In the latter case, we also find that $N^{(vv)}_{n(pq)}$ and $N^{(\omega\omega)}_{n(pq)}$ evaluate to zero to order ε. We expect that higher orders in ε are non-zero.

Candelier *et al.* [25] used the slender-body approximation to calculate the steady hydrodynamic force and torque on curved atmospheric fibres with C_{2v} symmetry, settling in quiescent air. In slender-body theory [28], force and torque are expressed as

$$\boldsymbol{F} = \int \mathrm{d}s\, \boldsymbol{f}(s)\,, \quad \boldsymbol{T} = \int \mathrm{d}s\, \boldsymbol{r}(s)\wedge\boldsymbol{f}(s)\,, \tag{30}$$

replacing Eqs. (1). Here $\boldsymbol{f}(s)$ is the force on a small segment of a slender body. It is obtained by asymptotic matching, as an expansion in $1/\log\kappa$ where κ is the (large) aspect ratio of the fibre. The results of Khayat and Cox [28] are obtained including the order $1/(\log\kappa)^2$ and assuming that the particle Reynolds number w.r.t the (small) radius a of the fibre is small (the particle Reynolds number w.r.t. to the fibre length can be of order unity). It has been shown that the predictions of Khayat and Cox [28] are accurate for aspect ratios greater than 30 and for small Reynolds numbers based on the fibre radius, *i.e.* $v_0 a/\nu \leq 0.1$. To order $\mathrm{Re_p} = v_0 a/\nu$, the resulting hydrodynamic force and torque contain at most third powers of $\hat{\boldsymbol{v}}$, just as Eqs. (13) and (14). Let us compare the slender-body results for the torque on curved fibres with C_{2v} symmetry [Eq. (3) in Candelier *et al.* [25]] with the present symmetry analysis, Eq. (25). The two expressions are consistent. The differences arise from a difference in the orientation of the basis. Here, the reflection symmetry $\boldsymbol{n} \to -\boldsymbol{n}$ is broken, while in Ref. [25], the symmetry $\boldsymbol{p} \to -\boldsymbol{p}$ is broken. However, the slender-body approximation has fewer terms than allowed by the symmetry analysis, similar to the nearly-spherical particles discussed above, although different terms are zero in that case. The allowed terms that vanish in the slender-body approximation are proportional to $B_{qn}A_{nn}$, while allowed terms proportional to $B_{nq}A_{qq}$ appear. This can be understood as follows. Computing the Stokes resistance tensors for planar fibres with constant radius of curvature using $\boldsymbol{f}(s)$ from Ref. [28], one concludes that A_{qq} and A_{nn} are of order $1/\log\kappa$, and so is B_{nq} [58]. The coefficient B_{qn}, by contrast, is proportional to $1/(\log\kappa)^2$. This means that the corresponding contribution to the torque is of order $1/(\log\kappa)^3$, and thus not contained in the slender-body theory of Khayat and Cox [28], to the order quoted there. The above dependencies on κ are confirmed by numerical results for B_{nq}/B_{qn} for a bead model obtained by modeling the fibres as chains of hydrodynamically interacting, identical beads (Table S1 in supplemental material of Ref. [25]): the numerical results are consistent with $B_{nq}/B_{qn} \sim \log\kappa$. The accuracy is approximately 2% when comparing $\kappa = 20$ with $\kappa = 40$.

This shortcoming of slender-body theory stems from approximations for the inner solution, namely that hydrodynamic interactions between different segments of the fibre are neglected (one has to go to higher orders in $1/(\log\kappa)$ to account for these interactions [59]). It is instructive to compare these conclusions with results for the bead model [25]. In that case, $\mathbb{B} = 0$ without hydrodynamic interactions in the centre-of-mass of the chain. This is no longer true if the beads have different sizes, or in the slender-body approximation where the fibre segments have different orientations.

In slender-body theory, higher orders in $\mathrm{Re_p} = a v_0/\nu$ result in higher powers of $\hat{\boldsymbol{v}}$ in the expressions for hydrodynamic force and torque. To obtain reasonable agreement between theory and experiment, Candelier *et al.* [25] found it necessary to include higher orders in $\mathrm{Re_p}$, not contained in Eq. (25) in Section III (although for spheroids, Bhowmick *et al.* [24] found that the linear approximation in $\mathrm{Re_p}$ works well if the prefactor is adjusted by an $\mathrm{Re_p}$-dependence). It is likely that higher-order singular contributions to force and torque are entirely determined by the Stokes tensors $\mathbb{A}$, $\mathbb{B}$, and $\mathbb{C}$. If this is the case, any other symmetry-breaking effects at larger particle Reynolds numbers must come from the inner solution.

At small but finite $\mathrm{Re_p}$, fluid inertia torques tend to align highly symmetric particles with the slip velocity. This is important in the atmospheric sciences, where the alignment of symmetric ice crystals (D_{nh} symmetry with $n > 2$) settling in the quiescent or weakly turbulent atmosphere [16–20, 24]. Calculations of torque and force for nearly spherical spheroids and slender fibres with circular cross sections [28] show that such particles – with D_{nh} symmetry with $n > 2$ – align so that they settle in quiescent air with their broad sides down. The fixed points of angular dynamics are dictated by rotational and fore-aft symmetry. Their stability is determined by the sign of the coefficient $N_1^{(vv)} + N_2^{(vv)}$ in Eq. (22) which depends on the aspect ratio of the spheroid. The coefficient changes sign at aspect ratio $\lambda = 1$ (sphere). Dabade *et al.* [29] calculated how $N_1^{(vv)} + N_2^{(vv)}$ depends on the particle aspect ratio, although their result differs from that of Cox [35] in the nearly spherical limit.

Andersen *et al.* [60] used an empirical torque model to describe fluttering and tumbling of platelets settling in a quiescent fluid at $\mathrm{Re_p}$ of order 10^3. For planar motion, they parameterise the out-of-plane component of the torque as $T_3 = c_1\omega + c_2\omega^2$ [their Eq. (3.9)]. The first term is consistent with Stokes torque (5). However, our symmetry analysis (Section III) does not produce the suggested ω^2 correction. Instead we find $(N_1^{(\omega\omega)} + N_2^{(\omega\omega)})\omega^2 \sin 2\theta$ for a spheroid to order $\mathrm{Re_p}$. In the spherical limit, the quadratic correction to the torque vanishes to this order in $\mathrm{Re_p}$, as observed by Rubinow and Keller [56]. Analysis of ab-initio data for force and torque on a thin disk (aspect ratio $\lambda = 0.2$) in unsteady motion in a quiescent fluid at $\mathrm{Re_p} \sim 2$ shows that there is a small ω^2 contribution to the torque consistent with $(N_1^{(\omega\omega)} + N_2^{(\omega\omega)})\omega^2 \sin 2\theta$. Any possible contribution of the form $c_2\omega^2$ is small. This is consistent with the direct numerical simulations of Pierson *et al.* [61] who considered the torque on a cylinder rotating perpendicular to its symmetry axis (with $\theta = 0$). They observe an ω^2-contribution, but only at large Reynolds numbers, not attainable from a first-order expansion in $\mathrm{Re_p}$.

For particles with prismatic symmetry (Fig. 2(**a**)), the symmetry analysis predicts that all three torque components are non-zero, in general. For specific orientations the torque may vanish. For example, if $\boldsymbol{\omega} = 0$, and $\hat{\boldsymbol{v}} = -\hat{\mathbf{e}}_3$, we have $v_p = \sin\theta\cos\psi, v_q = -\sin\theta\sin\psi$, and $v_n = -\cos\theta$. We see that there are six orientations where the torque

vanishes, each corresponding to one side of the particle in Figure 2(**a**) pointing down ($\theta = 0, \pm\frac{\pi}{2}$ and $\psi = 0, \pm\frac{\pi}{2}$). These are potential steady states of the angular dynamics at small $\mathrm{Re_p}$.

The laboratory experiments of Bhowmick *et al.* [42] show that ellipsoidal particles settling in quiescent air approach a steady orientation with their broadest side down. Eq. (20) explain this observation for nearly spherical ellipsoids, as the linear-stability analysis described in Appendix C shows. More generally, the symmetry analysis of Section III explains that particles with broken reflection symmetries ($C_{\infty v}$ and C_{2v}, for example) align differently, compared more symmetric particles discussed in the previous paragraph, such as spheroids and ellipsoids. The reason is that both Stokes and fluid-inertia torque are non-zero and can balance for certain orientations, provided that $\mathrm{Re_p}$ is not too large [38–40, 57]. Particles that align at a non-zero tilt angle as they settle in quiescent air move horizontally. This can affect the transport of such particles in the atmosphere, but standard models for the transport of atmospheric particles assume symmetrical shapes (spheroids) [41].

The previous paragraph discussed the steady-state problem, the orientation of a steadily settling particle. Now consider how the particle orientation changes as the steady state is approached. As explained in Section II, the transient is affected by history forces and torques arising from inertial fluid acceleration (the term $\partial_t \boldsymbol{w}$ in the unsteady Stokes equation. In this limit, the history force is well understood for a spherical particle settling in a quiescent fluid. The history force arises from the outer solution and decays slowly, as $t^{-1/2}$, after a sudden change of the particle dynamics [62]. Fluid-inertia corrections at small $\mathrm{Re_p}$ modify the power-law decay in a non-universal fashion [46], but the decay remains slow at small Reynolds numbers. The history torque, by contrast, decays rapidly for a sphere. Its kernel is essentially a Dirac delta function [63]. Since the torque is determined by the inner solution, it is expected that small-$\mathrm{Re_p}$ corrections do not change this fact. Eqs. (9) and (13) show that the situation is quite different for particles with non-zero translation–rotation coupling $\mathbb{B}$, because $\mathbb{B}$ results in a slow decay of the history torque as well. This history torque is expected to affect the transient dynamics of asymmetric particles settling at non-zero Reynolds numbers [25]. For spheroids ($\mathbb{B} = 0$) the relaxation of the orientational dynamics is well described [24], but as yet there is no reliable theory for the relaxation of particles with non-zero translation-rotation coupling outside the Stokes limit [25]. The main complication are the above-mentioned slowly decaying history torques.

Note that we computed the torque w.r.t. the centre-of-mass of the particle, and assumed a homogeneous mass-density distribution. An inhomogeneous distribution of the particle-mass density can shift the centre-of-mass, breaking further shape symmetries. Adjusting its centre-of-mass allows gliders settling in a quiescent fluid to navigate to land on a certain spot [64].

Our symmetry analysis is based on the theory for hydrodynamic forces and torques described in Section II, which is valid at non-zero but small $\mathrm{Re_p}$. How small the Reynolds number must be for the theory to work qualitatively or quantitatively depends on particle shape. For a spherical particle, the left of Eqs. (17) simplifies to the Oseen force (Appendix B), and it is well known that this works up to $\mathrm{Re_p} \sim 0.5$ [65]. The Rubinow-Keller lift force for a spherical particle [Eq. (B2)] is in good qualitative agreement with experiments up to $\mathrm{Re_p} \sim 5$ [66]. For fibres, Fintzi *et al.* [67] demonstrated that it is necessary to include the full functional form of the singular contribution at moderate Reynolds numbers ($\mathrm{Re_p} \geq 0.5$), especially for large aspect ratios, even though this range of Reynolds numbers probably lies beyond the validity of the present asymptotic analysis.

Bhowmick *et al.* [24] used empirical parameterisations of the fluid-inertia torque for spheroidal particles based on Eq. (22), with $\mathrm{Re_p}$-dependent coefficients. This works well up to $\mathrm{Re_p} \sim 20$, although the functional dependence of the coefficients has to be determined by comparison with particle-resolving simulations. In a similar way, the simulation results of Jiang *et al.* [30] and the experiments of Cabrera *et al.* [33] indicate that the functional form (22) is correct for fibres and spheroids, see also Refs. [67–69]. As mentioned above, slender-body theory [28] allows to include higher-order corrections in $\mathrm{Re_p}$, albeit only to order $1/(\log\kappa)^2$. The ab-initio simulations of Fintzi *et al.* [67] (see also Ref. Kharrouba *et al.* [70]) indicate that these refined predictions fail quantitatively for $\kappa = 30$ and $\mathrm{Re_p} \geq 0.5$ (with Reynolds number based on the radius of the fibre), because the large-aspect-ratio limit required by the theory of Khayat and Cox [28] was most likely not attained in the simulations. Candelier *et al.* [25], on the other hand, found qualitative agreement between the full slender-body theory for the torque on curved atmospheric fibres and experiments. Roy *et al.* [39] compared theory and experiment for the settling of straight slender fibres with broken fore-aft symmetry. They found good agreement between measurements and slender-body theory (including high-order $\mathrm{Re_p}$ corrections). These results indicate that the results presented here help to constrain fluid-inertia torques on particles of general shape. In the past, some authors have attempted to constrain the functional form of the fluid-inertia force by comparing with the potential-flow limit. The results of Candelier *et al.* [63] indicate, however, that this approach may be fallacious, because the expressions for the hydrodynamic force on a sphere in a linear flow are qualitatively different in the two limits. Whether it may help to constrain fluid-inertia torques remains an open question. In summary, only direct numerical simulations and dedicated experiments can serve as the final benchmark to test the range of validity of the theory present here.

We determined how shape symmetry constrains the hydrodynamical torque on an isotropic helicoid, an isotropic particle with non-zero translation-rotation coupling [52]. Our analysis shows that the coupling remains isotropic to

order $\mathrm{Re_p}$, just as in the potential-flow limit analysed by Lord Kelvin. We also saw that symmetry allows for a non-zero contribution $\mathbb{N}^{(v\omega)} : \boldsymbol{v} \otimes \boldsymbol{\omega} \propto \boldsymbol{v} \wedge \boldsymbol{\omega}$ to the fluid-inertia torque, analogous to the Rubinow-Keller lift force on a rotating sphere translating in a fluid at rest. In the Stokes limit, helical ribbons exhibit an infinite sequence of bifurcations as the translation-rotation coupling tensor passes through axisymmetry [15]. The theory described here can be used to determine fluid-inertia torques (and forces) on helical ribbons. This allows to determine how fluid-inertia corrections change the phase portraits of the angular dynamics.

The results described up to this point ignore the unsteady term of the disturbance equation in the inner solution, as one must in the stated limit $1 \gg \mathrm{Re_p} \gg \mathrm{Re_pSl}$. To conclude the discussion, we briefly consider the opposite limit $1 \gg \mathrm{Re_pSl} \gg \mathrm{Re_p}$ (details in Appendix D). In this limit, there are additional contributions to the regular parts of hydrodynamic force and torque

$$\boldsymbol{F}_{\mathrm{u}}^{(2)} = \mathrm{Re_pSl}(\mathbb{P}\dot{\boldsymbol{v}} + \mathbb{Q}\dot{\boldsymbol{\omega}})\,, \tag{31a}$$

$$\boldsymbol{T}_{\mathrm{u}}^{(2)} = \mathrm{Re_pSl}(\mathbb{Q}^{\mathsf{T}}\dot{\boldsymbol{v}} + \mathbb{R}\dot{\boldsymbol{\omega}})\,. \tag{31b}$$

Here dots denote time derivatives, and $\mathbb{P}$, $\mathbb{Q}$, and $\mathbb{R}$ are second-rank tensors that transform as Eqs. (6). Therefore they obey the same constraints as $\mathbb{A}$, $\mathbb{B}$, and $\mathbb{C}$. Eqs. (31) were first derived by Gavze [71] who obtained a general solution for the unsteady Stokes equation for a particle of arbitrary shape. We note that the unsteady solution also contains history terms. In Appendix D we show that these history terms agree with those derived in Section II to order $\sqrt{\mathrm{Re_pSl}}$. Collis *et al.* [37] solved the unsteady Stokes equation for nearly spherical particles with several different shapes in the frequency domain. One must obtain the kernels derived in Appendix D by integration over frequency.

VI. CONCLUSIONS

In this paper we used symmetry analysis to constrain the hydrodynamic torque on particles moving in a quiescent fluid at small but non-zero particle Reynolds number. For highly symmetrical particles, such as slender fibres with circular cross section and spheroids, fluid inertia torques were well understood [27–29], and known to describe how highly symmetric particles align as they settle in quiescent or weakly turbulent fluids [24].

The present study was motivated by recent interest in the angular dynamics of asymmetrical atmospheric particles [25, 38–40, 57], such as curved fibres, asymmetric ice crystals and ash particles. Here we show how breaking of shape symmetry allows new terms to appear in the hydrodynamic torque (and force), that can significantly change how particles align as they settle. The analysis shows that the bent disks of Miara *et al.* [14], and planar curved atmospheric fibres with constant radius of curvature [25] obey the same equations of motion, albeit with different parameters. The form of the equation of motion determines the possible dynamical behaviours by constraining the bifurcations that may occur as the parameters are varied. For example, in the Stokes limit the transition from alignment at small $\mathrm{Re_p}$ (curved fibre) to oscillations (bent disk) occurs when the product $B_{pq}B_{qp}$ of the non-zero translation-rotation coupling coefficients in Eq. (23) changes sign [25]. The results summarised here allow to determine how the bifurcations change for larger ribbons, as fluid-inertia corrections become important.

Regarding the hydrodynamic torque, our results generalise the theory of [35] to include unsteady effects, leading to slowly decaying history torques for asymmetrical particles with translation-rotation coupling (for symmetrical particles, history torques decay rapidly). Such unsteady effects influence the transient angular dynamics. In order to understand the transient angular dynamics for asymmetrical, curved atmospheric fibres [24], we expect history torques to play a role. Similar conclusions are expected for bent disks [14], which have the same point-group shape symmetry as planar fibres with constant radius of curvature.

Even in the absence of history torques, one expects complex settling trajectories even for symmetrical particles settling in quiescent air. For example, our theory shows that the transient dynamics of ellipsoids is governed by three couplings (the six non-zero elements of the rank-3 tensor $\mathbb{N}^{(vv)}$ which take different values depending on the aspect ratios of the ellipsoidal particle. This – together with the fact that all three components of the hydrodynamical torque are non-zero – explains the rich variety of settling behaviours observed in the experiment [42], but a detailed computation of the transient dynamics remains a question for the future. Regarding the steady limit, our calculations show that nearly spherical ellipsoids settle with their broadest side down, as observed in the experiment [42]. To confirm that this conclusion is valid for ellipsoidal particles with arbitrary aspect ratios, one needs to compute the three symmetrised coefficients in Eq. (20) for the torque by direct numerical simulation.

The results discussed here were obtained in the limit of small Reynolds numbers, $\mathrm{Re_p} \ll 1$. An important question is how the particle dynamics changes as the Reynolds number increases. For spheroids in shear flow, bifurcations that occur at larger shear Reynolds numbers Re_s have been mapped out, and it turns out that the small-Re theory remains qualitatively valid for Re_s up to order unity. For spheroids settling in a quiescent fluid, one can obtain quantitative agreement with experiments using empirical torque models similar to those discussed here [24]. For particles with

broken shape symmetry [25], the expressions derived here yield qualitative but not quantitative agreement with the experiments. How the accuracy of small-Re approximations breaks down for highly asymmetric particles as the Reynolds number increases remains an open question. It may be instructive to compare the results of the present analysis with the potential-flow limit, the limit considered by Lord Kelvin in his analysis of the isotropic helicoid [52]. Corresponding expressions for hydrodynamic force and torque can be obtained for particles of arbitrary shape using either the Lagrangian formalism [72], or by direct integration of the pressure on the body [73]. However, the results of Candelier *et al.* [63] indicate that even for a spherical particle, hydrodynamic force and torque can be quite different in the two limits. As a consequence it may be challenging to find convincing interpolation formulae between the two limits.

Last but not least, symmetry analysis as described here can be used to constrain hydrodynamical forces and torques on motile micro-organisms. The standard model assumes that the organisms are spherical, but this is an idealisation. In the future we will analyse how the interaction of microswimmers with the surrounding flow changes when shape symmetries are broken. To this end, one needs to generalise the present analysis to account for strain and vorticity of the undisturbed flow. For special cases this is known [8, 11, 44, 45], but not in general.

ACKNOWLEDGMENTS

LS and BM were supported by VR grant no. 2021-4452. This work was completed while BM held a Gauss professorship in Göttingen, financed by the Göttingen Academy of Sciences and Humanity in Lower Saxony. KG was supported by VR grant no. 2023-03617.

[1] S.K.P. Sanjeevi, J.A.M. Kuipers, and J.T. Padding, "Drag, lift and torque correlations for non-spherical particles from Stokes limit to high Reynolds numbers," Int. J. Multiphase Flow **106**, 325–337 (2018).
[2] R. Ouchene, M. Khalij, A. Tanière, and B. Arcen, "Drag, lift and torque coefficients for ellipsoidal particles: from low to moderate particle Reynolds numbers," Computers & Fluids **113**, 53–64 (2015).
[3] R. Ouchene, M. Khalij, B. Arcen, and A. Tanière, "A new set of correlations of drag, lift and torque coefficients for non-spherical particles at large Reynolds numbers," Powder Technology **303**, 33–43 (2016).
[4] R. Ouchene, "Numerical simulation and modeling of the hydrodynamic forces and torque acting on individual oblate spheroids," Phys. Fluids **32**, 073303 (2020).
[5] A. Hölzer and M. Sommerfeld, "Lattice Boltzmann simulations to determine drag, lift and torque acting on non-spherical particles," Computers & Fluids **38**, 572–589 (2009).
[6] M. Zastawny, G. Mallouppas, F. Zhao, and B. van Wachem, "Derivation of drag and lift forces and torque coefficients for non-spherical particles in flow," International Journal of Multiphase Flow **39**, 227–239 (2012).
[7] K. Fröhlich, M. Meinke, and W. Schröder, "Correlations for inclide prolates based on highly resolved simulations," J. Fluid Mech. **901**, A5 (2020).
[8] F.P. Bretherton, "The motion of rigid particles in a shear flow at low Reynolds number," J. Fluid Mech. **14**, 284–304 (1962).
[9] H. Brenner, "The Stokes resistance of a slightly deformed sphere," Chem. Eng. Sci. **19**, 519–539 (1964).
[10] J. Happel and H. Brenner, *Low Reynolds Number Hydrodynamics* (Martinus Nijhoff Publishers, Hague, 1983).
[11] J. Fries, J. Einarsson, and B. Mehlig, "Angular dynamics of small crystals in viscous flow," Phys. Rev. Fluids **2**, 014302 (2017).
[12] T.A. Witten and H. Diamant, "A review of shaped colloidal particles in fluids: anisotropy and chirality," Reports on progress in physics **83**, 116601 (2020).
[13] D. Collins, R.J. Hamati, F. Candelier, K. Gustavsson, B. Mehlig, and G.A. Voth, "Lord Kelvin's isotropic helicoid," Phys. Rev. Fluids **6**, 074302 (2021).
[14] T. Miara, C. Vaquero-Stainer, D. Pihler-Puzović, M. Heil, and A. Juel, "Dynamics of inertialess sedimentation of a rigid u-shaped disk," Comm. Phys. **7**, 47 (2024).
[15] E. Huseby, J. Gissinger, F. Candelier, N. Pujara, G. Verhille, B. Mehlig, and G. Voth, "Helical ribbons: Simple chiral sedimentation," Phys. Rev. Fluids **10**, 024101 (2025).
[16] A. J. Heymsfield, "Laboratory and field observations of the growth of columnar and plate crystals from frozen droplets," JAS **30**, 1650–1656 (1973).
[17] K. Sassen, "Remote sensing of planar ice crystal fall attitudes," J. Meteor. Soc. Japan. Ser. II **58**, 422–429 (1980).
[18] J. D. Klett, "Orientation model for particles in turbulence," JAS **52**, 2276 – 2285 (1995).
[19] V. Noel and K. Sassen, "Study of planar ice crystal orientations in ice clouds from scanning polarization lidar observations," J. Appl. Meteorol. **44**, 653 – 664 (2005).
[20] K. Gustavsson, M. Z. Sheikh, A. Naso, A. Pumir, and B. Mehlig, "Effect of particle inertia on the alignment of small ice crystals in turbulent clouds," JAS **78**, 2573 – 2587 (2021).

[21] R. K. Newsom and C. W. Bruce, "The dynamics of fibrous aerosols in a quiescent atmosphere," Phys. Fluids **6**, 521–530 (1994).

[22] R.K. Newsom and C.W. Bruce, "Orientational properties of fibrous aerosols in atmospheric turbulence," J. Aerosol Sci. **29**, 773–797 (1998).

[23] J.-L. Pierson, "Inertial settling of an arbitrarily oriented cylinder in a quiescent flow: From short-time to quasisteady motion," Phys. Rev. Fluids **8**, 104301 (2023).

[24] T. Bhowmick, J. Seesing, K. Gustavsson, J. Guettler, Y. Wang, A. Pumir, B. Mehlig, and G. Bagheri, "Inertia induces strong orientation fluctuations of nonspherical atmospheric particles," Phys. Rev. Lett. **132**, 034101 (2024).

[25] F. Candelier, K. Gustavsson, P. Sharma, L. Sundberg, A. Pumir, G. Bagheri, and B. Mehlig, "Torques on curved atmospheric fibres," (2024), arXiv:2409.19004.

[26] Y. Cai, D.M. Mitrano, M. Heuberger, R.Hufenus, and B. Nowack, "The origin of microplastic fiber in polyester textiles: The textile production process matters," Journal of Cleaner Production **267**, 121970 (2020).

[27] H. Brenner, "The Oseen resistance of a particle of arbitrary shape," J. Fluid Mech. **11**, 604–610 (1961).

[28] R.E. Khayat and R.G. Cox, "Inertia effects on the motion of long slender bodies," J. Fluid Mech. **209**, 435–462 (1989).

[29] V. Dabade, N. K. Marath, and G. Subramanian, "Effects of inertia and viscoelasticity on sedimenting anisotropic particles," J. Fluid Mech. **778**, 133–188 (2015).

[30] F. Jiang, L. Zhao, H. I. Andersson, K. Gustavsson, A. Pumir, and B. Mehlig, "Inertial torque on a small spheroid in a stationary uniform flow," Phys. Rev. Fluids **6**, 024302 (2021).

[31] D. Lopez and E. Guazzelli, "Inertial effects on fibers settling in a vortical flow," Phys. Rev. Fluids **2**, 024306 (2017).

[32] A. Roy, S. Kramel, U. Menon, G.A. Voth, and D.L. Koch, "Orientation of finite Reynolds number anisotropic particles settling in turbulence," Journal of Non-Newtonian Fluid Mechanics **318**, 105048 (2023).

[33] F. Cabrera, M. Z. Sheikh, B. Mehlig, N. Plihon, M. Bourgoin, A. Pumir, and A. Naso, "Experimental validation of fluid inertia models for a cylinder settling in a quiescent flow," Phys. Rev. Fluids **7**, 024301 (2022).

[34] H. Brenner and R. G. Cox, "The resistance to a particle of arbitrary shape in translational motion at small Reynolds numbers," J. Fluid Mech. **17**, 561–595 (1963).

[35] R.G. Cox, "The steady motion of a particle of arbitrary shape at small Reynolds numbers," J. Fluid Mech. **23**, 625–643 (1965).

[36] F. Candelier, J. Einarsson, F. Lundell, B. Mehlig, and J.-R. Angilella, "Role of inertia for the rotation of a nearly spherical particle in a general linear flow," Phys. Rev. E **91**, 053023 (2015).

[37] J. F. Collis, A. Nunn, and J. E. Sader, "Unsteady motion of nearly spherical particles in viscous fluids: a second-order asymptotic theory," Journal of Fluid Mechanics **1001**, A23 (2024).

[38] F. Candelier and B. Mehlig, "Settling of an asymmetric dumbbell in a quiescent fluid," J. Fluid Mech. **802**, 174–185 (2016).

[39] A. Roy, R.J. Hamati, L. Tierney, D.L. Koch, and G.A. Voth, "Inertial torques and a symmetry breaking orientational transition in the sedimentation of slender fibres," J. Fluid Mech. **875**, 576–596 (2019).

[40] S. Ravichandran and J. S. Wettlaufer, "Orientation dynamics of two-dimensional concavo-convex bodies," Phys. Rev. Fluids **8**, L062301 (2023).

[41] D. Tatsii, S. Bucci, T. Bhowmick, J. Guettler, L. Bakels, G. Bagheri, and A. Stohl, "Shape matters: Long-range transport of microplastic fibers in the atmosphere," Environmental Science & Technology **58**, 671–682 (2024).

[42] T. Bhowmick, Y. Wang, J. Latt, and G Bagheri, "Twist, turn and encounter: the trajectories of small atmospheric particles unravelled," Journal of Fluid Mechanics **1021**, A27 (2025).

[43] S. Kim and S.J. Karrila, *Microhydrodynamics: principles and selected applications* (Butterworth-Heinemann, Boston, 1991).

[44] H. Brenner, "The Stokes resistance of an arbitrary particle—III: Shear fields," Chem. Eng. Sci. **19**, 631–651 (1964).

[45] K. Ishimoto, "Jeffery orbits for an object with discrete rotational symmetry," Phys. Fluids **32** (2020).

[46] P. M. Lovalenti and J. F. Brady, "The hydrodynamic force on a rigid particle undergoing arbitrary time-dependent motion at small Reynolds number," Journal of Fluid Mechanics **256**, 561–605 (1993).

[47] S. Childress, "The slow motion of a sphere in a rotating, viscous fluid," J. Fluid Mech. **20**, 305–314 (1964).

[48] P. G. T. Saffman, "The lift on a small sphere in a slow shear flow," Journal of fluid mechanics **22**, 385–400 (1965).

[49] J. Meibohm, F. Candelier, T. Rosén, J. Einarsson, F. Lundell, and B. Mehlig, "Angular velocity of a spheroid log rolling in a simple shear at small Reynolds number," Phys. Rev. Fluids **1**, 084203 (2016).

[50] T. Redaelli, F. Candelier, R. Mehaddi, C. Eloy, and B. Mehlig, "Hydrodynamic force on a small squirmer moving with a time-dependent velocity at small Reynolds numbers," Journal of Fluid Mechanics **973**, A11 (2023).

[51] M. M. Flapper, G. Piumini, R. Verzicco, S. G. Huisman, and D. Lohse, "Settling dynamics of an oloid: experiments and simulations," (2025), arXiv:2511.05137 [physics.flu-dyn].

[52] Lord Kelvin, "Hydrokinetic solutions and observations," Phil. Mag. **42**, 362 (1871).

[53] N. W. Ashcroft and N. D. Mermin, *Solid State Physics* (Holt-Saunders, 1976).

[54] U. Nakaya, *Snow Crystals: Natural and Artificial* (Harvard University Press, 1954).

[55] Y. Furukawa and J. S. Wettlaufer, "Snow and ice crystals," Physics Today **60**, 70–71 (2007).

[56] S. I. Rubinow and Joseph B. Keller, "The transverse force on a spinning sphere moving in a viscous fluid," Journal of Fluid Mechanics **11**, 447–459 (1961).

[57] Z. Maches, M. Houssais, A. Sauret, and E. Meiburg, "Settling of two rigidly connected spheres," (2024), arXiv:2406.10381.

[58] R. G. Cox, "The motion of long slender bodies in a viscous fluid Part 1. General theory," J. Fluid Mech. **44**, 791–810 (1970).

[59] J. B. Keller and S. I. Rubinow, "Slender-body theory for slow viscous flow," Journal of Fluid Mechanics **75**, 705–714

(1976).
[60] A. Andersen, U. Pesavento, and Z. Jane Wang, "Unsteady aerodynamics of fluttering and tumbling plates," Journal of Fluid Mechanics **541**, 65 (2005).
[61] J.-L. Pierson, M. Kharrouba, and J. Magnaudet, "Hydrodynamic torque on a slender cylinder rotating perpendicularly to its symmetry axis," Phys. Rev. Fluids **6**, 094303 (2021).
[62] L. D. Landau and E. M. Lifshitz, *Fluid mechanics*, 2nd ed. (Pergamon Press, 1987).
[63] F. Candelier, R. Mehaddi, B. Mehlig, and J. Magnaudet, "Second-order inertial forces and torques on a sphere in a viscous steady linear flow," J. Fluid Mech. **954**, A25 (2023).
[64] X. Jiang, J. Qiu, K. Gustavsson, B. Mehlig, and L. Zhao, "Smart navigation of a gravity-driven glider with adjustable centre-of-mass," (2025), arXiv:2510.09250.
[65] W. Chester, D.R. Breach, and I. Proudman, "On the flow past a sphere at low Reynolds number," J. Fluid Mech. **37**, 751–760 (1969).
[66] B. Oesterle and T. Bui Dinh, "Experiments on the lift of a spinning sphere in a range of intermediate Reynolds numbers," Experiments in Fluids **25**, 16 (1998).
[67] N. Fintzi, L. Gamet, and J.-L. Pierson, "Inertial loads on a finite-length cylinder embedded in a steady uniform flow," Phys. Rev. Fluids **8**, 044302 (2023).
[68] R. Ouchene, M. Khalij, B. Arcen, and A. Tanière, "A new set of correlations of drag, lift and torque coefficients for non-spherical particles at large Reynolds numbers," Powder Technology **303**, 33–43 (2016).
[69] S. K. P. Sanjeevi and J. T. Padding, "On the orientational dependence of drag experienced by spheroids," J. Fluid Mech. **820**, R1 (2017).
[70] M. Kharrouba, J.-L. Pierson, and J. Magnaudet, "Flow structure and loads over inclined cylindrical rodlike particles and fibers," Phys. Rev. Fluids **6**, 044308 (2021).
[71] E. Gavze, "The accelerated motion of rigid bodies in non-steady stokes flow," Int. J. Multiph. Flow **16**, 153 (1990).
[72] H. Lamb, *Hydrodynamics* (University Press, 1924).
[73] M. S. Howe, "On the force and moment on a body in an incompressible fluid, with application to rigid bodies and bubbles at high and low Reynolds numbers," The Quarterly Journal of Mechanics and Applied Mathematics **48**, 401–426 (1995).
[74] D. Legendre and J. Magnaudet, "A note on the lift force on a spherical bubble or drop in a low-Reynolds-number shear flow," Phys. Fluids **9**, 3572–3574 (1997).

Appendix A: Fluid-inertia kernels

We use asymptotic matching [47, 48] to find a solution to the disturbance equation (2) assuming that $1 \gg \mathrm{Re_p} \gg \mathrm{Re_pSl}$. The calculation is very similar to the one in Ref. [50], except for two differences. First, here we consider a passive particle which simplifies the expression for $\boldsymbol{f}_0$. Second, here we consider non-spherical particles and allow force and particle velocity to point in different directions. For spherical particles, hydrodynamic force [74] and torque [49] are entirely determined by the outer solution. For a particle of general shape the inner solution depends on particle shape and can contribute to force and torque. In the outer solution, particle shape enters only as the amplitude of a source term in the disturbance equation. The outer solution is obtained as a convolution of this shaped-dependent amplitude with a universal kernel (equivalent to that obtained by Lovalenti and Brady [46]) that depends on the history of the particle dynamics. The kernels in Eq. (9) in the main text have elements:

$$\begin{aligned}[\mathbb{K}^{(1)}(t,\tau)]_{ij} = &-\frac{1}{8\pi}\left(\frac{\exp(-A(t,\tau)^2)}{\sqrt{\pi}A(t,\tau)^2}+\frac{\operatorname{erf}(A(t,\tau))(A(t,\tau)^2-\frac{1}{2}))}{A(t,\tau)^3}\right)\frac{\delta_{ij}}{\sqrt{t-\tau}}\\ &+\frac{1}{8\pi}\left(\frac{3\exp(-A(t,\tau)^2)}{2\sqrt{\pi}A(t,\tau)^2}+\frac{\operatorname{erf}(A(t,\tau))(A(t,\tau)^2-\frac{3}{2})}{2A(t,\tau)^3}\right)\frac{\delta_{ij}-\hat{a}_i(t,\tau)\hat{a}_j(t,\tau)}{\sqrt{t-\tau}}\,.\end{aligned} \tag{A1}$$

and

$$\begin{aligned}[\mathbb{K}^{(2)}(t,\tau)]_{ij} =&\frac{1}{8\pi}\frac{1}{4A(t,\tau)}\left(\frac{3\exp(-A(t,\tau)^2)}{\sqrt{\pi}A(T,\tau)^2}+\frac{\operatorname{erf}(A(t,\tau))(A(t,\tau)^2-\frac{3}{2})}{A(t,\tau)^3}\right)\\ &\times\frac{v_i(\tau)\hat{a}_j(t,\tau)+\hat{a}_i(t,\tau)v_j(\tau)-4[\boldsymbol{v}(\tau)\cdot\hat{\boldsymbol{a}}(t,\tau)]\hat{a}_i(t,\tau)\hat{a}_j(t,\tau)}{t-\tau}\\ &-\frac{1}{8\pi}\frac{1}{4A(t,\tau)}\left(\frac{(-4A(t,\tau)^2-3)\exp(-A(t,\tau)^2))}{\sqrt{\pi}A(t,\tau)^2}+\frac{\operatorname{erf}(A(t,\tau))(A(t,\tau)^2+\frac{3}{2})}{A(t,\tau)^3}\right)[\boldsymbol{v}(\tau)\cdot\hat{\boldsymbol{a}}(t,\tau)]\\ &\times\frac{\delta_{ij}-\hat{a}_i(t,\tau)\hat{a}_j(t,\tau)}{t-\tau}\,.\end{aligned} \tag{A2}$$

In these expressions, $\boldsymbol{f}^{(0)}$ is the force exerted by the particle upon the fluid in the Stokes limit, $A(t,\tau)$ is the norm of the pseudo-displacement vector $\boldsymbol{a}(t,\tau)$ initially introduced by Lovalenti and Brady [46]

$$\boldsymbol{a}(t,\tau)=\frac{1}{2}\sqrt{\frac{\mathrm{Re_p}}{\mathrm{Sl}}}\frac{1}{\sqrt{t-\tau}}\int_\tau^t \mathrm{d}t'\boldsymbol{v}(t')\,, \tag{A3}$$

and $\hat{\boldsymbol{a}}=\boldsymbol{a}/A(t,\tau)$. In the steady limit, Eq. (A3) implies $\boldsymbol{a}=\frac{1}{2}\sqrt{\frac{\mathrm{Re_p}}{\mathrm{Sl}}}\sqrt{t-\tau}\,\boldsymbol{v}$ and therefore $\hat{\boldsymbol{a}}=\hat{\boldsymbol{v}}$. Using these results, we see that Eq. (9) simplifies to Eq. (16) in the steady limit. These kernels are equivalent to those obtained by Lovalenti and Brady [46]. But the details differ because the decomposition into two integrals, one involving $\boldsymbol{f}^{(0)}$ and the other involving $\mathrm{d}\boldsymbol{f}^{(0)}/\mathrm{d}\tau$ is not unique. The above equations are more general than those derived in Ref. [50], where it was assumed that $\boldsymbol{f}^{(0)}$ and $\hat{\boldsymbol{v}}$ are collinear.

Appendix B: Coupling tensors for nearly spherical particles

In this Appendix, we quote results for the elements of the coupling tensors obtained for the nearly spherical particles listed in Table I. The results were obtained as follows. To each order in the asymptotic-matching calculation one needs to solve a Stokes problem, as described in Ref. [50]. These Stokes problems are solved for nearly spherical particles by expanding in the small non-sphericity parameter ε as described in the Appendix of Ref. [36].

1. O_h-symmetry

The results for O_h symmetry are well known [10]. The tensors $\mathbb{A}$ and $\mathbb{C}$ are isotropic:

$$A_{pp}=A_{qq}=A_{nn}=6\pi-\frac{9}{5}\pi\varepsilon+\frac{116}{525}\pi\varepsilon^2\,,\quad\text{and}\quad C_{pp}=C_{qq}=C_{nn}=8\pi-\frac{36}{5}\varepsilon\pi+\frac{1678}{525}\varepsilon^2\pi\,, \tag{B1a}$$

The tensor $\mathbb{B}$ vanishes. For $\varepsilon = 0$, Eq. (17) yields the Oseen drag on a spherical particle

$$\boldsymbol{F} = 6\pi(1 - \tfrac{3}{8}\mathrm{Re_p} v)\boldsymbol{v}\,. \tag{B1b}$$

The following rank-3 tensors are non-zero: $\mathbb{M}^{(v\omega)} = M^{(v\omega)}\boldsymbol{\epsilon}$, $\mathbb{N}^{(vv)} = N^{(vv)}\boldsymbol{\epsilon}$, and $\mathbb{N}^{(\omega\omega)} = N^{(\omega\omega)}\boldsymbol{\epsilon}$. The tensors $\mathbb{N}^{(vv)}$ and $\mathbb{N}^{(\omega\omega)}$ do not contribute because they are doubly contracted with a symmetrical tensor. For $M^{(v\omega)}$ we find to order ε

$$M^{(v\omega)} = -\big(\pi - \tfrac{9}{10}\pi\varepsilon\big)\,. \tag{B1c}$$

Eq. (B1c) yields the Keller-Rubinow lift force for a nearly spherical particle with O_h symmetry. In dimensional form, we obtain

$$\boldsymbol{F} = -\varrho_\mathrm{f}\nu a v_0 \mathrm{Re_p}\pi(1 - \tfrac{9}{10}\varepsilon)\boldsymbol{v}\wedge\boldsymbol{\omega}/(v_0\omega_0) = \varrho_\mathrm{f} a^3\pi(1 - \tfrac{9}{10}\varepsilon)\boldsymbol{\omega}\wedge\boldsymbol{v}\,. \tag{B2}$$

For $\varepsilon = 0$, this is Eq. (71) in Ref. [56].

2. D_{2h}-symmetry

For D_{2h} symmetry, we find the following non-zero coefficients,

$$\begin{aligned}
&A_{pp} = 6\pi + \big(-\tfrac{12}{5}\pi - \tfrac{6}{5}\alpha\pi\big)\,\varepsilon\,, \quad A_{qq} = 6\pi + \big(-\tfrac{6}{5}\pi - \tfrac{12}{5}\alpha\pi\big)\,\varepsilon\,, \quad A_{nn} = 6\pi + \big(-\tfrac{12}{5}\alpha\pi - \tfrac{12}{5}\pi\big)\,\varepsilon\,, \\
&C_{pp} = 8\pi + \big(-\tfrac{48}{5}\pi - \tfrac{24}{5}\alpha\pi\big)\,\varepsilon\,, \quad C_{qq} = 8\pi + \big(-\tfrac{24}{5}\pi - \tfrac{48}{5}\alpha\pi\big)\,\varepsilon\,, \quad C_{nn} = 8\pi + \big(-\tfrac{48}{5}\pi - \tfrac{48}{5}\alpha\pi\big)\,\varepsilon\,, \\
&2N^{(\omega\omega)}_{p(nq)} = \tfrac{1}{15}\pi\varepsilon\,, \quad 2N^{(\omega\omega)}_{q(np)} = -\tfrac{1}{15}\pi\alpha\varepsilon\,, \quad 2N^{(\omega\omega)}_{n(pq)} = \tfrac{1}{15}\pi(\alpha-1)\varepsilon\,, \\
&2N^{(vv)}_{p(nq)} = \tfrac{29}{20}\pi\varepsilon\,, \quad 2N^{(vv)}_{q(np)} = -\tfrac{29}{20}\pi\alpha\varepsilon\,, \quad 2N^{(vv)}_{n(pq)} = \tfrac{29}{20}\pi(\alpha-1)\varepsilon\,, \\
&M^{(v\omega)}_{pqn} = -\pi + \big(\tfrac{2}{5}\alpha\pi + \tfrac{37}{20}\pi\big)\,\varepsilon\,, \quad M^{(v\omega)}_{pnq} = \pi - \big(\tfrac{2}{5}\alpha\pi + \tfrac{3}{4}\pi\big)\,\varepsilon\,, \\
&M^{(v\omega)}_{qnp} = \pi - \big(\tfrac{2}{5}\alpha\pi + \tfrac{3}{4}\pi\big)\,\varepsilon\,, \quad M^{(v\omega)}_{qpn} = \pi - \big(\tfrac{2}{5}\pi + \tfrac{37}{20}\alpha\pi\big)\,\varepsilon\,, \\
&M^{(v\omega)}_{nqp} = \pi - \big(\tfrac{3}{4}\alpha\pi + \tfrac{37}{20}\pi\big)\,\varepsilon\,, \quad M^{(v\omega)}_{npq} = -\pi + \big(\tfrac{3}{4}\pi + \tfrac{37}{20}\alpha\pi\big)\,\varepsilon\,,
\end{aligned} \tag{B3}$$

confirming the symmetry analysis in Section III [Eq. (19)]. For $\alpha = 1$ the particle shape is spheroidal ($C_{\infty h}$). As explained in the main text, this constrains more coefficients to vanish [Eq. (22)].

3. $C_{\infty v}$-symmetry

For a particle with broken fore-aft symmetry (third row in Table I), we find the following non-zero coupling coefficients

$$\begin{aligned}
&A_\perp = 6\pi - \tfrac{18}{5}\pi\varepsilon + \big(\tfrac{198}{175}\pi + \tfrac{9}{20}\gamma^2\pi\big)\,\varepsilon^2\,, \quad A_\parallel = 6\pi - \tfrac{24}{5}\pi\varepsilon + \big(\tfrac{192}{175}\pi + \tfrac{3}{5}\gamma^2\pi\big)\,\varepsilon^2\,, \\
&C_\perp = 8\pi - \tfrac{72}{5}\pi\varepsilon + \big(\tfrac{2736}{175}\pi + \tfrac{9}{5}\gamma^2\pi\big)\,\varepsilon^2\,, \quad C_\parallel = 8\pi - \tfrac{96}{5}\pi\varepsilon + \big(\tfrac{3264}{175}\pi + \tfrac{12}{5}\gamma^2\pi\big)\,\varepsilon^2, \\
&N_1^{(vv)} + N_2^{(vv)} = \tfrac{29}{20}\pi\varepsilon \quad \text{and} \quad N_1^{(\omega\omega)} + N_2^{(\omega\omega)} = \tfrac{\pi}{15}\,, \\
&N_1^{(v\omega)} = \pi\gamma\varepsilon\,, \quad \text{and} \quad N_3^{(v\omega)} = -\pi\gamma\varepsilon\,, \\
&M_1^{(\omega\omega)} + M_2^{(\omega\omega)} = -\tfrac{1}{6}\pi\gamma\varepsilon\,, \quad \text{and} \quad M_3^{(\omega\omega)} = \tfrac{1}{6}\pi\gamma\varepsilon\,, \\
&M_1^{(v\omega)} = \pi - \tfrac{23}{20}\pi\varepsilon\,, \quad M_2^{(v\omega)} = -\pi + \tfrac{9}{4}\pi\varepsilon\,, \quad \text{and} \quad M_3^{(v\omega)} = -\pi + \tfrac{13}{5}\pi\varepsilon\,.
\end{aligned} \tag{B4}$$

The tensors $\mathbb{B}$, $\mathbb{N}^{(vv)}$, and $\mathbb{N}^{(\omega\omega)}$ were computed with respect to the centre-of-mass $\boldsymbol{x}_\mathrm{com} = -\frac{\gamma}{2}\varepsilon\hat{\boldsymbol{e}}_3$. The coupling coefficients $M_4^{(vv)}$ and $M_4^{(\omega\omega)}$ vanish to order ε although they are allowed to be non-zero by symmetry. The tensor $\mathbb{B}$ vanishes to order ε^2, although allowed to be non-zero by the symmetry analysis. We quote the elements of $\mathbb{A}$ and $\mathbb{C}$ to second order in ε, to show their γ-dependence which occurs only at this order.

4. C_{2v}-symmetry

For a nearly spherical particle with C_{2v}-symmetry (fourth row in Table I), we find the following non-zero coupling coefficients

$$A_{pp}=6\pi-\tfrac{24\pi}{5}\varepsilon+\left(\tfrac{192\pi}{175}+\tfrac{9\pi}{20}\beta^2\right)\varepsilon^2, A_{qq}=6\pi-\tfrac{18\pi}{5}\varepsilon+\left(\tfrac{198\pi}{175}+\tfrac{9\pi}{20}\beta^2\right)\varepsilon^2, A_{nn}=6\pi-\tfrac{18\pi}{5}\varepsilon+\left(\tfrac{198\pi}{175}+\tfrac{3\pi}{5}\beta^2\right)\varepsilon^2, \tag{B5}$$

$$C_{pp}=8\pi-\tfrac{96}{5}\pi\varepsilon+\left(\tfrac{3264\pi}{175}+\tfrac{9\pi}{5}\beta^2\right)\varepsilon^2, C_{qq}=8\pi-\tfrac{72\pi}{5}\varepsilon+\left(\tfrac{2736\pi}{175}+\tfrac{9\pi}{5}\beta^2\right)\varepsilon^2, C_{nn}=8\pi-\tfrac{72}{5}\pi\varepsilon+\left(\tfrac{2736\pi}{175}+\tfrac{12\pi}{5}\beta^2\right)\varepsilon^2,$$

$$2N^{(vv)}_{q(pn)}=\tfrac{29}{20}\pi\varepsilon, \quad 2N^{(vv)}_{n(pq)}=-\tfrac{29}{20}\pi\varepsilon,$$

$$2N^{(\omega\omega)}_{q(pn)}=\tfrac{1}{15}\pi\varepsilon, \quad 2N^{(\omega\omega)}_{n(pq)}=-\tfrac{1}{15}\pi\varepsilon,$$

$$N^{(v\omega)}_{pnp}=N^{(v\omega)}_{qnq}=\beta\pi\varepsilon, \quad N^{v\omega}_{npp}=N^{v\omega}_{nqq}=-\beta\pi\varepsilon,$$

$$2M^{(\omega\omega)}_{p(pn)}=2M^{(\omega\omega)}_{q(np)}=-\tfrac{1}{6}\pi\beta\varepsilon, \quad 2M^{(\omega\omega)}_{n(pp)}=2M^{(\omega\omega)}_{n(qq)}=\tfrac{1}{6}\pi\beta\varepsilon,$$

$$M^{(v\omega)}_{pqn}=-M^{(v\omega)}_{pnq}=-\pi+\tfrac{13}{5}\pi\varepsilon, \quad M^{(v\omega)}_{qpn}=-M^{(v\omega)}_{npq}=\pi-\tfrac{23}{20}\pi\varepsilon, \quad M^{(v\omega)}_{qnp}=-M^{(v\omega)}_{nqp}=-\pi+\tfrac{9}{4}\pi\varepsilon,$$

The elements of $\mathbb{B}$ $\mathbb{C}$, and $\mathbb{N}$ were computed with respect to the centre-of-mass $\boldsymbol{x}_{\rm com}=-\frac{\beta}{2}\varepsilon\hat{\boldsymbol{e}}_1$. The tensor $\mathbb{B}$ vanishes to order ε^2, and the combinations $N^{(vv)}_{n(qp)}$ and $N^{(\omega\omega)}_{n(qp)}$ vanish to order ε, although allowed to be non-zero by the symmetry analysis.

Appendix C: Stability of a settling ellipsoid

We consider the sedimentation of an ellipsoidal particle in a quiescent fluid. Such particles have D_{2h} symmetry. The force and torque are given by

$$\boldsymbol{F}=-\mathbb{A}\cdot\boldsymbol{v}+\mathrm{Re_p}\boldsymbol{F}^{(1)}-G\hat{\mathbf{e}}_3\,, \tag{C1a}$$

$$\boldsymbol{T}=-\mathbb{C}\cdot\boldsymbol{\omega}+\mathrm{Re_p}\boldsymbol{T}^{(1)}\,. \tag{C1b}$$

Here $\boldsymbol{F}^{(1)}=\boldsymbol{F}^{(1)}_{\rm reg}+\boldsymbol{F}^{(1)}_{\rm sing}$, where $\boldsymbol{F}^{(1)}_{\rm reg}$ takes the form in Eq. (14) with $M^{(vv)}=M^{(\omega\omega)}=0$ and $M^{(\omega v)}$ being of the same form as $N^{(vv)}$ due to the symmetry constraints posed by Eqs. (18), and $\boldsymbol{F}^{(1)}_{\rm sing}$ is given in Eq. (17). Moreover, $\boldsymbol{T}^{(1)}=\boldsymbol{T}^{(1)}_{\rm reg}$ is given in Eq. (20) [$\boldsymbol{T}^{(1)}_{\rm sing}=0$ since $\mathbb{B}=0$ for D_{2h} symmetry]. Finally, $-G\hat{\boldsymbol{e}}_3$ is the buoyancy force, with $G=(\rho_{\rm p}-\rho_{\rm f})V_{\rm p}g/(\mu v_0 a)$, where $V_{\rm p}$ is the particle volume, and $\rho_{\rm p}$ and $\rho_{\rm f}$ are the densities of the particle and fluid, respectively. We express the dynamics in the coordinate system $\boldsymbol{p},\boldsymbol{q},\boldsymbol{n}$ that rotates with the particle. In this system, $\mathbb{A}$ and $\mathbb{C}$ are diagonal for D_{2h}. Neglecting the fluid-inertia contribution to the hydrodynamic force, we obtain

$$\dot{v}_p=-A_{pp}v_p+F^{(1)}_p+G\cos\psi\sin\theta+\omega_n v_q-\omega_q v_n \tag{C2a}$$

$$\dot{v}_q=-A_{qq}v_q+F^{(1)}_q-G\sin\psi\sin\theta+\omega_p v_n-\omega_n v_p \tag{C2b}$$

$$\dot{v}_n=-A_{nn}v_n+F^{(1)}_n-G\cos\theta+\omega_q v_p-\omega_p v_q \tag{C2c}$$

$$\dot{\theta}=\omega_q\cos\psi+\omega_p\sin\psi\,, \quad \dot{\psi}=\omega_n+\cot\theta[\omega_p\cos\psi-\omega_q\sin\psi]\,, \tag{C2d}$$

$$\dot{\omega}_p=\frac{1}{I_{pp}}[-C_{pp}\omega_p+\mathrm{Re_p}T^{(1)}_p+\omega_n\omega_q(I_{qq}-I_{nn})] \tag{C2e}$$

$$\dot{\omega}_q=\frac{1}{I_{qq}}[-C_{qq}\omega_q+\mathrm{Re_p}T^{(1)}_q+\omega_p\omega_n(I_{nn}-I_{pp})] \tag{C2f}$$

$$\dot{\omega}_n=\frac{1}{I_{nn}}[-C_{nn}\omega_n+\mathrm{Re_p}T^{(1)}_n+\omega_q\omega_p(I_{pp}-I_{qq})]\,. \tag{C2g}$$

Here, $I_{pp},\ldots$ are the elements of the inertia tensor of the ellipsoidal particle. The $\omega_i v_j$ and $\omega_i\omega_j$ terms result from the time derivative of the particle orientation. We consider the dynamics in the subsystem $\boldsymbol{V}=[v_p,v_q,v_n,\theta,\psi,\omega_p,\omega_q,\omega_n]^{\mathsf{T}}$, not including $\boldsymbol{x}$ and ϕ, since these coordinates do not affect $\boldsymbol{V}$.

We search for a rotation-free steady state, $\boldsymbol{\omega}=0$. By solving $\dot{\boldsymbol{V}}=0$ under this condition, the system (C2) has six fixed points corresponding to the particle settling with either $\boldsymbol{p}$, $\boldsymbol{q}$, $\boldsymbol{n}$ aligned with or against gravity. The settling speed is obtained as a solution to a second-order polynomial. For small Reynolds numbers, it takes the form $v^*_g=G/A^{(g)}$, where $A^{(g)}$ is the component of the resistance tensor in the direction that aligns/anti-aligns with gravity.

The 8×8 stability matrix $\mathbb{J}$ has elements $J_{ij} = \partial_{V_j} \dot{V}_i$. Evaluating $\mathbb{J}$ at either of the fixed points and suitably permuting the rows and columns, we find that it is block-diagonal with two 1-blocks and two 3-blocks. The eigenvalues of the 1-blocks are the negative resistance elements $\lambda_1 = -A^{(g)}$ and $\lambda_2 = -C^{(g)}/I^{(g)}$. The eigenvalues of the 3-blocks each satisfy a third-order polynomial being equal to zero, giving the stability exponents λ_{3-5} and λ_{6-8}, respectively. For particles settling with $\boldsymbol{n}$ pointing downwards, these become (neglecting contributions of order $\mathrm{Re_p^2}$)

$$
\begin{aligned}
&0 = \lambda^3 + P_2\lambda^2 + P_1\lambda + P_0 \text{ and } 0 = \lambda^3 + Q_2\lambda^2 + Q_1\lambda + Q_0 \text{ with } P_0 = -\frac{2N^{(vv)}_{p(qn)}}{I_{pp}}\frac{G^2\mathrm{Re_p}}{A_{nn}}\,,\; Q_0 = \frac{2N^{(vv)}_{q(np)}}{I_{qq}}\frac{G^2\mathrm{Re_p}}{A_{nn}}\,,\\
&P_1 = \frac{A_{qq}C_{pp}}{I_{pp}}(1 - \frac{G\mathrm{Re_p}}{32\pi}\frac{A_{nn}-3A_{qq}}{A_{nn}}) - 2N^{(vv)}_{p(qn)}\frac{G^2\mathrm{Re_p}}{A^2_{nn}I_{pp}}\,,\; Q_1 = \frac{A_{pp}C_{qq}}{I_{qq}}(1 - \frac{G\mathrm{Re_p}}{32\pi}\frac{A_{nn}-3A_{pp}}{A_{nn}}) + 2N^{(vv)}_{q(np)}\frac{G^2\mathrm{Re_p}}{A^2_{nn}I_{qq}}\,,\\
&P_2 = A_{qq} + \frac{C_{pp}}{I_{pp}} - \frac{G\mathrm{Re_p}}{32\pi}\frac{A_{qq}}{A_{nn}}(A_{nn}-3A_{qq})\,,\; Q_2 = A_{pp} + \frac{C_{qq}}{I_{qq}} - \frac{G\mathrm{Re_p}}{32\pi}\frac{A_{pp}}{A_{nn}}(A_{nn}-3A_{pp})\,.
\end{aligned}
\tag{C3}
$$

A necessary condition for these polynomials to only have negative solutions is that all polynomial coefficients are positive, $P_i > 0$ and $Q_i > 0$, which requires

$$
N^{(vv)}_{p(qn)} < 0 \text{ and } N^{(vv)}_{q(np)} > 0\,. \tag{C4}
$$

A sufficient condition (Routh-Hurwitz criterion) is that additionally the product of the coefficients of λ and λ^2 is larger than the constant coefficient:

$$
P_1P_2 > P_0 \text{ and } Q_1Q_2 > Q_0\,. \tag{C5}
$$

Alignment with $\boldsymbol{n}$ pointing against gravity (instead of along) gives the same stability exponents. The stability exponents for the remaining four orientations are obtained by permutations of $\boldsymbol{p}$, $\boldsymbol{q}$, and $\boldsymbol{n}$. The conditions corresponding to Eq. (C4) when settling along or against $\boldsymbol{p}$ and $\boldsymbol{q}$ are

$$
N^{(vv)}_{n(pq)} < 0 \text{ and } N^{(vv)}_{p(qn)} > 0 \text{ for } \boldsymbol{q} \parallel \boldsymbol{e}_3 \tag{C6a}
$$

$$
N^{(vv)}_{q(np)} < 0 \text{ and } N^{(vv)}_{n(pq)} > 0 \text{ for } \boldsymbol{p} \parallel \boldsymbol{e}_3 \tag{C6b}
$$

The three conditions (C4) and (C6) are mutually exclusive. This means that at most one orientation can be stable. In the overdamped limit (large components of the resistance tensor), Eqs. (C5) are satisfied and the ellipsoid obtain a stable orientation provided that at least two of the components $N^{(vv)}_{n(pq)}$, $N^{(vv)}_{q(np)}$, and $N^{(vv)}_{n(pq)}$ have opposite signs. This orientation may become unstable for less inertial particles, for which Eqs. (C5) are no longer satisfied.

For nearly spherical ellipsoids, the shape parameters are given in Eq. (B 2). Substituting the results into Eqs. (C4), (C5), and (C6) shows that, as long as $|\epsilon|$ is not too large, the particle aligns $\boldsymbol{n}$ with gravity if $\varepsilon < 0$ and $\alpha > 0$ and $\alpha > 0$, aligns $\boldsymbol{q}$ if $\varepsilon > 0$ and $\alpha < 1$, and aligns $\boldsymbol{p}$ if $\varepsilon > 0$ and $\alpha > 1$ or if $\varepsilon < 0$ and $\alpha < 0$. All these cases correspond to the particle aligning the broadest cross section perpendicular to gravity.

Appendix D: Asymptotic matching for large Strouhal numbers

Here we show how to obtain Eqs. (31). When the Strouhal number is large, in the limit $1 \gg \mathrm{Re_p Sl} \gg \mathrm{Re_p}$, the equations for the outer flow may be simplified by neglecting the convective terms. Force and torque on the particle can still be obtained using matched-asymptotic expansions, but extended to the second order, following Candelier *et al.* [63], but setting the undisturbed flow to 0. In short, the idea is to seek the disturbance flow in the form

$$
\boldsymbol{w}_{\mathrm{in}} = \boldsymbol{w}^{(0)}_{\mathrm{in}} + \sqrt{\mathrm{Re_p Sl}}\,\boldsymbol{w}^{(1)}_{\mathrm{in}} + \mathrm{Re_p Sl}\,\boldsymbol{w}^{(2)}_{\mathrm{in}} + \dots \quad \text{and} \quad p_{\mathrm{in}} = p^{(0)}_{\mathrm{in}} + \sqrt{\mathrm{Re_p Sl}}\,p^{(1)}_{\mathrm{in}} + \mathrm{Re_p Sl}\,p^{(1)}_{\mathrm{in}} + \dots\,. \tag{D1}
$$

To second order, the outer flow equations require two source terms, $f^{(0)}$ and $f^{(1)}$,

$$
\mathrm{Re}_p\,\mathrm{Sl}\,\frac{\partial \boldsymbol{w}}{\partial t} = -\boldsymbol{\nabla} p + \triangle \boldsymbol{w} + \left(\boldsymbol{f}^{(0)} + \sqrt{\mathrm{Re_p Sl}}\,\boldsymbol{f}^{(1)}\right)\delta(\boldsymbol{r})\,. \tag{D2}
$$

The solution of this outer equation takes the form

$$
\begin{aligned}
\boldsymbol{w}_{\mathrm{out}} =& \frac{1}{8\pi}\left(\frac{\mathbb{1}}{r} + \frac{\boldsymbol{r}\otimes\boldsymbol{r}}{r^3}\right)\cdot\left(\boldsymbol{f}^{(0)} + \sqrt{\mathrm{Re_p Sl}}\,\boldsymbol{f}^{(1)}\right) + \sqrt{\mathrm{Re}_p\mathrm{Sl}}\,\boldsymbol{\mathcal{U}}_1\\
&+ \mathrm{Re}_p\mathrm{Sl}\left(\frac{3r}{32\pi}\left(\mathbb{I} - \frac{1}{3}\frac{\boldsymbol{r}\otimes\boldsymbol{r}}{r^2}\right)\frac{\mathrm{d}\boldsymbol{f}^{(0)}}{\mathrm{d}t} + \boldsymbol{\mathcal{U}}_2\right)
\end{aligned}
\tag{D3}
$$

where

$$\boldsymbol{\mathcal{U}}_1 = -\int_0^t \frac{\mathrm{d}\tau}{6\pi}\frac{1}{\sqrt{\pi(t-\tau)}}\frac{\mathrm{d}\boldsymbol{f}^{(0)}}{\mathrm{d}\tau} \quad \text{and} \quad \boldsymbol{\mathcal{U}}_2 = -\int_0^t \frac{\mathrm{d}\tau}{6\pi}\frac{1}{\sqrt{\pi(t-\tau)}}\frac{\mathrm{d}\boldsymbol{f}^{(1)}}{\mathrm{d}\tau}\,. \tag{D4}$$

The matching procedure leads us to $\boldsymbol{f}^{(1)} = -\mathbb{A}\cdot\boldsymbol{\mathcal{U}}_1$. The corresponding singular contributions to force and torque read:

$$\boldsymbol{F}^{(1)}_{\text{sing}} = \mathbb{A}\cdot\boldsymbol{\mathcal{U}}_1, \quad \boldsymbol{F}^{(2)}_{\text{sing}} = \mathbb{A}\cdot\boldsymbol{\mathcal{U}}_2,$$

$$\boldsymbol{T}^{(1)}_{\text{sing}} = \mathbb{B}\cdot\boldsymbol{\mathcal{U}}_1, \quad \boldsymbol{T}^{(2)}_{\text{sing}} = \mathbb{B}\cdot\boldsymbol{\mathcal{U}}_2\,.$$

In the limit $\mathrm{Sl} \gg 1$, the two kernels $\mathbb{K}^{(1)}$ and $\mathbb{K}^{(2)}$, defined in Eqs. (A1)–(A2), simplify as

$$\mathbb{K}^{(1)} \longrightarrow \frac{1}{6\pi\sqrt{t-\tau}}\,, \qquad \mathbb{K}^{(2)} \longrightarrow \mathbb{0}\,, \tag{D5}$$

the same as the kernel $\boldsymbol{U}_1$ in Eq. (D4). The derivation underlying Eqs. (A1)–(A2) assumed $\mathrm{Sl} \ll 1$. Eq. (D5) shows that the result remains uniformly valid at order $\sqrt{\mathrm{Re_p\,Sl}}$. To order $\mathrm{Re_p\,Sl}$ there are additional contributions to the memory kernel in the form of a double convolution. For an isotropic particle where $\mathbb{A} \propto \mathbb{I}$, the double convolution simplifies to an instantaneous contribution connected to the added mass [63].

Now consider the regular contribution. The regular expansion for the disturbance velocity in the inner region is linearly related to the particle velocity $\boldsymbol{v}$ and its angular velocity $\boldsymbol{\omega}$

$$\boldsymbol{w}^{(0)}_{\text{in}} = \mathbb{W}_v(\boldsymbol{X})\cdot\boldsymbol{v} + \mathbb{W}_\omega(\boldsymbol{X})\cdot\boldsymbol{\omega}\,, \tag{D6}$$

where X_i are coordinates in the particle-fixed coordinate system. Eq. (2), however, is written in a coordinate system that translates with particle (but does not rotate with it). Evaluating the time derivative of $\boldsymbol{w}^{(0)}_{\text{in}}$ in the translating coordinate system yields an expression that depends linearly on $\dot{\boldsymbol{v}}$ and $\dot{\boldsymbol{\omega}}$, and there are also second-order terms proportional to $\boldsymbol{\omega}\otimes\boldsymbol{v}$ and $\boldsymbol{\omega}\otimes\boldsymbol{\omega}$. Hydrodynamic force and torque must have the same tensorial structure. There are quadratic terms just like Eq. (14). But there are also unsteady contributions to force and torque of the form

$$\boldsymbol{F}^{(2)}_{\text{u}} = \mathrm{Re_p Sl}\,(\mathbb{P}\dot{\boldsymbol{v}} + \mathbb{Q}\dot{\boldsymbol{\omega}})\,, \tag{D7a}$$

$$\boldsymbol{T}^{(2)}_{\text{u}} = \mathrm{Re}_p\mathrm{Sl}\,(\mathbb{Q}^{\mathsf{T}}\dot{\boldsymbol{v}} + \mathbb{R}\dot{\boldsymbol{\omega}})\,, \tag{D7b}$$

distinct from the terms discussed in the main text. Here $\mathbb{P}$, $\mathbb{Q}$, $\mathbb{R}$ are second-order tensors, constrained by symmetry in the same way as the second-order Stokes resistance tensors. The fact that $\mathbb{Q}^{\mathsf{T}}$ appears in the expression for the torque follows from the reciprocal theorem. The terms (D7) that look like added-mass contributions. They were first obtained by Gavze [71], who derived a general solution of the unsteady Stokes equation for a particle of arbitrary shape. More recently, Collis *et al.* [37] considered the same limit as Gavze [71]. They solved the unsteady Stokes equation for several nearly spherical particles to obtain hydrodynamic force and torque in the unsteady limit, at large Strouhal numbers. No history terms appear in their expressions, because they work in the frequency domain. Integration over frequency must give these terms, in the same way as for a sphere oscillating in a fluid at rest [62].

ISBN 978-91-988537-1-1 (PRINT)